STUDY OF SOLAR MICROWAVE RADIATION USING MULTIFREQUENCY DATA

Thesis by

Jeongwoo Lee

In Partial Fulfillment of the Requirements

for the Degree of

Doctor of Philosophy

California Institute of Technology

Pasadena, California

1994

(Submitted October 21, 1993)

Acknowledgements

I joined the Caltech Solar Group four years ago without a good knowledge of the sun. Prof. Harold Zirin kindly guided me to the real sun. Although his criticism was always cold to the ideas that I brought to him, it helped me to strengthen my argument in the end. On the other hand, his encouragement was warm as the sun to bring me out of every dilemma I had. Without these two, the works presented here would have never been finished. So, I dedicate this thesis to him.

The work presented in this thesis was motivated and made possible by the solar microwave data obtained from the world-premier, frequency-agile telescope at the Owens Valley Radio Observatory. Dr. Gordon Hurford designed this instrument and initiated the observations. Dr. Dale Gary guided me to the physics of solar microwave radiation and supported me for most of the period of this study. My special appreciation is therefore due to these two persons. I wish this thesis could partly reward their efforts to keep the instrument operating to produce those valuable data.

I was happy sitting in one of Prof. Roger Blandford's classes, Ph136, where I got most of my current knowledge used in my research. Prof. Shrinivas Kulkarni taught me the fundamentals of radio instrumentation, without which I would still be in the dark about the radio business.

I appreciate Sara Martin, Francis Tang, and Haimin Wang for sharing with me their invaluable wisdom and experience of the sun, and Web Ewell and Martin Woodard for helping me with better English. I am grateful to Nora Knicker for her help with paper submissions. I also thank Stephen Benka for sending me a copy of his thesis which helped me to shorten the time in learning basic formulae for microwave and X-ray radiation as used in Chapter 5.

Finally, I would like to thank my parents for their encouragement to pursue a doctoral degree at Caltech and my wife for her support and love throughout the life at Pasadena.

To Professor Harold Zirin

Abstract

I have carried out analysis of multifrequency data of solar microwave radiation gathered by the frequency-agile telescope at Owens Valley Radio Observatory to address several long-standing problems in the study of active region structure and solar flare particles.

In the study of active region structure, I use the microwave data and the magnetograms of NOAA 4741 obtained during 1986 August 2 - 9 to discover: (i) change of dominant radiation mechanism with the coronal height, (ii) angle-dependent properties of the gyroresonance opacity, (iii) distribution of the coronal magnetic fields and its implication for the force balance in the upper atmosphere of the active region. The merit of this study lies in the fact that most results are empirical and thus provide an observational basis to test theoretical sunspot models and the gyromagnetic radiation theory.

In the flare study, I deal with impulsive bursts and extended bursts, aiming at two issues: (i) the physical link between microwaves and hard X-rays in impulsive bursts and (ii) influence of ambient plasma on the evolution of extended microwave activity. The first issue has been addressed by a kinetic approach made to deduce the distribution of microwave-emitting electrons and hard X-ray electrons in momentum space, referring to the 1989 March 18 flare in NOAA 5395. For the second issue, I analyse data of extended microwave bursts on 1990 May 24 (NOAA 6063), 1991 March 7 and 8 (NOAA 6538), and 1991 March 22 (NOAA 6555) in terms of a nonuniform coronal trap model to deduce source conditions responsible for the observed anomalies of extended bursts. These data sets and results of analysis underline the influence of the source condition on the spectral and temporal evolution of microwave radiation during solar flares.

Table of contents

Chapter 1

Introduction to solar microwave radiation

1. Preliminaries and Statement of Purposes

Solar microwave radiation has historically been divided into two components: the slow microwave component and the microwave burst. The slow component refers to quiescent microwave radiation from a static active region and is thus believed to be of thermal origin. The microwave burst refers to explosive microwave radiation due to energetic nonthermal particles produced during solar flares that accompany other high energy emissions such as X-rays. In the following two sections, I describe the proposed radiation mechanisms for both components and discuss the scientific goals of their study and observational requisite for achieving the goals.

1.1. THE SLOW COMPONENTS

The slow component is believed to be due to either the gyroresonance emission or free-free emission from thermal nonrelativistic electrons.

The gyroresonance radiation is due to centripetal acceleration of nonrelativistic electrons gyrating in a magnetic field and is concentrated over a narrow frequency range centered at first few harmonics of the gyrofrequency, $\nu_B = eB/m_e c$ (Ginzberg and Zheleznyakov, 1961). Here, e and m_e are the electric charge and the mass of an electron; c is the speed of light; B is magnetic field strength. This radiation is efficient at the lower corona of solar active regions where the field strength is high above a few hundred gauss and the electron thermal velocity is about $0.01c$-$0.02c$. The gyroresonance opacity is very sensitive to the strength of ambient magnetic fields, which makes this radiation perhaps the unique diagnostic for the coronal magnetic field structure above solar active regions.

Free-free emission at radio frequencies is due to distant encounters of electrons with ions in the Coulomb field, which cause an acceleration by small-angle deflection. The free-free emission provides information of the column emission measure, $\int n_e^2 dl$. Here, n_e is the electron number density and l is the thickness of the medium along

the line-of-sight. The free-free emission may dominate the gyroresonance emission in a region with relatively weaker fields and higher electron density.

Study of microwave slow components starts by determining which is the more dominant radiation mechanism between gyroresonance and free-free radiation. Once the emission mechanism had been determined, two further scientific goals may be sought. In one, the diagnostic capabilities of these radiations are exploited to determine physical parameters of the coronal active region, notably the magnetic field strength, B, from the gyroresonance spectra and the column emission measure, $\int n_e^2 dl$, from the free-free spectra. In the other, observations are made to investigate the theoretically proposed properties of radiation mechanisms, mainly referring to some characteristics relatively insensitive to particular values of source parameters such as: (i) the frequency-dependence, (ii) the angle-dependence, and (iii) degree of circular polarization. This mainly refers to the case of gyroresonance radiation which suggests many interesting problems associated with magneto-ionic theory.

Previous works on slow components have been directed toward these scientific goals in several different ways depending on the type of observation. In observations with large arrays such as WSRT and VLA, detailed spatial morphology of radio images obtained at one or a few frequencies is studied. In this case, judgement of a dominant radiation mechanism has been based on the model-calculation of theoretical opacities of gyroresonance and free-free opacity. For the source parameters needed for model-calculation, use is made of density and temperature obtained from simultaneous observations of EUV or soft X-rays (e.g., Schmahl *et al.*, 1982; Shibasaki *et al.*, 1983; Chiuderi-Drago, Alissandrakis, and Hagyard, 1987) or a model atmosphere (e.g., Allisandrakis, Kundu, and Lantos, 1980). As for the magnetic fields, the field extrapolation of photospheric magnetic fields measured from magnetograms is often used.

Observations with frequency-agile telescopes such as RATAN-600 and the Solar Array at the Owens Valley Radio Observatory (OVRO) permit a more empirical

approach to the radiation mechanism and magnetic field strengths. A brightness temperature spectrum that falls off proportional to ν^{-2} is due to free-free emission, in which case the spectral information can be used to determine the column emission measure (Gary and Hurford, 1987, 1994). If the spectrum falls off steeper than ν^{-5} with a large degree of circular polarization, it is due to gyroresonance radiation and the limiting frequency is, in this case, related to the magnetic field strength of the source region. Such spectral information together with one-dimensional spatial information has been used to constrain parameters of a dipole model for a sunspot (Akhmedov *et al.*, 1982; Krüger *et al.*, 1986; Hurford and Gary, 1986; Borovik *et al.*, 1989).

In cases where observations of a steady active region are continued for many days, the daily variation of microwave spectra can be compared with predictions of the gyromagnetic radiation theory (e.g., Zheleznyakov, 1970; Zlotnik, 1968ab; Lantos, 1968) to understand angle-dependent properties of gyroresonance opacity (e.g., Kakinuma and Swarup, 1962; Papagiannis and Kogut, 1975). Especially, a polarization reversal, expected to occur during center-to-limb passage of the source region, has attracted some efforts in relation to the theory of wave-propagation in the magneto-ionic modes (e.g., Kundu and Alissandrakis, 1984; White, Thejappa, and Kundu, 1992).

In this thesis, I pursue a complete, empirical approach to understand both the coronal magnetic structure of a sunspot and the properties of gyroresonance radiation, taking advantage of the high spectral resolution provided by the OVRO Solar Array, using a data set chosen carefully to achieve these goals. I use the technique proposed by Hurford, Gary, and Garrett (1985) to determine field strength as a function of distance across a sunspot. It can be foreseen that the field measurement will be easier if the source has a simple morphology and is located near the disk center. The latter is to avoid a projection effect in interpreting magnetogram data. The study of the angle-dependence of gyromagnetic opacity requires little or no change of the source during its center-to-limb passage. The chance to meet all of

these observational requisites will be low in general, but could be high around the time of solar minimum, where active regions tend to have simpler morphology and are quiescent over longer periods. In addition, active regions get closer to the equator around solar minimum so that the projection effect is lowered when they pass the disk center. Under these considerations, I take the microwave data of NOAA 4741 obtained at OVRO when it passed from the center to limb during 1986 August 2-9 as the best data set for the study of the microwave slow component.

1.2. MICROWAVE BURSTS

The microwave bursts appear in various types implying that many different physical mechanisms can be involved from flare to flare. The initial efforts to understand such a variety have been made in terms of phenomenological classifications such as those according to time profiles of monochromatic flux (Kundu, 1965), association with Hα or X-rays (De Jager, 1967), or spectral shape (e.g., Guidice and Castelli, 1975; Böhme *et al.*, 1978). A modern classification tends to be made according to the presumed radiation mechanisms such as gyrosynchrotron emission, free-free emission, and coherent emissions (Dulk, 1985; Dulk, McLean, and Nelson, 1985).

The gyrosynchrotron emission is due to centripetal acceleration of mildly relativistic electrons gyrating in a magnetic field with speed 0.2c-0.9c (Takakura, 1960). As compared to the gyroresonance emission mentioned above, the spectral peaks of gyrosynchrotron emission are more broad and are extended to higher harmonics as more energetic electrons are involved. The free-free emission is relatively unimportant in the flare study because it diminishes as the electron temperature increases during flares. The only place they play a role is the weak events known as the 'gradual rise-and-fall' microwave bursts (e.g., Hudson and Ohki, 1972; Shimabukuro, 1972) where total flux is usually below 40 sfu above 1 GHz (Švestka, 1976, p140). Here, the 'sfu' represents the solar flux unit and 1 sfu corresponds to 10^{-22} W m^{-2} Hz^{-1}. Coherent emissions in solar flares have two types: electron-cyclotron masers and plasma radiation (see Dulk, 1985 for review). They pose interesting problems

regarding plasma instability under solar flare conditions. It is, however, unlikely that they are a significant contributor to the total microwave outputs during flares because the resulting fluxes are confined to an extremely narrow frequency range and a short time interval.

Therefore, only the gyrosynchrotron radiation is left as the most important radiation mechanism responsible for the majority of solar microwave bursts (Takakura, 1967; Ramaty, 1969). This is perhaps due to the fact that the gyrosynchrotron radiation is a relatively efficient emission process in an environment with moderately strong magnetic fields (10^2 - 10^3 G), as is the case of solar active regions where flares occur. In particular, microwave spectra which appear in a broad-band with fluxes above 10^2 sfu are most likely due to gyrosynchrotron radiation. Similar to the gyroresonance spectrum, the gyrosynchrotron spectrum does carry information of the ambient magnetic fields. However, more interesting in relation to the flare study would be the physics underlying the whole time-variability of the microwave fluxes, which is yet unclear in spite of numerous spirited works. Below, I discuss this issue mainly referring to two contrasting cases: impulsive bursts and large extended bursts both of which are presumed to be due to the gyrosynchrotron radiation for the reason mentioned above.

Impulsive microwave bursts with duration from a few seconds to minutes are commonly seen in typical solar flares. The nature of impulsive microwave bursts has usually been discussed in comparison with the accompanying hard X-rays. A very good correlation between impulsive microwave bursts and hard X-ray bursts has long been known not only in fluxes but in time profiles (e.g., Dennis, 1988). It is thus postulated that microwaves are due to the same or a closely-related population of hard X-ray electrons. In a most widely accepted model for hard X-rays, however, the high-energy electrons are accelerated in the corona, stream downward along magnetic fields, and emit hard X-rays near the footpoints through thick-target bremsstrahlung (Brown, 1971, 1972; Petrosian, 1973; Dennis, 1988). On the other

hand, microwaves may be emitted by the high-energy electrons traversing the coronal portion of the loop. Therefore, the sites of microwave emission and hard X-ray emission can differ although both radiations are due to the same or closely-related population of electrons (Petrosian, 1989; Lu and Petrosian, 1990). It should also be noted that microwaves are emitted by high energy electrons ($\geq$ 200 keV) and hard X-rays by low energy electrons (Takakura, 1973). This fact may be a clue to the observed time-delay of impulsive microwave peak relative to that of accompanying hard X-rays (Crannell *et al.*, 1978; Kaufmann *et al.*, 1983; Cornell *et al.*, 1984; Lu and Petrosian, 1990) if acceleration of electrons to higher energy needs a finite time to operate (Dulk, Kiplinger, and Winglee, 1992). Accepting such an acceleration scenario, the next concern would be the energy release of flare electrons which can be described by the evolution of electron distribution in momentum space. A point worthy of investigation with spectral information is whether microwave electrons and hard X-ray electrons evolve in different ways due to different sites in a magnetic loop and due to different energy dependence of various cooling mechanisms.

The 'extended microwave bursts' refer to long-period events with high flux (e.g., $\geq 10^2$ sfu) such as those reported in Kosugi, Dennis, and Kai's (1988) paper. It should be distinguished from the above-mentioned 'gradual rise-and-fall bursts' which also have long-period but refer to weaker events. The extended microwave bursts are less common in general but common in very large flares. In these events, the microwave activity is not only longer than that of impulsive microwave events, but also exceed that of accompanying hard X-rays, which leads to microwave richness in the decay phase. A viable model for microwave excess in the decay phase has been the coronal trap model in which microwave emitting electrons survive longer due to being trapped in the coronal part of a flaring loop (e.g., Vilmer, Kane, and Trottet, 1982; Kai, Kosugi, and Nitta, 1985; Kosugi, Dennis, and Kai, 1988; Bruggmann *et al.*, 1993). As this notion will also apply to the impulsive burst (cf., Lu and Petrosian, 1990), a distinction between the extended event and the impulsive event seems to lie in how efficient the coronal trap is in keeping the high energy

electrons. Also related to this issue are the existence of continuous injection, the role of magnetic field structure in modulating the life time of electrons, and so on.

Missing in the previous studies of both cases is the detailed spectral morphology of microwaves with which the comparative study of microwave emitting electrons and hard X-ray electrons could be more informative. What we have learned from high-spectral resolution data obtained at OVRO is that microwave fluxes in impulsive events evolve keeping more or less the same spectral shape (Stähli, Gary, and Hurford, 1989; 1990). In contrast, hard X-ray bursts are known to show a characteristic variation of their spectral shape during flares (e.g., Lin and Schwartz, 1987; Dulk, Kiplinger, and Winglee, 1992). Such a distinction between microwave spectral activity and that of hard X-rays could be an important clue to elucidate the nature of impulsive microwave bursts. Meanwhile, a few good samples of the extended bursts have been gathered using the OVRO Solar Array, in observations of large flares that occurred during the last solar maximum. These data show a characteristic variation of spectral shape, different from the case of typical impulsive events. It is likely that such a variation reflects a corresponding change in the macroscopic source parameters, which is perhaps unique to big flares, but absent in normal impulsive events.

These spectroscopic results of the OVRO Solar Array encourage a challenge to the two main issues: (i) the physical link between the microwaves and hard X-rays in an impulsive event and (ii) the origin of extended microwave bursts. A notion that I would like to develop through the study of these data is the influence of the ambient plasma and magnetic fields upon radiating particles, which has different observational consequences for microwaves and hard X-rays as seen respectively in impulsive events and extended events. There are basically two ways that ambient plasma can influence the microwave radiation; the direct way is by absorption of the radiation and the indirect way is by modulating the evolution of radiating particles. In this thesis, the primary effort of analyzing data will be focused on the separation

of these two factors, without which interpretation of microwave burst spectra might go astray.

2. Overview of Thesis

This thesis is in two parts: Part I presents a study of slow microwave components and Part II, the study of microwave bursts.

2.1. PART I

Part I consists of Chapter 2, Chapter 3, and Chapter 4. The results presented in these chapters are all based on microwave observations of a static sunspot in an active region, NOAA 4741, which passed the solar disk from the center to limb on 1986 August 2-9. Owing to the lowest level of solar activity in the last solar cycle and the relatively simple structure of the active region, an excellent opportunity is given for exploring the static structure of the magnetic fields and the angle-dependent properties of gyroresonance opacity. I present the results of the magnetic field distribution in Chapter 2, the results for angle-dependent properties in Chapter 3, and implication for magnetostatic equilibrium in Chapter 4, respectively.

In Chapter 2 I analyze the multifrequency images of the sunspot when it was located near the disk center in which case we can avoid the projection effect on the magnetic field measurement. The radio sizes of the sunspot measured at 24 frequencies are converted to the horizontal distribution of magnetic fields at the coronal base of the sunspot using the property that microwave brightness is limited above a frequency given by a first few harmonics of the gyrofrequency. The value of maximum effective harmonic has been determined empirically using the principle of magnetic flux conservation and magnetogram data. In this way, the horizontal distribution of magnetic fields at the coronal base of this spot is found in a gaussian form with $1/e$-folding radius of 11 arcsec and central magnetic field strength of 1420 G.

Chapter 3 presents the center-to-limb variation of the microwave spectra of this active region. Main results are as follows: First, sunspot microwave emission appears in a double-peak structure near the disk center but in a single-peak structure near the limb. Second, the brightness temperature at high, optically-thin frequencies shows a limb-increase. These two observational characteristics have been interpreted as due to the angle-dependence of the gyroresonance opacity. Third, the center-to-limb variation of circular polarization seems to be characterized by a change of effective harmonic, which is thus discontinuous. Fourth, a change of spectrum from gyroresonance to free-free emission is found when the spot passed over the solar limb, which confirms the location of the gyroresonance source low in the corona of the active region.

In Chapter 4 I combine the horizontal and vertical field distributions obtained respectively in Chapter 2 and Chapter 3 to present the three-dimensional structure of the magnetic fields as a whole. Since these results are empirical, they can be compared with a few theoretical models to yield a physical implication of the deduced magnetic structure of this sunspot. A satisfactory fit is obtained for a model which is based on force balance between the magnetic curvature force and the horizontal pressure gradient. It is therefore concluded that the sunspot fields at the coronal base tend to be kept confined by the pressure gradient across the sunspot.

The results presented in Part I consist of a complete set of works in which the diagnostic capability of gyromagnetic radiation is fully exploited on an empirical basis to understand the magnetic structure of a sunspot as well as the principal characteristics of the gyromagnetic radiation.

2.2. PART II

Part II presents results of analysis of several microwave burst spectra which are assumed to be due to nonthermal gyrosynchrotron radiation. Two contrasting cases are studied: a typical impulsive microwave burst in Chapter 5 and a set of extended microwave bursts in Chapter 6.

In Chapter 5 I analyze the time variation of microwave spectra and hard X-ray spectra of the 1989 March 18 flare to explore the evolution of radiating particles primarily in the decay phase. The observational motivation is that microwaves decouple from hard X-rays in the decay phase, away from the good correlation seen at the initial rise. The hypothesis is investigated whether the observed decoupling is due to the different cooling efficiency of high energy electrons in each source region. For this purpose, a Fokker-Planck equation which describes the stochastic acceleration of electrons by the Whistler waves, energy loss by Coulomb interaction, and particle escape is set up and solved numerically. The Fokker-Planck solutions are used to calculate microwave and hard X-ray spectra for agreement with observations. Results are as follows: In a stronger field region, the energy loss by electron escape due to scattering by the waves is greatly enhanced resulting in steep particle distributions that reproduce the observed hard X-ray spectra. In a region with weaker fields and lower density, the probability of electron escape is reduced allowing high energy electrons to survive longer so that microwaves can be emitted there in excess of hard X-rays during the decay phase of the flare. These results based on spectral fitting are discussed in comparison with previous studies of microwaves and hard X-rays based on either temporal or spatial information.

In Chapter 6 I analyze a set of large, extended microwave bursts as obtained from four X-Class flares that occurred on 1990 May 24 and 1991 March 7, 8, and 22. These data are characteristic in that the flux spectra are flat in shape and unusually high in amount of flux at the maximum phase, and that time profiles are impulsive at high frequencies but more extended at lower frequencies. These rather peculiar characteristics have been interpreted in terms of a nonuniform magnetic loop and nonthermal gyrosynchrotron radiation mechanism. Main results are summarized as follows: First, a flat microwave spectrum reaching up to 10^2 - 10^4 sfu may occur in a case where a magnetic loop is expanded to a large size containing abundant nonthermal electrons (10^{36} - 10^{38} above 10 keV) with power law index $\delta \sim 3$ - 3.5. Second, the observed spectral activity could adequately be accounted for by the shrinking of the region of nonthermal electrons to the loop top and by softening of

electron power-laws. Third, the extended microwave activity at lower frequencies is probably due to electrons trapped in the loop top where magnetic fields are low.

The results presented in Part II cover two distinct types of nonthermal gyrosynchrotron radiation and underline the influence of source conditions on the evolution of particles and microwave radiations during solar flares.

References

Akhmedov, Sh. B., Gelfreich, G. B., Bogod, V. N., and Korzhavin, A. N.: 1982, *Solar Phys.* **79**, 41.

Alissandrakis, C. E., Kundu, M. R., and Lantos, P.: 1980, *Astron. Astrophys.* **82**, 30.

Böhme, A., Fürstenberg, Hildebrandt, J., and Krüger A.: 1978, *Phys. Solariterr., Potsdam No.* **7**, 13.

Borovik, V. N., Gelfreikh, G. B., Bogod, V. M., Korzhavin, A. N., Krüger, A., Hildebrant, J., and Urpo., S.: 1989, *Solar Phys.* **124**, 157.

Brown, J. C.: 1971, *Solar Phys.* **18**, 489.

Brown, J. C.: 1972, *Solar Phys.* **25**, 158.

Bruggmann, G., Vilmer, N., Klein, K.-L., and Kane, S. R.: 1993, *Solar Phys.* in press.

Chiuderi-Drago, F., Alissandrakis, C., and Hagyard, M.: 1987, *Solar Phys.* **112**, 89.

Cornell, M. E., Hurford, G. J., Kiplinger, A. L., and Dennis, B. R.: 1984, *Astrophys. J.* **279**, 875.

Crannell, C. J., Frost, K. T., Mätzler, C., Ohki, K. and Saba, J. L.: 1978, *Astrophys. J.* **223**, 620.

De Jager, C.: 1967, *Solar Phys.* **2**, 327.

Dennis, B. R.: 1988, *Solar Phys.* **118**, 49.

Dulk, G. A.: 1985, *Ann. Rev. Astr. Ap.* **23**, 169.

Dulk, G. A., Kiplinger, A. L., and Winglee, R. M.: 1992, *Astrophys. J.* **389**, 756.

Dulk, G. A., McLean, D. J., and Nelson, G. J.: 1985, in D. J. Nelson and N. R. Labrum, (eds.), *Solar Radiophysics.*, Cambridge Univ Press, Chapter 4.

Gary, D. E. and Hurford, G. J.: 1994, *Astrophys. J.* in press.

Gary, D. E. and Hurford, G. J.: 1987, *Astrophys. J.* **317**, 522.

Ginzburg, V. L. and Zheleznyakov, V. V.: 1961, *Soviet Astron.* **5**, 1.

Guidice, D. A. and Castelli, J. P.: 1975, *Solar Phys.* **44**, 155.

Hudson, H. S. and Ohki, K.: 1972, *Solar Phys.* **23**, 155.

Hurford, G. J. and Gary, D. E.: 1986, *Coronal Processes and Plasmas*, Nasa Conference Proc. 2442, p. 319.

Hurford, G. J., Gary, D. E., and Garrett, H. B.: 1985, in R.M. Hjellming and D.M. Gibson, (eds.), *Radio Stars*, (Dordrecht:Reidel), p. 379.

Kai, K., Kosugi, T., and Nitta, N.: 1985, *Publ. Astron. Soc. Japan* **37**, 105.

Kakinuma, T. and Swarup , G.: 1962, *Astrophys. J.* **277**, 865.

Kaufmann, P., Strauss, F. M., Costa, J. E. R., Dennis, B. R., Kiplinger, A., Frost, K. J., and Orwig, L. E.: 1983, *Solar Phys.* **84**, 311.

Kosugi, T., Dennis, B. R., and Kai, K.: 1988, *Astrophys. J.* **324**, 1118.

Krüger, A., Hildebrandt, J., Bogod, V. M., Korzhavin, A. N., Akhmedov, Sh. B., and Gelfreikh, G. B.: 1986, *Solar Phys.* **105**, 111.

Kundu, M. R.: 1965, *Solar Radio Astronomy*, Interscience, New York.

Kundu, M. R. and Alissandrakis, C.E.: 1984, *Solar Phys.* **94**, 249.

Lantos, P.: 1968, *Ann Astrophys.* **31**, 105.

Lin, R. P. and Schwartz, R. A.: 1987, *Astrophys. J.* **312**, 462.

Lu, E. T. and Petrosian, V.: 1990, *Astrophys. J.* **354**, 735.

Papagiannis, M. D. and Kogut, J. A.: 1975, AFRCL-TR-75-0430.

Petrosian, V.: 1989, in E. R. Priest and V. Krishan, (eds.), *Basic Plasma Processes On The Sun*, IAU Symp. No. 142, p. 391.

Petrosian, V.: 1973, *Atrophys. J.* **186**, 291.

Ramaty, R.: 1969, *Atrophys. J.* **158**, 753.

Schmahl, E. J., Kundu, M. R., Strong, K. T., Bentley, R. D., Smith, J. B., and Krall, J. R.: 1982, *Solar Phys.* **80**, 233.

Shibasaki, K., Chiuderi Drago, F., Melozzi, M., Slottje, C., and Antonucci, E.: 1983, *Solar Phys.* **89**, 307.

Shimabukuro, F. I.: 1972, *Solar Phys.* **23**, 169.

Stähli, M., Gary, D. E., and Hurford, G. J.: 1989, *Solar Phys.* **120**, 351.

Stähli, M., Gary, D. E., and Hurford, G. J.: 1990, *Solar Phys.* **125**, 343.

Švestka, Z.: 1976, *Solar flares*, D. Reidel Publishing Co.

Takakura, T.: 1960, *Publ. Astron. Soc. Japan* **12**, 325.

Takakura, T.: 1967, *Solar Phys.* **1**, 304.

Takakura, T.: 1973, in R. Ramaty and R. G. Stone, (eds.), *High Energy Phenomena on the Sun*, NASA/GSFC-SP-342, p. 179.

Vilmer, N., Kane, S. R., and Trottet, G.: 1982, *Astron. and Astrophys.* **108**, 306.

White, S. M., Thejappa, G., and Kundu, M. R.: 1992, *Solar Phys.* **138**, 163.

Zheleznyakov, V. V.: 1970, *Radio Emission of the Sun and Planets*, Pergamon Press, New York.

Zlotnik, E. Ya.: 1968a, *Soviet Astron.* **12**, 245.

Zlotnik, E. Ya.: 1968b, *Soviet Astron.* **12**, 464.

Chapter 2

Microwave diagnostics of the coronal magnetic fields

Published in the **Solar Physics**, Vol. 144

Abstract

From the gyroresonance brightness temperature spectrum of a sunspot, one can determine the magnetic field strength by using the property that microwave brightness is limited above a frequency given by an integer-multiple of the gyrofrequency. In this paper, we use this idea to find the radial distribution of magnetic field at the coronal base of a sunspot in the active region, NOAA 4741. The gyroresonance brightness temperature spectra of this sunspot are obtained from multi-frequency interferometric observations made at the Owens Valley Radio Observatory at 24 frequencies in the range of 4.0 GHz - 12.4 GHz with spatial resolution 2.2″-6.8″. The main results of present study are summarized as follows: First, by comparison of the coronal magnetic flux deduced from our microwave observation with the photospheric magnetic flux measured by KPNO magnetograms, we show that the o-mode emission must arise predominantly from the second harmonic of the gyrofrequency, while the x-mode arises from the third harmonic. Second, the radial distribution of magnetic fields $B(r)$ at the coronal base of this spot (say, 2000-4000km above the photosphere) can be adequately fitted by

$$B(r) = 1420(1 \pm 0.080) \exp\left[- \left(\frac{r}{11.05''(1 \pm 0.014)} \right)^2 \right] \text{ G},$$

where r is the radial distance from the spot center at coronal base. Third, it is found that coronal magnetic fields originate mostly from the photospheric umbral region. Fourth, although the derived vertical variation of magnetic fields can be approximated roughly by a dipole model with dipole moment 1.6×10^{30} erg/G buried at 11000 km below the photosphere, the radial field distribution at coronal heights is found to be more confined than predicted by the dipole model.

1. Introduction

There have been many attempts to determine the strength and configuration of coronal magnetic fields over solar active regions by making use of the observed microwave emission from the regions, which are otherwise too transparent to many forms of radiation available in ground-based observations. Previous efforts along this line were made in two ways. One is to do a model-fit to the field configuration which can reproduce the spatial distributions of microwave brightness over the active region imaged at one or a few frequencies. The other approach is to use the microwave spectrum to exploit its sensitive dependence on the magnetic field strength.

The first approach is made in a number of studies, where very large arrays such as WSRT or VLA are used to yield high-spatial resolution microwave maps (e.g., Kundu, Becker, and Velusamy, 1974; Kundu and Alissandrakis, 1984; Lang, Wilson, and Gaizauskas, 1983; Chiuderi-Drago, Alissandrakis, and Hagyard, 1987). Often, observations in different regimes such as X-ray and UV were performed simultaneously to provide the physical parameters required for the model-computation (e.g., Schmahl *et al.*, 1982; Shibaski *et al.*, 1983). The second approach permits a more direct determination of the coronal field strength, but is limited to a few telescopes such as RATAN-600 and the array at Owens Valley Radio Observatory (OVRO) which are capable of observing at many frequencies (e.g., Akhmedov *et al.*, 1982; Krüger *et al.*, 1986; Hurford and Gary, 1986). Obviously, a more complete implementation of microwave observation as an independent diagnostic tool would be possible if both spatial and spectral resolutions were achieved at the same time.

We report, in this paper, such an implementation made possible by the multi-frequency, interferometric observation of a simple sunspot with the OVRO Solar Array. The basic strategy of this paper is similar to that of Hurford and Gary (1986) in that the spectral behavior of microwave brightness temperature and source size are used as a means to determine the coronal magnetic fields. The difference is that

this approach aims at empirical determination of the coronal magnetic field as a function of radial distance while Hurford and Gary (1986) sought a dipole magnetic field model by which the observed microwave spectrum can be reconstructed. For this particular purpose, we choose data obtained from microwave observations of the active region, NOAA 4741, at OVRO on 1986 August 2. These data have several distinct advantages over previous ones gathered at OVRO for many years. Owing to the fact that solar activity was at its lowest at that time, NOAA 4741 was the only active region on the solar disk, which avoids the problem of confusion by other sources. We have observations over many days while the region transitted the solar disk, which will be presented in a second paper (Lee, Gary, and Hurford, 1993). This paper concentrates on the unique information that can be gained when the region is nearest the disk center and thus the projection effects can be ignored. The active region was an exceptionally simple, single round sunspot on both white-light images and magnetograms, which allows us to assume radial symmetry. The plan of this paper is as follows. In Section 2, we describe the observational techniques. In Section 3, we identify the radiation mechanism and discuss its diagnostic potential for detecting the magnetic field strength. In Section 4, we present the procedure and result of the coronal magnetic field determination. Finally, our approach and results are discussed in Section 5.

2. Observation

2.1. SOURCE

The source region, NOAA 4741, passed the central meridian on 1986 August 2 at a latitude of N10°. No significant activity was observed during the whole day and thus we attempt mapping of this active region using earth-rotation synthesis with the three-element interferometer at OVRO to get the spatial information on the microwave emission.

2.2. INSTRUMENT SETUP AND IMAGING

The observation was made with the frequency-agile radio array at OVRO, operating with three antennas. The three baselines were formed from a pair of 27 m antennas and a 40 m antenna, which all lay along the East-West direction at the time. The maximum separation was 1067 m. The amplitudes and phases of the source for both polarizations were gathered at three baselines and the calibrator observations were also made to provide gain and phase corrections. Imaging was done by standard earth-rotation synthesis technique to yield two-dimensional contour maps of brightness temperature at each desired frequency. However, due to the baselines all lying in the East-West direction, the synthesized beams appear highly elongated along the North-South direction. We thus limit our measurement to the East-West direction which gives the highest resolution. For 4.0 GHz $\leq \nu \leq$ 12.0 GHz, the FWHM of the synthesized beam along this direction varies in the range of $6.8''$ - $2.2''$ which is less than half of the FWHM of image. Some of the resulting one-dimensional maps are shown in Figure 1 where the brightness temperatures for both right and left circular polarization are shown as a function of radial distance and frequency. In this figure, the vertical scale is set to a common value of 1.2×10^6 K. As can be learned by comparison of the beam width with the source width, the source is only marginally resolved. Therefore, we do not regard some of fine structures in anomalous asymmetry as worthy of detailed analysis. However, the full width of the brightness distribution is less than the beam width at each frequency and thus we consider them for use in the following analysis.

3. Radiation Mechanism and Diagnostics of Coronal Magnetic Field

In the present data as shown in Figure 1, the radiation mechanism can be identified readily by looking at how the brightness temperature drops at high, optically thin frequencies. Similar to Hurford and Gary's (1986) result, we notice from Figure 1 that the peak brightness temperature of this spot is constant at low frequencies, then declines sharply above 6 GHz with large degree of circular polarization. Such spectral behavior is expected for gyroresonance radiation.

In the gyroresonance spectrum, the sharp drop of brightness temperature above a certain frequency (hereafter called 'limiting frequency') is due to lack of sufficiently strong magnetic fields in the corona to maintain the radiation power at higher frequencies (see Gary and Hurford, 1987). As a result, the observed limiting frequency, ν_l, can be related to the magnetic field, B, of the radiating region as

$$\nu_l = 2.8nB, \tag{1}$$

where ν_l is in units of GHz and B in kG. The harmonic number, n, in this expression should be the maximum harmonic above which the medium is no longer opaque to the radiation. Due to the dependence of the opacity on wave mode, we separately denote the harmonic for the right-circularly polarized waves as n_R and that for left-circularly polarized waves as n_L. Note that right and left polarization states correspond to the ordinary and the extraordinary modes, respectively, for the radiation from this spot with the negative magnetic polarity. The above equation states that the magnetic field can be determined locally if both the limiting frequency and the corresponding harmonic are specified.

It seems appropriate to address here the problem that we face in order to determine the magnetic field strength by using the above condition. By multi-frequency observations with spatial resolution, we can derive the limiting frequency, ν_l, as a function of position. This information by itself is not sufficient, however. We must also determine the corresponding harmonic as a function of position. Although the presumed harmonics for a typical sunspot condition are in narrow ranges like $n = 2$ or 3 for the ordinary mode and $n = 3$ or 4 for the extraordinary mode (Zheleznyakov, 1970; Takakura, 1972; Holt and Ramaty, 1969; Ramaty and Petrosian, 1972), depending on the choice of a harmonic, uncertainty of the resulting field strength can be as high as 50% (Dulk and McLean, 1978). For this reason, we will expend some effort below in determining the appropriate harmonic as well as the limiting frequencies. Once these are determined, we can use Equation (1) to

find the coronal field strength as a function of position, as will be shown in the next section.

4. The Coronal Magnetic Field: Its Strength and Radial Distribution

4.1. THE LIMITING FREQUENCY AS A FUNCTION OF RADIAL DISTANCE

As mentioned earlier by Hurford and Gary (1986), a more formal technique is to construct a spectrum at each point of interest to decide the limiting frequency at the position. For a symmetric sunspot, however, we can assume that the magnetic field strength decreases radially outward from the spot center. In this case, the observed gradual decrease of source size with frequency (see Figure 1) reflects the fact that the imaged region is being confined to the inner sunspot region with stronger field as the observing frequency increases.

Following this reasoning, we assign the limiting frequency as the observing frequency at the position where the boundary of the source occurs. To quantify the source boundary, we set it to the point where the brightness profile crosses two levels, either 10% or 30% of the peak brightness temperature in Figure 1. After converting the limiting frequency, ν_l, to the nB values using (1), we plot the curves for the two values Figure 2 as a function of radial distance, which is set to half the source width. In the figure, the open and filled rectangles correspond to the choices of 10% and 30% level boundaries, respectively. For example, consider the profiles labelled 5.6 GHz in Figure 1. The left-circularly polarized source, marked with crosses in the figure, has a full width of about $15''$ at the 10% level, and about $12''$ at the 30% level. On Figure 2a, then, the 5.6 GHz points, which correspond to $nB = 2000$G, are plotted as a filled box at $r = 6''$ (half the measured full width) for the 30% level and an open box at $r = 7.5''$ for the 10% level. Following this procedure for each frequency and polarization yields the curves in Figure 2. Figure 2 gives nB as a function of radial distance across the sunspot. Now we need only to determine n in order to get the actual magnetic field strength.

4.2. A GEOMETRICAL FORM FACTOR OF THE CORONAL FIELD DISTRIBUTION

One problem we have is that the harmonic number, n, may vary with position. In that event, the use of Equation (1) to determine magnetic field strength is complicated, and also the resulting field values do not pertain to a common coronal height. The latter is due to the fact that the locus of the gyroresonance layer varies with harmonic and frequency for a given magnetic configuration (see Zlotnik, 1968). However, such a variation of harmonic is likely to be detectable, since n can take only low integer values (see Section 3). If the harmonic changes its value somewhere along a smoothly varying field structure, a discontinuity must show up in the nB distribution. As seen in Figure 2(a), such a behavior appears in the $n_L B(r)$ distribution while $n_R B(r)$ appears to be smooth as we see in Figure 2(b). This implies that n_R is constant along the radial distance, in which case we can use the $n_R B$ distribution to derive a field distribution at a height of the source layer.

Without specifying the value of n_R at this point, we can use the fact that n_R is constant to find a geometrical form for the radial dependence of the magnetic field from Figure 2b, in terms of n_R. After trying several geometric forms, we found that a gaussian form fits closely the $n_R B$-distribution. Depending on the choice of boundary level, we have the field strength at spot center of either $(3070/n_R)$ G for the 10% level or $(2620/n_R)$ G for the 30% level. However, the 1/e half-width of the field distribution appears to be fairly insensitive to the choice of the boundary level; it is 11.2″ for 10% level and 10.9″ for 30% level. Taking these as the possible range of those values, we use their mean and deviation to represent the coronal field distribution as

$$B_c(r_c) = \frac{2840(1 \pm 0.080)}{n_R} \exp\left[- \left(\frac{r_c}{11.05''(1 \pm 0.014)} \right)^2 \right] \quad \text{G}, \qquad (2)$$

where n_R is constant with radial distance, r_c, at a coronal height. Note that the

error range in the above expression is a result of choosing the 10% or 30% level as the boundary level and thus it does not preserve the standard statistical meaning.

4.3. EFFECTIVE HARMONIC NUMBER AND CORONAL FIELD STRENGTH

The value of n_R in (2) is yet to be determined for final evaluation of the coronal field strength. For this purpose, we consider the magnetic flux at the corona and that at the photosphere separately, because they are calculable with data at hand and can be related by the principle of magnetic flux conservation, leaving n_R as the only unknown parameter.

We determine the photospheric magnetic flux by reading the KPNO magnetogram under the assumption of radial symmetry. Since this sunspot was passing the central meridian at low latitude ($\simeq 10^\circ$), the longitudinal field recorded on the magnetogram can be taken as being close to the normal component to the spot surface area. The KPNO magnetogram, however, showed a saturation at around 1100 G. As the Mt. Wilson data (courtesy of Tom Shieber), which is free of saturation, gives the peak value of 2400 G, we made a fit to recover the saturated portion. Again, a gaussian form appears to fit both the unsaturated portion of the magnetogram and the peak value provided by Mt. Wilson data as a whole with the gaussian width of $9.9'' \pm 1.0''$. Since the error in Mt. Wilson data is ± 100 G (Tom Shieber, private communication), we express the photospheric field distribution as $B_p(r_p) = 2400(1 \pm 0.04)e^{-(r_p/9.9'' \pm 1.0'')^2}$G, where r_p is the radial distance from the spot center on the photosphere. On integration of $B_p(r_p)$ over a spot area within radius r_p, we can find the photospheric flux within the area, $\Phi_p(r_p)$, as

$$\Phi_p(r_p) \equiv \int_0^{r_p} \mathbf{B}_p \cdot d\mathbf{a} \approx 3.9(1 \pm 0.04) \times 10^{21} \left[1 - e^{-(r_p/9.9'' \pm 1.0'')^2}\right] \mathrm{Mx}, \quad (3)$$

where $d\mathbf{a}$ is an element of spot area parallel to the solar surface and Mx represents the Maxwell unit of magnetic flux.

The calculation of the coronal magnetic flux is not so straightforward, because the magnetic field, B_c, found in Equation (2) is not the normal component to the surface but is the total field strength. However, we do not need to determine the coronal magnetic flux to great accuracy because we want to find the harmonic number which can take only an integer value. All we need in this case is to assess a probable range of coronal magnetic flux to rule out the wrong harmonic number. If use is made of B_c given by Equation (2), the resulting value should be regarded as an *upper bound* for the coronal magnetic flux, since the normal component cannot exceed the total strength, i.e., $B_\perp \leq B_c$. To get a *lower bound*, we can assume a distribution of tilt angle of coronal fields as measured from the sunspot normal. In an analogy of the tilt angle distribution found in sunspots at the photosphere (Zirin, 1992), we consider a coronal tilt-angle, α_c, which increases linearly with distance from the center, and drops to zero at the boundary. For the boundary of this gaussian distribution, we take $r_c \approx 19''$ where the field decreases to 5% of its maximum value at spot center. Under this assumption, we set the coronal tilt angle as $\alpha_c \sim 90^\circ (r_c/19'')$ for $r_c \leq 19''$ but $\alpha_c \sim 90^\circ$ for $r_c > 19''$ to give a reasonable lower bound for the normal component of the coronal magnetic fields. We then have the possible range of the coronal magnetic flux as

$$\frac{2840\mathrm{G}}{n_R} \int_0^{r_c} e^{-(r/11.05'')^2} \cos\alpha_c(r) 2\pi r dr \leq \Phi_c(r_c) \leq \frac{5.76\times10^{21}}{n_R}\left[1 - e^{-(r_c/11.05'')^2}\right]\mathrm{Mx} . \quad (4)$$

We now compare (3) with (4) to determine which value of n_R is consistent with the notion of magnetic flux conservation with height. First of all, the total magnetic flux of the corona should not exceed that of the photosphere, but this condition is satisfied for the choice of both n_R= 2 and 3. Therefore, we require a more strict constraint by comparing the magnetic flux as a function of radial distance at both the photosphere and the corona for agreement. If the field lines lying within a

radius r_p at the photosphere are extended to the corona with tilt angle α_p, they will occupy a coronal region of radius, $r_c = r_p + h \tan \alpha_p$, where h is the height of the corona from the photosphere. In terms of magnetic flux, this relation will be expressed as

$$\Phi_p(r_p) \approx \Phi_c(r_p + h \tan \alpha_p), \tag{5}$$

if the field lines keep the same tilt angle up to the corona. We can expect this approximate equality to be good near the spot center because α_p is small, and the field lines are more rigid there. At a large distance from the spot center, however, $\Phi_c(r_p + h \tan \alpha_p)$ will fall below $\Phi_p(r_p)$, as the tilt angle of the curved, outer region field lines tends to increase more with height, i.e., $r_c > r_p + h \tan \alpha_p$. Thus, we may rule out a harmonic that fails to match the photospheric magnetic flux at small r_p. In Figure 3, we plot the photospheric flux given by (3) and the coronal magnetic fluxes by (4) as a function of radial distance. To relate the photospheric radius r_p with the coronal radius $r_c = r_p + h \tan \alpha_p$, we use the empirical law of the tilt-angle distribution at the photosphere found by Zirin (1992):

$$\alpha_p = 14^\circ + 62^\circ \frac{r_p}{R} \qquad (0.4 \leq r_p/R \leq 1), \tag{6}$$

where R is the total radius of the sunspot at the photosphere. In the present calculation, we take R $\approx 17''$ from the magnetogram and $h = 4''$ as a typical coronal height.

At large r_p ($r_p/R \geq 0.7$), the coronal magnetic flux for either choice of harmonic comes out less than the photospheric value where no distinction can be made due to the uncertainty regarding the height variation of the tilt angle. Near the umbra ($r_p/R \sim 0.5$), however, an agreement is found between the photospheric magnetic flux $\Phi_p(r_p)$ and that of the corona $\Phi_c(r_c)$ computed for n_R=2, while the coronal

flux for n_R=3 falls everywhere well below $\Phi_p(r_p)$. Therefore, we regard $n_R = 2$ as the appropriate harmonic for the o-mode and finally determine the field distribution from (2) as

$$B_c(r_c) = 1420(1 \pm 0.080) \exp\left[- \left(\frac{r_c}{11.05''(1 \pm 0.014)} \right)^2 \right] \text{ G.} \qquad (7)$$

This field distribution will pertain to a height near the base of the corona where the electron temperature makes a rapid transition from 1.2×10^5 °K to below.

The harmonic for the left-circularly polarized waves (x-mode) also deserves some comment. According to model calculation with theoretical gyroresonance opacity (e.g., Zheleznyakov, 1970, his Table 6; see also Lee, Gary, and Hurford, 1992), the harmonic for x-mode is expected to be greater than that for o-mode by unity except when the angle between the magnetic field and observer is close to 0° or 90°. Therefore, we suggest $n_L = n_R + 1 = 3$ as the appropriate harmonic for the region where the distribution of $n_L B$ is similar to that of $n_R B$ in Figure 2, i.e., $r \geq 3''$-$5''$. The presence of the discontinuous jump of $n_L B$ near the spot center ($r \leq 3''$-$5''$) is then interpreted as being due to the change of n_L from 3 to lower values as gyroresonance opacity at the third harmonic gets lowered at small tilt angles of field lines near the spot center. Since lower harmonic layers occur at regions of stronger magnetic fields, the increase in B can cause an increase in $n_L B$ in spite of lowered n_L, as shown in Figure 2(a). This downward change of n_L can also explain the lowered brightness temperature for x-mode at spot center shown in Figure 1. Unfortunately, the magnetic structure implied by our data for left-circularly polarized radiation cannot be explored, since the transition of n_L from 3 to 2 and 2 to 1 appears to be more rapid within the narrow core region than we can follow with our spatial resolution.

4.4. IMPLICATION FOR THE VERTICAL MAGNETIC STRUCTURE

In the previous section, a somewhat lengthy consideration was given to the magnetic fluxes and field tilt angles at two heights solely to figure out the appropriate harmonic number. Here, we show that they can also be used to yield an interesting implication for the vertical magnetic structure of this spot.

Since the total magnetic flux at the corona is found to be less than that at the photosphere (i.e., $\Phi_p(\infty) > \Phi_c(\infty)$), it must be that not all but only a portion of the photospheric field lines reach the coronal height. We thus consider a photospheric radius, r_o, from which all of coronal magnetic flux should originate. We can find r_o from the condition $\Phi_p(r_o) = \Phi_c(\infty)$. From (3) and (4) including the stated uncertainties, we calculate r_o defined above to find that $8.0'' \leq r_o \leq 11.4''$ with corresponding tilt angles in the range $43^\circ \leq \alpha_p \leq 56^\circ$ from (6). With these results, we depict, in Figure 4, the range of these border field lines extending from r_o to the corona under the assumption that they keep the same tilt angles all the way to the corona. If, as is likely, the tilt angle increases further with height, the field lines starting from upper bound radius, $r_o = 11.4''$, may deviate from the observed coronal microwave image size, $R_{cor} = 19''$, as shown in Figure 4. It is, therefore, reasonable to presume that r_o takes a value from $8.0''$ to somewhat less than $11.4''$ in order to match the size of coronal active region implied by the magnetic flux to the measured size of the microwave image. In this case, we find, from Figure 4, that r_o is much closer to the umbral size than the size out to the penumbral boundary. This leads us to conclude that the coronal field lines must be rooted mostly in the photospheric umbral region. It is then implied that the photospheric umbral fields and the whole of the coronal fields should be regarded as a unit, with the penumbral field lines diverging so rapidly that they do not penetrate into the corona.

5. Discussion and Conclusion

It has been thought for many years that the sensitive dependence of gyroresonance spectrum on magnetic field would permit a direct measurement of the field strength

of the coronal active region. In general, this becomes possible only after the harmonic number, n, is uniquely determined (see Equation (1)). In this paper, we took several steps to determine the value of n by combining high frequency resolution observations and magnetogram observations of a round spot located near disk center. This approach was found to be useful not only because it enables the empirical determination of coronal magnetic field strength but also because it sheds light on the relationship between the coronal fields and the photospheric umbral fields.

As a result, we found that the magnetic field at the coronal base varies in the horizontal direction in a gaussian form with $1/e$ half-width of $\sim 11''$. Comparing with the Mt. Wilson data, the maximum coronal strength of ~ 1400 G implies that the umbral fields decrease vertically by 40% in reaching the coronal base.

Many assumptions were made in various stages of the present study to arrive at the above result; it would be worth listing them all together. First, it is assumed that the field distribution is smooth and in circular symmetry, which is feasible due to the round appearance in the photosphere and the dominance of the magnetic pressure over the gas pressure in the corona. Second, we assumed that our measurement of the width of microwave images at all frequencies pertains to a same height. This approximation makes sense because the active region was near the center and thus there was no appreciable projection effect on the apparent source dimension at each frequency. Third, we used several parameters arbitrarily chosen. For example, we use the position where the brightness temperature falls off to 10% - 30% of the peak value as the boundary. The resulting field strength at center varies by 8.0%, according to which choice is made. The corresponding change in the scale radius is even less, only 1.4%. We take the coronal height $h = 4''$ as a typical value. It can be easily shown that even for $2'' < h < 6''$, the choice of $n_R = 2$ does not change. This wide range of h will certainly span the real coronal height. Therefore, the present result is quite insensitive to the choice of these parameters. Fourth, we assumed tilt-angle distributions of fields at the corona and the photosphere in order to compare the magnetic fluxes at both heights. The coronal tilt angles are chosen

similar to that of the photosphere which can be justified, on average, on empirical grounds (Zirin, 1992).

In previous attempts to determine the coronal field strength, model computations were usually made to check which field distribution is capable of reproducing the principal characteristics of the observation (e.g., Alissandrakis, Kundu, and Lantos, 1980; Gelfreikh and Lubyshev, 1979; Krüger *et al.*, 1986; Schmahl *et al.*, 1982). Although such a task was not necessary in the present approach, it would still be useful to see whether our result is reproduced by any theoretical model. In Figure 5, we make a comparison of our result with the dipole model as a simplest theoretical one. It appears that the photospheric field is well approximated by a dipole model with dipole moment 1.6×10^{30} erg/G buried at 11000 km below the photosphere. However, the same dipole model fails to fit the coronal fields derived in this paper, in that it predicts a broader width of the field distribution than found in the present study (see Figure 5). It seems that the height variation of the field strength at spot center can be roughly described by the dipole model, but that the radial distribution of the real sunspot field is more confined than that predicted by the dipole model.

Acknowledgements

We are grateful to Harold Zirin for many helpful suggestions and comments. We wish to thank Tom Shieber for providing Mt. Wilson data and Norman W. Murray for his help in reading the KPNO magnetic tapes. This work was funded by NSF grants ATM-9013173 and AST-8919770 and by NASA grant NAGW-3005 to the California Institute of Technology.

REFERENCES

Akhmedov, Sh. B., Gelfreich, G. B., Bogod, V. N., and Korzhavin, A. N.: 1982, *Solar Phys.* **79**, 41.

Alissandrakis, C. E., Kundu, M. R., and Lantos, P.: 1980, *Astron. Astrophys.* **82**, 30.

Chiuderi Drago, F., Alissandrakis, C., and Hagyard, M.: 1987, *Solar Phys.* **112**, 89.

Dulk, G. A. and McLean, D. J.: 1978, *Solar Phys.* **57**, 279.

Gary, D. E. and Hurford, G. J.: 1987, *Astrophys. J.* **317**, 522.

Gelfreikh, G. B. and Lubyshev, B. I.: 1979, *Soviet Astron.* **23**, 316.

Holt, S. S. and Ramaty, R.: 1969, *Solar Phys.* **8**, 119.

Hurford, G. J. and Gary, D. E.: 1986, *Coronal Processes and Plasmas*, Nasa Conference Proc. 2442, p. 319.

Krüger, A., Hildebrandt, J., Bogod, V. M., Korzhavin, A. N., Akhmedov, Sh. B., and Gelfreikh, G. B.: 1986, *Solar Phys.* **105**, 111.

Kundu, M. R. and Alissandrakis, C. E.: 1984, *Solar Phys.* **94**, 249.

Kundu, M. R., Becker, R. H., and Velusamy, T.: 1974, *Solar Phys.* **240**, L63.

Lang, K. R., Wilson, R. B., and Gaizauskas, V.: 1983, *Astrophys. J.* **267**, 455.

Lee, J. W., Gary, D. E., and Hurford, G. J.: 1993, *Solar Phys.* **144**, 349.

Ramaty, R. and Petrosian, V.: 1972, *Astrophys. J.* **178**, 241.

Schmahl, E. J., Kundu, M. R., Strong, K. T., Bentley, R. D., Smith, J. B., and Krall, J. R.: 1982, *Solar Phys.* **80**, 233.

Shibasaki, K., Chiuderi Drago, F., Melozzi, M., Slottje, C., and Antonucci, E.: 1983, *Solar Phys.* **89**, 307.

Takakura, T.: 1972, *Solar Phys.* **26**, 151.

Zheleznyakov, V. V.: 1970, *Radio Emission of the Sun and Planets*, Pergamon Press, New York.

Zirin, H.: 1992, in preparation.

Zlotnik, E. Ya.: 1968, *Soviet Astron.* **12**, 245.

FIGURE CAPTIONS

Fig. 1. One-dimensional maps of the brightness temperature at several frequencies. The brightness temperatures are all normalized to a common value of 1.2×10^6 K. r is the radial distance measured from the spot center along the East-West direction. The crosses and circles represent the brightness in left and right circular polarization, respectively. The synthesized beam width is also shown at each frequency in the upper left corner.

Fig. 2. Distribution of nB over the radial distance r for (a) the left-circularly polarized waves and (b) the right-circularly polarized waves. The scales of the corresponding limiting frequency are shown to the right side of the ordinate. Open and filled rectangles correspond to the choice of boundary at 10% and 30% level of the peak brightness temperature.

Fig. 3. The allowed ranges of the photospheric magnetic flux, Φ_p, and the coronal magnetic flux, Φ_c, as a function of radial distance normalized to $R = 17''$, the radius of the photospheric sunspot. r_p and r_c are the radial distances at the photosphere and the corona, respectively, which are related by $r_c = r_p + h\tan\alpha_p$. Here, h is the coronal height taken as $4''$ and α_p is the tilt angle of photospheric fields given by (6). The ranges for Φ_p and Φ_c at $n_R = 3$ do not overlap, indicating that the o-mode emission from the spot cannot be due to the third harmonic of the gyrofrequency.

Fig. 4. A schematic diagram showing the possible inclination of the photospheric field lines reaching the boundary of the coronal active region. R_{cor} and R_{ph} are the effective radius of the sunspot at the corona and at the photosphere, respectively. r_{um} is the mean radius of the umbra at the photosphere. Two boundary radii r_o are also shown (see text for definition).

Fig. 5. Comparison of the derived field distribution with that of the dipole model. (a) The photospheric magnetic field distribution: Circles are KPNO magnetogram

data read along east-west direction (open circles) and north-south direction (filled circles) passing through the spot center. Due to saturation of KPNO magnetogram above 1100 G, Gaussian fit and a dipole model fit are made to recover the peak value of 2400 G given by Mt. Wilson data. (b) The coronal magnetic field distribution: Circles are data obtained after dividing the measured $n_R B$ values (see Figure 2) by $n_R = 2$. The same dipole model shown in (a) is used to compute the coronal field distribution for several heights of corona and then compared with the gaussian fit to the microwave data. r_c and r_p refer to radial distance at the corona and the photosphere, respectively.

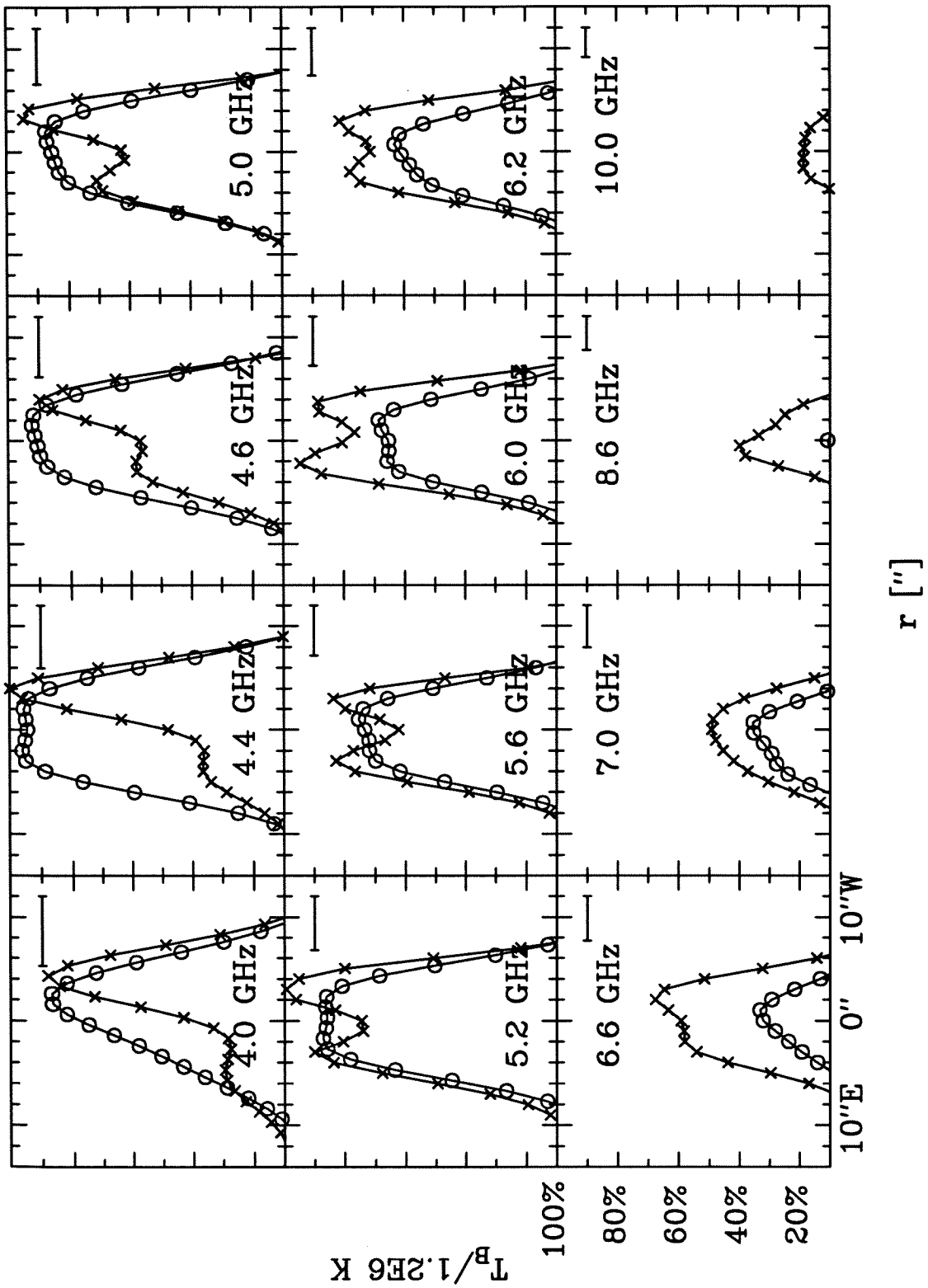
4.0 GHz
4.4 GHz
4.6 GHz
5.0 GHz
5.2 GHz
5.6 GHz
6.0 GHz
6.2 GHz
6.6 GHz
7.0 GHz
8.6 GHz
10.0 GHz
10"E
0"
10"W
r ["]
100%
80%
60%
40%
20%
T_B/1.2E6 K

Figure 1

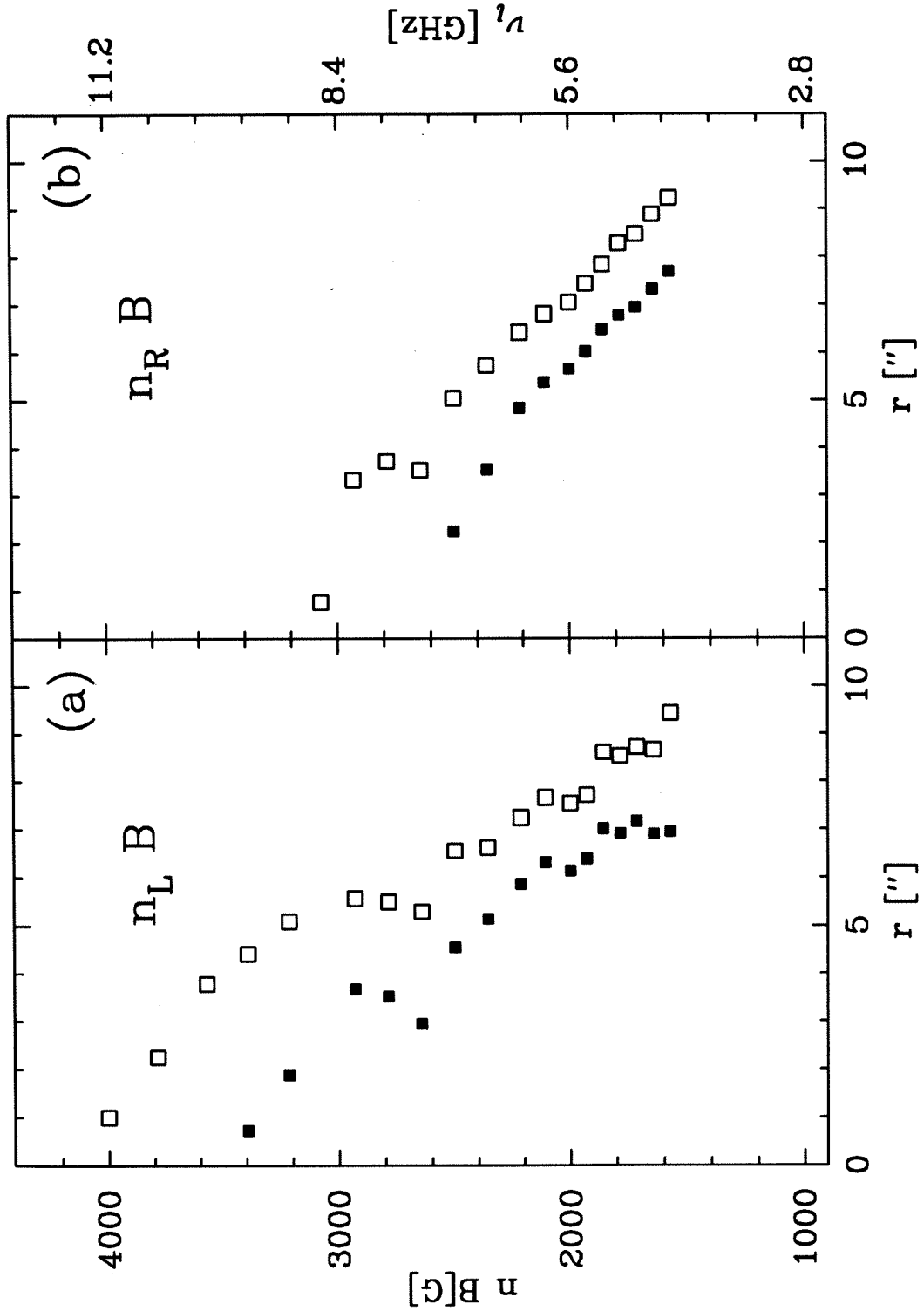

Figure 2

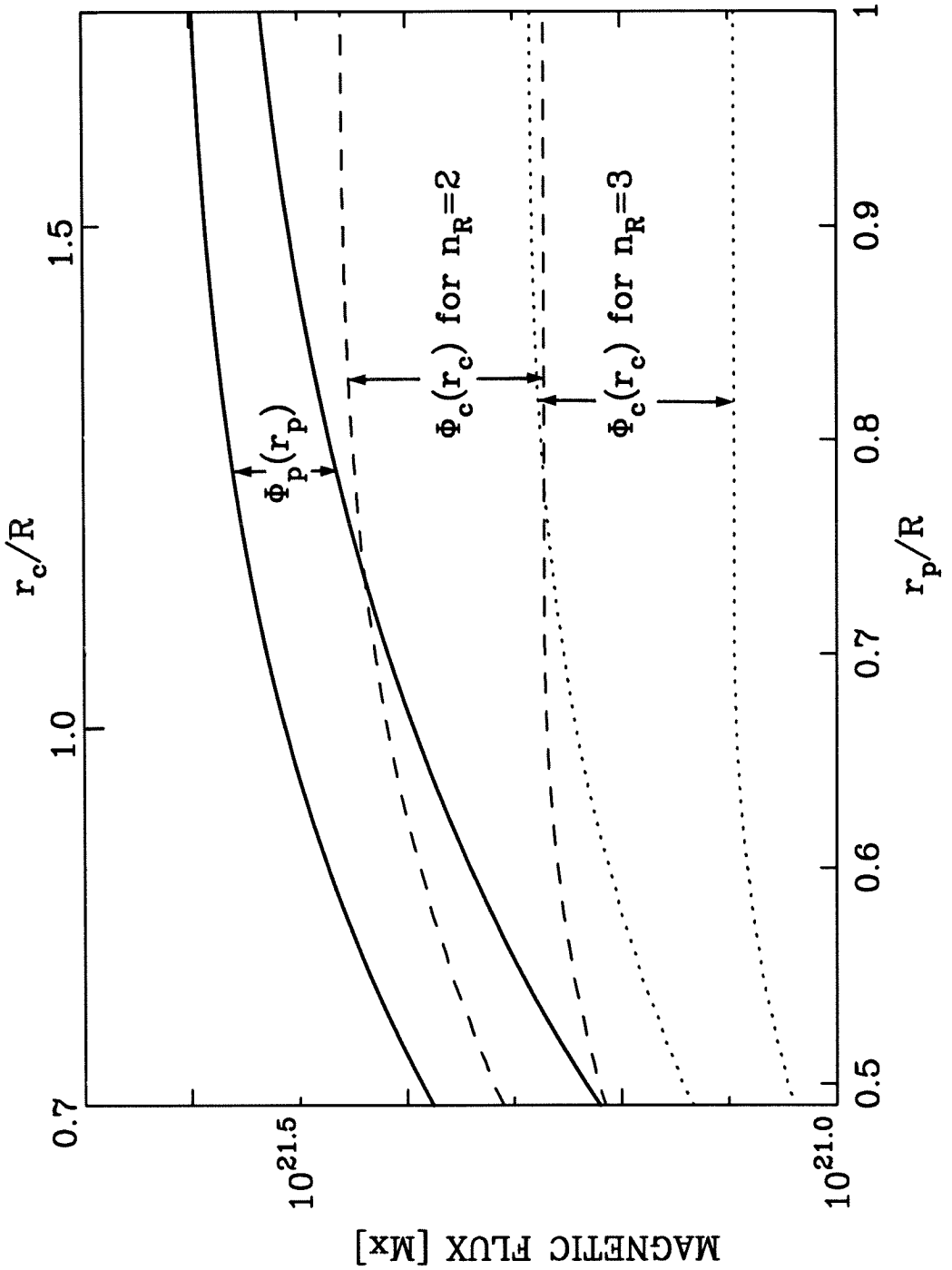
MAGNETIC FLUX [Mx]
$10^{21.5}$
$10^{21.0}$
r_c/R
r_p/R
0.7
1.0
1.5
0.5
0.6
0.7
0.8
0.9
1
$\Phi_p(r_p)$
$\Phi_c(r_c)$ for n_R=2
$\Phi_c(r_c)$ for n_R=3

Figure 3

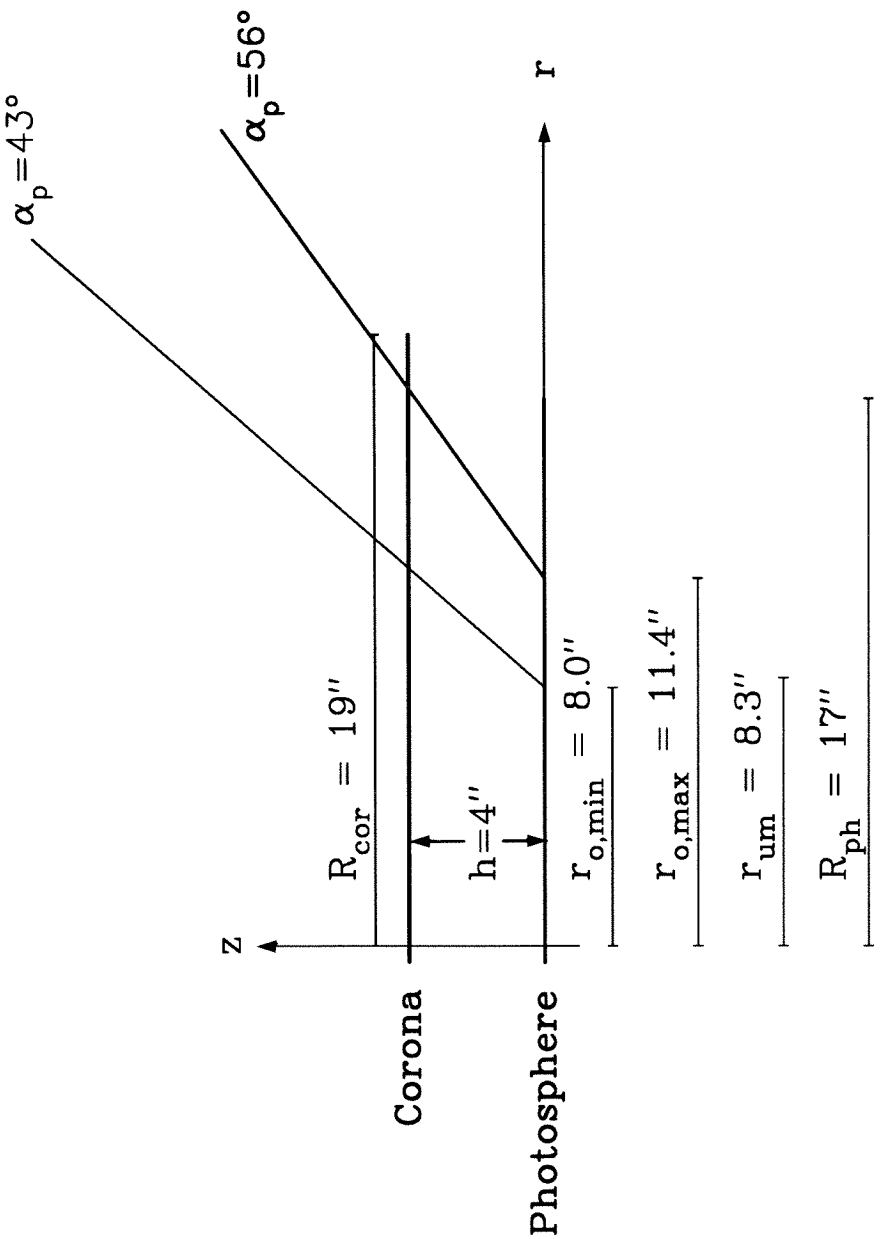
α_p=43°
α_p=56°
r
z
R_{cor} = 19''
h=4''
$r_{o,min}$ = 8.0''
$r_{o,max}$ = 11.4''
r_{um} = 8.3''
R_{ph} = 17''
Corona
Photosphere

Figure 4

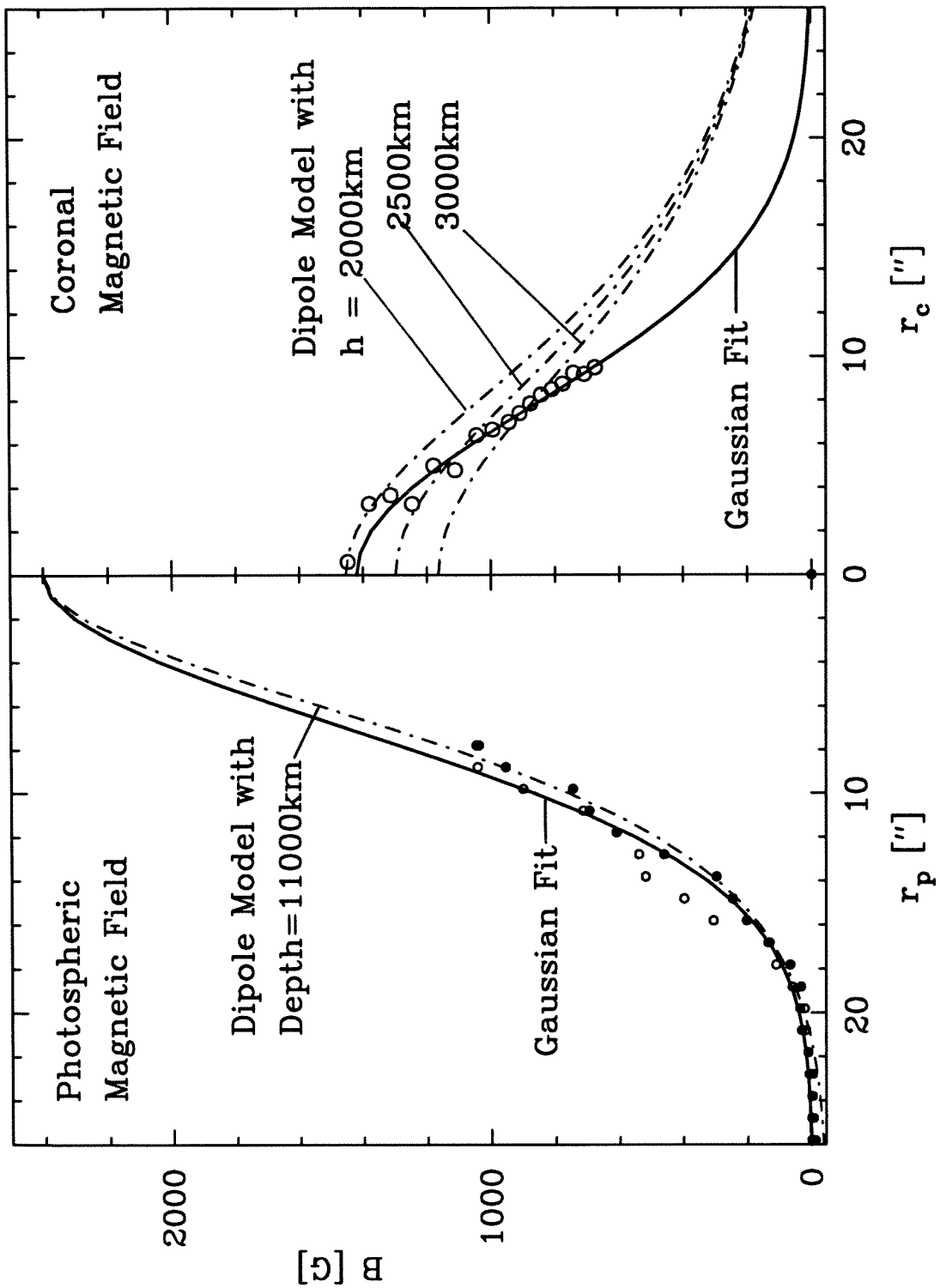
Photospheric
Magnetic Field
Dipole Model with
Depth=11000km
Gaussian Fit
B [G]
2000
1000
0
20
10
0
r_p ["]
Coronal
Magnetic Field
Dipole Model with
h = 2000km
2500km
3000km
Gaussian Fit
20
10
0
r_c ["]

Figure 5

Chapter 3

Center-to-limb variation of microwave radiation

Published in the **Solar Physics**, Vol. 144

Abstract

A series of microwave observations of a sunspot in the active region NOAA 4741 was made with the Owens Valley Solar Array for the purpose of investigating the center-to-limb variation of both the spectral and spatial brightness distribution. In this investigation, several properties of the sunspot microwave radiation are found. First, sunspot microwave emission appears in two typical profiles depending on the heliocentric position of the spot: either the ring structure near disk center or single-peak structure near the limb. Second, the brightness temperature at high, optically thin frequencies (> 6 GHz) increases slightly as the spot approaches the limb, which we interpret as being due to the increase of the gyroresonance opacity of the field lines near the spot center as they gain greater viewing angles. Third, the center-to-limb variation of the gyroresonance spectrum seems to be mostly characterized by a change of effective harmonic, which accompanies a discontinuous change of the degree of polarization. Fourth, a change of spectrum from gyroresonance to free-free emission is found in the passage of the spot over the solar limb, which gives a determination of the height of the gyroresonance layer to confirm its location low in the corona of the active region.

1. Introduction

Microwave emission from sunspots has been studied in detail for many years. Most initial studies were performed to confirm the hypothesis of gyroresonance radiation for the dominant mechanism (Zheleznyakov, 1962; Kakinuma and Swarup, 1962; Kundu *et al.*, 1977). Afterward observations were made with high resolution to reveal that microwave brightness above a sunspot exhibits a local depression feature, so called 'ring structure' (e.g., Alissandrakis and Kundu, 1982; Lang and Wilson, 1982), of which origin is still in debate (Strong, Alissandrakis, and Kundu, 1984). The inversion of circular polarization associated with the passage of bipolar active regions also attracted many observational and theoretical studies (see White, Thejappa, and Kundu, 1992 for recent review). It is also found that microwave radiation contains a wealth of information on the physical conditions in coronal active regions that can be exploited by both high-resolution maps (e.g., Alissandrakis, Kundu, and Lantos, 1980; Chiuderi-Drago, Alissandrakis, and Hagyard, 1987) and high-resolution spectra (e.g., Hurford and Gary, 1986).

In Paper I (Lee, Hurford, and Gary, 1993), we presented a completely empirical result for the coronal magnetic field distribution of an active region, NOAA 4741, where both spectral and spatial resolution were fully made use of. In the present paper, we report observations continued during the passage of the active region from the central meridian to the west limb. We note that these data provide an excellent opportunity for the study of the angle-dependent properties of microwave radiation, since NOAA 4741 was the only active region over the whole disk and retained its simple shape throughout the center-to-limb passage owing to the fact that solar activity was at a minimum. Of interest in this investigation is the positional variation of polarization and spatial profile of the microwave brightness above the active region, in relation to numerous theoretical predictions on the role of viewing angles in the apparent brightness profiles (e.g., Lantos, 1968; Zlotnik, 1968b). It is shown that the angle-dependence of the gyromagnetic opacity alone allows a consistent interpretation of the overall center-to-limb variation of microwave radiation

from the sunspot. We also find that occultation of the lower part of the active region by the solar limb provides an excellent opportunity to measure the physical parameters of the region such as the vertical scale height of coronal magnetic field and the height of the gyroresonance layer. The plan of this paper is as follows: We briefly describe the observation in Section 2. Results for spatial profiles and spectra of the brightness temperature are presented in Section 3. In Section 4, we discuss the physical parameters of the active region and the center-to-limb variation pattern of polarization derived from our data. Our main results are summarized in Section 5.

2. Observation

The source was the spot in the same active region, NOAA 4741, as reported in Paper I. This spot passed the central meridian on 1986 August 2 and passed over the west limb on 1986 August 9 at the heliocentric latitude of 10° N. We list, in Table I, the spot's heliolongitudes and the photospheric magnetic field strengths measured by Mt. Wilson magnetogram (Courtesy of Tom Shieber) on the days of observation. In this table, the heliocentric position refers to UT 20:00 each day and the error range of magnetic fields is ±100 G (Tom Shieber, private communication). For simplicity, the term 'longitude' will be used for the heliocentric longitude of the spot center throughout this paper. During the passage of the spot from disk center to west limb, there was no significant activity in this region and thus the interferometric observations were made during 6-8 hours per day to get spatial maps and an average spectrum each day using the method of rotational synthesis. The observations are made with the three-element, frequency-agile solar array at the Owens Valley Radio Observatory (OVRO). The array configuration and the synthesized beam were the same as described in Paper I. The data on August 3 was not processed due to activity that occurred on this day; the data of August 8 is missing due to a mechanical problem. Note that, on August 9, the spot has passed over the limb by 5° and thus its photospheric part was invisible, but the upper part of the active region could be observed in microwave wavelengths.

3. Results

3.1. SPATIAL PROFILES OF BRIGHTNESS TEMPERATURE

Figure 1 shows one-dimensional scans at several frequencies for each longitude. The profiles in each row are the brightness distribution obtained after interferometric observation for a day; the angle in each row is the longitude of the spot center on the day of observation. In the figure, thick solid lines represent brightness temperature for right-circularly polarized waves, T_R, and the thin lines for left-circularly polarized waves, T_L, both of which are normalized to the maximum peak brightness temperature on each day.

A general pattern found in this figure is the variation of the shape of the brightness profile with longitude. Central depressions appear in the profiles at small longitudes ($\theta < 45°$), while profiles at large longitudes ($\theta > 45°$) tend to show a single peak. The central depression feature looks similar to the 'ring structure' found by Alissandrakis and Kundu (1982) and Lang and Wilson (1982). This structure has been thought to be due to either the lowered gyroresonance opacity near spot center or the presence of cool material (Strong, Alissandrakis, and Kundu, 1984). Accordingly, we check whether either of these possibilities can explain the disappearance of the central depression at large longitude as well. In view of previous model calculations (e.g., Zlotnik, 1968b), the result that strong fields at spot center become transverse and thus optically thick at large longitudes may well give rise to a natural explanation for this phenomenon. On the other hand, the hypothesis of the cool material origin would also explain the disappearance of the central depression if the material were in a form of a thin slab so that its apparent dimension decreased by $\cos\theta$ at longitude θ. For example, the material of a width of the central depression seen on August 2 would look smaller by $\cos 55° \approx 55\%$ on August 6. Any feature intrinsically varying with polarization state or frequency will be helpful to distinguish the true origin between these two possibilities. Seemingly, the width of the central depression gets smaller with frequency; however, it can also be that

the physical width of the central depression is just below the beam width, which is decreasing with frequency. Therefore, it seems that neither of two possibilities can be ruled out by this data alone.

It appears that the degree of polarization also diminishes with longitude. The degree of polarization in the gyromagnetic radiation becomes high when the medium becomes optically thin in one circular polarization while remaining optically thick in the other. This happens when either the frequency is high or the viewing angle is small (see above). It is interesting to note that the polarization disappears after a certain longitude ($\theta > 60°$), regardless of frequency and position. This seems to imply a predominant role of viewing angle in the polarization structure.

At $0° < \theta < 90°$, the peak brightness temperature of each profile is about constant with frequency until $\nu \sim 6$ GHz, after which it drops steeply, as expected for gyromagnetic radiation. After the active region passed over the limb, however, the peak temperature shows an entirely different spectral behavior; that is, a rather gradual decrease with frequency. It thus seems that the dominant radiation mechanism has been changed after the spot passed over the west limb. We can better check this point in terms of high-resolution spectra, which we do in the next section.

3.2. BRIGHTNESS TEMPERATURE SPECTRA

Figure 2 shows spectra of peak brightness temperature, each of which is taken from a map generated at 30 frequencies between 3 and 18 GHz in both left and right circular polarizations. In this figure, two different spectral features are found. During August 2 - 6, the spectra appear all in the shape of a gyroresonance spectrum which is characterized by a sharp drop-off of the brightness temperature and high polarization at high frequencies (> 6 GHz). On August 7, the polarization at high frequencies has disappeared, but the overall shape still resembles a gyroresonance spectrum. On August 9, the gyroresonance emission that dominated the spectrum above 7 GHz on previous days is now gone. Instead a lower brightness temperature,

optically thin free-free emission, has appeared at $\nu > 7$ GHz, as manifested by its frequency dependence as slow as ν^{-2} (guided by the dotted line in Figure 2). We assume that this free-free emission was also present on previous days, but was masked by the brighter gyroresonance emission coming from the strongest field regions of the spot. It is therefore surmised that those field regions are located low in the corona, but occulted by the limb on August 9, allowing the less bright free-free emission to dominate the spectrum above 7 GHz.

Of interest in the gyroresonance spectra measured on August 2-7 is the longitudinal variation of limiting frequency and polarization. To quantify the limiting frequency, we read from Figure 2 the frequency at which the brightness temperature falls off to 30% of the optically thick value and plot it as a function of longitude in Figure 3. The figure shows that the limiting frequency increases slightly with longitude at $0° < \theta < 55°$. At first hand, it might be attributed to a growth of the active region magnetic field, since the limiting frequency is proportional to the magnetic field strength. On the other hand, Zlotnik's (1968b) model predicts that the maximum flux will shift toward higher frequency as strong fields at spot center become more transverse at high longitude and thus acquire higher gyroresonance opacity. Zlotnik's (1968b) idea seems more plausible in view of no appreciable change of the photospheric magnetic fields of this sunspot during the days of observation (see Table I).

To examine the longitudinal variation of circular polarization, we plot, in Figure 4, the degree of circular polarization defined by $P = (T_L - T_R)/(T_L + T_R)$ where T_R and T_L are taken from Figure 2. Although the frequency dependence is noisy (due primarily to beam squint of the spiral feeds), it is clear that the degree of circular polarization remains more or less constant with longitude up to $\theta = 55°$, and then abruptly decreases to near zero at greater longitudes, independent of frequency. To explain this discontinuous variation of polarization with longitude, we suggest that the effective harmonic may become the same for both modes at $\theta \geq 70°$, in which

case the polarization will vanish, independent of frequency. We discuss this point further in Section 4.2.

4. Discussion

4.1. PHYSICAL PARAMETERS INFERRED FROM AUGUST 9 SPECTRUM

The spectral change on August 9 relative to the previous days, associated with the occultation by the solar limb, allows us to determine several parameters for this coronal active region. We refer to the geometry shown in Figure 5 to estimate the height of the gyroresonance layer that is occulted at the longitudinal position of the spot on August 9. If we consider the contribution of the opaque chromosphere to the overall occultation as well as the photospheric limb, the source height is given by

$$h = (\mathrm{R}_\odot + \mathrm{H})/\cos 5^\circ - \mathrm{R}_\odot \simeq 5200\mathrm{km},$$

where $\mathrm{R}_\odot = 6.96 \times 10^5$ km is the radius of the sun and H is the height of the top of the chromosphere which we take as ~2500 km. This result confirms the idea that the gyroresonance layer should be located in the low corona (e.g., Zlotnik, 1968ab).

There is still a gyroresonance feature with a limiting frequency at 7.2 ± 0.2 GHz where the error range is due to the frequency interval of our receiver. Interpreting the limiting frequency as the third harmonic of the gyrofrequency, we find a field strength $860(1 \pm 0.03)$ G at the occulted height ~ 5200 km. In paper I, we have shown that the magnetic field strength is about 1420 G at the base of the corona of this spot ($\simeq$ 2500km). From these two results, we may find the vertical scale height of the coronal magnetic fields as

$$z_B \equiv \left|\frac{\partial \ln B}{\partial z}\right|^{-1} \approx \frac{\langle B \rangle}{\Delta B}\Delta z \approx 7.5'',$$

where $\langle\rangle$ and Δ denote, respectively, the mean and the difference of the associated quantities at the two heights. Note that this result for the vertical field gradient is insensitive to the choice of the height of the coronal base, H as long as $H/\mathrm{R}_\odot << 1$. Krüger *et al.* (1986) investigated the scale height of spot magnetic fields as a function of spot radius based on fitting the dipole models to their observation. For the radius of this spot ($\simeq 17''$ from Paper I), their Figure 3 gives $z_B \simeq 7.7''$, which is in agreement with the present result.

Finally, the free-free emission feature above 7 GHz can be used to determine the electron density. According to Dulk (1985), the free-free optical depth in an isothermal corona is related to the electron density as

$$\tau_{ff} \simeq 0.21 T_e^{-3/2} \nu^{-2} \int n_e^2 dl,$$

where n_e is the electron density; T_e is the electron temperature; ν is the observing frequency. The electron temperature can be read from the optically thick portion of the spectrum: $T_e \simeq 1.3 \times 10^6$K. The drop of the brightness temperature from this value by $1/e$ is found at $\nu \simeq 4.0$ GHz if we use the extrapolated portion of the ν^{-2} relation (dotted line in Figure 2). For the thickness of the active region, we may use the characteristic scale of the field distribution as found in Paper I, i.e., $\int dl \simeq 22''$. Making use of these parameters in the above equation, we derive $n_e \simeq 8.4 \times 10^9$ cm^{-3} for the coronal electron density above this active region, again for a height $h \simeq 5200$km.

4.2. VARIATION OF CIRCULAR POLARIZATION

The variation of the degree of polarization with longitude was our initial interest, since it is the very quantity characterizing the property of gyromagnetic radiation. The circular polarization presented in Figure 4 refers to the relative difference between T_L and T_R which are measured by antennae sensitive only to left- and right-circularly polarized waves, respectively. It is now useful to consider the polarization

of the two electromagnetic modes, in terms of which the theoretical gyroresonance opacities are given. In Paper I, we treated the brightness temperature of extraordinary mode T_x as being identical to T_L and that of ordinary mode T_o to T_R for this spot in negative magnetic polarity. This was possible because for a spot located near disk center the two electromagnetic modes are essentially circularly polarized. In a more general case of elliptical polarization, they are not identical, but can still be related by (Papagiannis and Kogut, 1975)

$$R_c \equiv \frac{T_L - T_R}{T_L + T_R} = D\frac{T_x - T_o}{T_x + T_o}, \tag{1}$$

where $D = 2R_o/(1 + R_o^2)$ is a correction factor for the elliptic polarization and R_o is the axial ratio of the polarization ellipse for o-mode (T_o in the nomenclature of Melrose, 1980; and Dulk, 1985). According to this expression, there are two ways in which the measured circular polarization can disappear: either $D = 0$ or $T_x = T_o$. If $D = 0$, as in the case of linear polarization, we will detect no circular polarization even though $T_x \neq T_o$. Papagiannis and Kogut (1975) show that D can drop to zero at angles near $\theta \approx 90°$. Therefore, we would not expect to see any circular polarization in the spectrum on August 9, when the region is on the limb. During August 2-7, however, the longitude is in the range, $0° \leq \theta \leq 70°$, for which Papagiannis and Kogut (1975) show $0.8 \leq D \leq 1.0$. Therefore, the concept of circular polarization would be effective in the gyroresonance spectra obtained during these days, in which case $T_L(\nu) = T_R(\nu)$ on August 7 should be interpreted as $T_x(\nu) = T_o(\nu)$.

It is commonly cited that the gyroresonance spectrum should exhibit a large degree of polarization at the optically thin frequency regime. This idea is based on the fact that the opacities for ordinary and extraordinary modes have different angular dependencies leading to effective harmonics which often differ by unity (see Zheleznyakov, 1970). However, we note that the relative ratio of these opacities changes rapidly with the viewing angle and is greatly reduced to unity above a

certain angle. A consequence of this behavior is that the effective harmonic for the ordinary mode could jump to the same value for the extraordinary mode at sufficiently large longitude, giving a discontinuous change in polarization. It seems appropriate to consider this possibility, since, as shown in Figure 3, the limiting frequencies for both modes become the same at $\theta \sim 70°$ in a way that ν_l for ordinary mode increased to the same value of ν_l for extraordinary mode. Since ν_l is strictly proportional to the product of the harmonic and the magnetic field strength at the harmonic layer, there seems to be no way to account for this abrupt increase in ν_l for o-mode except to assume a common harmonic for emission of both modes.

To further investigate this point, we calculated the distribution of effective harmonics of ordinary and extraordinary modes over a model of the active region using the MCMEM code developed by Hurford, Gary, and Garrett (1985). For the thermal structure of sunspot, we use the model atmosphere tabulated by Papagiannis and Kogut (1975). The variation of electron density is also scaled from their model, but with an enhancement factor of 10 to match the one-point coronal density value found in the present study (see Section 4.1). In the calculation, we first set up a three-dimensional lattice of the spot atmosphere at the desired heliocentric position and then integrate the contribution to the opacity at each lattice point lying along the line-of-sight. After line-of-sight integration of the gyroresonant absorption coefficient, we determine up to which harmonic the sunspot atmosphere is opaque to the radiation. The results are shown in Figure 6, where only the southern side of the spot is displayed owing to the symmetry along the north-south direction. While the emission for the extraordinary mode is dominated mostly by the third harmonic at all longitudes, the effective harmonic for the ordinary mode undergoes a change from the second at small longitudes to the third at high longitude. Therefore, this result fully supports the above idea that the sunspot microwave emission may come from a common harmonic for both modes at large longitude. The presence of the correction factor D in (1) acts only to reduce the measured circular polarization further.

Although many authors note that the lowered degree of polarization is expected at large viewing angles as the opacity difference greatly reduced at mostly transverse fields (e.g., Kakinuma and Swarup, 1962; Zlotnik, 1968ab; Zheleznyakov, 1970), they do not explicitly mention the change of the harmonic for ordinary mode.

4.3. ABSENCE OF THE POLARIZATION REVERSAL

Several authors have shown evidence of polarization reversals due to weak mode coupling in high-resolution observations of active regions seen near the solar limb (e.g., Kundu and Alissandrakis, 1984; White, Thejappa, and Kundu, 1992). We expected to see this effect in our observations, but could find no evidence for this phenomenon. The absence of the polarization reversal in our data can be accounted for in two ways. First, the polarization reversal could exist, but not be apparent in our data. In examples discussed by White, Thejappa, and Kundu (1992), the degree of polarization of the reversed portion is only 26%, and is limited to one part of the whole region. Such a subtle change may not be detected by our observation due to lack of spatial resolution combined with our absolute sensitivity to polarization no better than 10% - 15%.

Second, the polarization reversal might not occur for this region which is composed of a single unipolar sunspot. The examples of polarization reversal reported so far often involve bipolar or more complex active regions (e.g., Kundu and Alissandrakis, 1984; White, Thejappa, and Kundu, 1992). In the bipolar structure, a neutral region with moderate field strength is likely to occur somewhere along the line of sight from the bipolar structure and thus provides the polarized waves coming from limbward component with a favorable condition for mode coupling. A unipolar region, however, is less likely to have a suitable quasitransverse region and thus the inversion of polarization would not occur.

5. Summary

In this paper, we presented the center-to-limb variation of the observed spatial profile and the spectrum of microwave radiation from a spot in NOAA 4741, and discussed them in comparison with proposed models. The main results of the present paper are as follows.

First, the central depression which is commonly observed at small longitude is found to disappear at large longitude, which is explicable in terms of the angle-dependent property of the gyroresonance opacity together with presumed magnetic structure of sunspot. However, the hypothesis of the cool material origin still seems possible, if the spatial size of the cool material is just below the width of our beam.

Second, the change of the spectral shape from gyroresonance to free-free emission at the limb indicates that both are relevant radiation mechanisms at the active region corona, but the former source is confined to lower coronal height. We made use of the heliocentric position of the spot to determine the height of the gyroresonance layer as $h \simeq 5200$ km and the free-free opacity to determine the electron density as $n_e \simeq 8.4 \times 10^9 \mathrm{cm}^{-3}$ above the layer. We also found that the coronal fields along the sunspot symmetry axis varies in the range 860 G $< B <$ 1420 G over the height, 2500 km $< z <$ 5200 km. From this result, the vertical scale height was derived as $z_B \simeq 7.5''$.

Third, the discontinuous variation of the polarization spectrum with longitude is a new result that has not been noted before. We suggest that the change of effective o-mode harmonic at a large longitude may yield the most likely interpretation of this phenomenon. We find no evidence for a reversal of polarization as the region nears the limb, which may be due to a peculiarity of the source geometry.

Finally, it is observed that the brightness temperature at high, optically thin frequencies ($>$ 6 GHz) increased with longitudes. Following Zlotnik (1968b), we

attribute this to a geometrical effect of the magnetic field near the spot center rather than temporal evolution of the magnetic fields.

Acknowledgement

We thank Harold Zirin for helpful comments. This work was funded by NSF grants ATM-9013173 and AST-8919770 and by NASA grant NAGW-3005 to the California Institute of Technology.

REFERENCES

Alissandrakis, C. E., Kundu, M. R., and Lantos, P.: 1980 *Astron. Astrophys.* **82**, 30.

Alissandrakis, C. E. and Kundu, M. R.: 1982 *Astrophys. J.* **253**, L49.

Chiuderi-Drago, F., Alissandrakis, C., and Hagyard, M.: 1987, *Solar Phys.,* **112**, 89.

Dulk, G. A.: 1985, *Ann. Rev. Astr. Ap.* **23**, 169.

Hurford, G. J., Gary, D. E., and Garrett, H. B.: 1985, in R.M. Hjellming and D.M. Gibson, (eds.), *Radio Stars*, (Dordrecht:Reidel), p. 379.

Hurford, G. J. and Gary, D. E.: 1986, *Coronal Processes and Plasmas*, NASA Conference Proc. 2442, p. 319.

Kakinuma, T. and Swarup , G.: 1962, *Astrophys. J.* **277**, 865.

Krüger, A., Hildebrandt, J., Bogod, V. M., Korzhavin, A. N., Akhmedov, Sh. B., and Gelfreikh, G. B.: 1986, *Solar Phys.* **105**, 111.

Kundu, M. R., Alissandrakis, C. E., Bregman, J. D., and Hin, A. C.: 1977, *Astrophys. J.* **213**, 278.

Kundu, M. R. and Alissandrakis, C.E.: 1984, *Solar Phys.* **94**, 249.

Lang, K. R. and Wilson, R. F.: 1982, *Astrophys. J. Letters,* **255**, L111.

Lantos, P.: 1968, *Ann Astrophys.* **31**, 105.

Lee, J. W., Hurford, G. J., and Gary, D. E.: 1993, *Solar Phys.* **144**, 45 (Paper I).

Melrose, D. B.: 1980, *Plasma Astrophysics*, Gordon and Breach, New York.

Papagiannis, M. D. and Kogut, J. A.: 1975, AFRCL-TR-75-0430.

Strong, K. T., Alissandrakis, C. E., and Kundu, M. R.: 1984, *Astrophys. J.* **277**, 865.

White, S. M., Thejappa, G., and Kundu, M. R.: 1992, *Solar Phys.* **138**, 163.

Zheleznyakov, V. V.: 1962, *Soviet Astron.* **6**, 3.

Zheleznyakov, V. V.: 1970, *Radio Emission of the Sun and Planets*, Pergamon Press, New York.

Zlotnik, E. Ya.: 1968a, *Soviet Astron.* **12**, 245.

Zlotnik, E. Ya.: 1968b, *Soviet Astron.* **12**, 464.

Table I

Heliolongitudes and the Photospheric Field Strengths of the Sunspot in NOAA 4741

Date	1986 Aug. 2	4	5	6	7	9
Heliolongitude	1.8°W	28°W	42°W	55°W	68°W	95°W
Magnetic Field	2400 G	2400 G	2200 G	2300 G	2200 G	–

Figure Captions

Fig. 1. Spatial profiles of the brightness temperature as a function of longitudes. Curves at each raw represent a day's profile at five frequencies. Thick and thin solid lines represent the brightness temperatures of right- and left-circularly polarized waves, respectively. Temperatures at all frequencies are normalized to the maximum value on each day. Beam sizes are also shown in the upper corner.

Fig. 2. Spectra of brightness temperature at six heliolongitudes. Circles and crosses represent brightness temperatures of right- and left- circularly polarized waves, respectively.

Fig. 3. Limiting frequencies in two modes and their ratio as a function of longitude.

Fig. 4. Degree of circular polarization as a function of frequency.

Fig. 5. Geometry of the occultation of the gyroresonance layer.

Fig. 6. Two-dimensional display of the effective harmonic distribution at $\nu = 5.0$ GHz over the projected plane over the sky at three different longitudes. Owing to symmetry, only the southern half of the whole distribution is shown. Extraordinary mode is shown at left side and ordinary mode at right side.

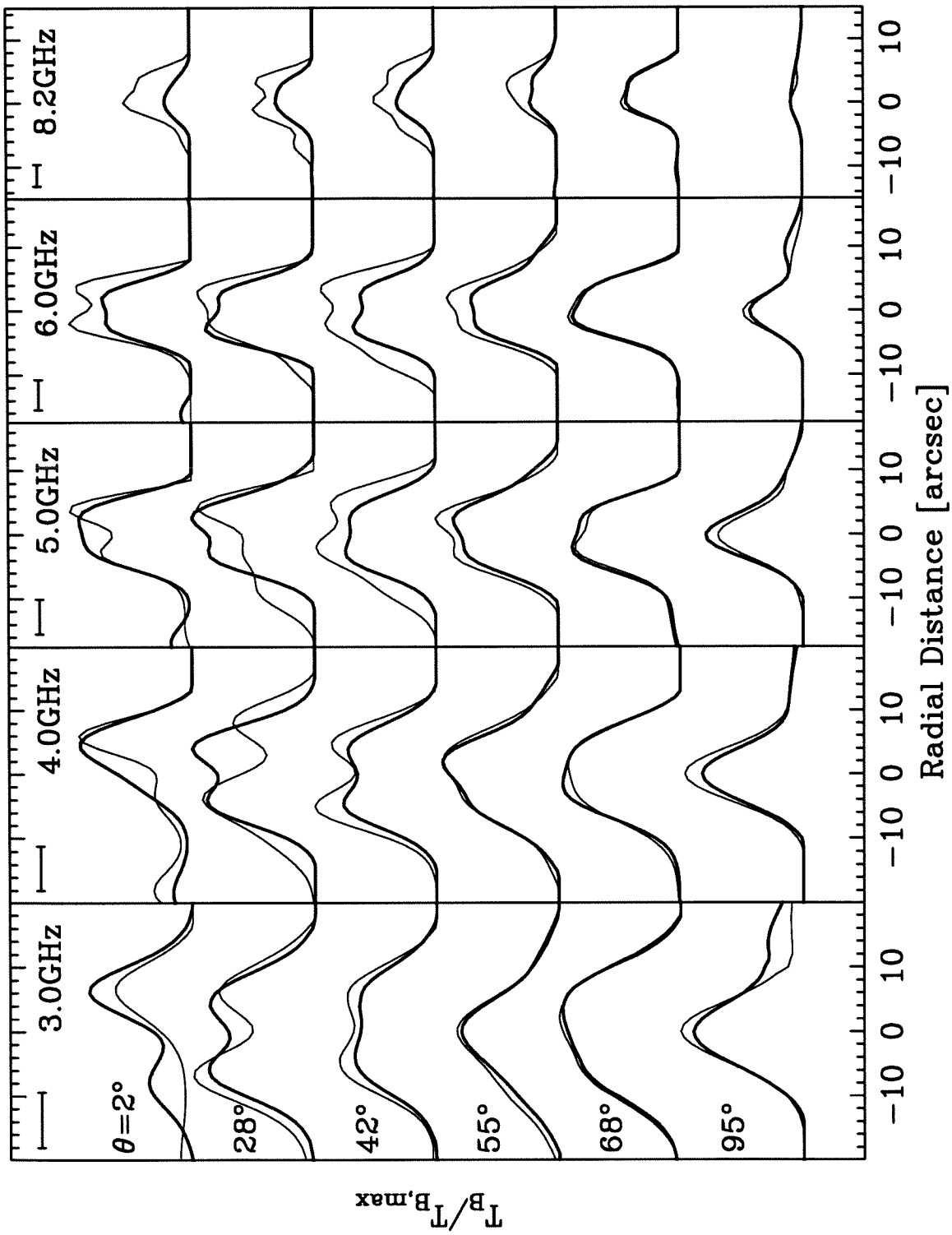
3.0GHz
4.0GHz
5.0GHz
6.0GHz
8.2GHz
θ=2°
28°
42°
55°
68°
95°
−10 0 10
Radial Distance [arcsec]
T_B/T_B,max

Figure 1

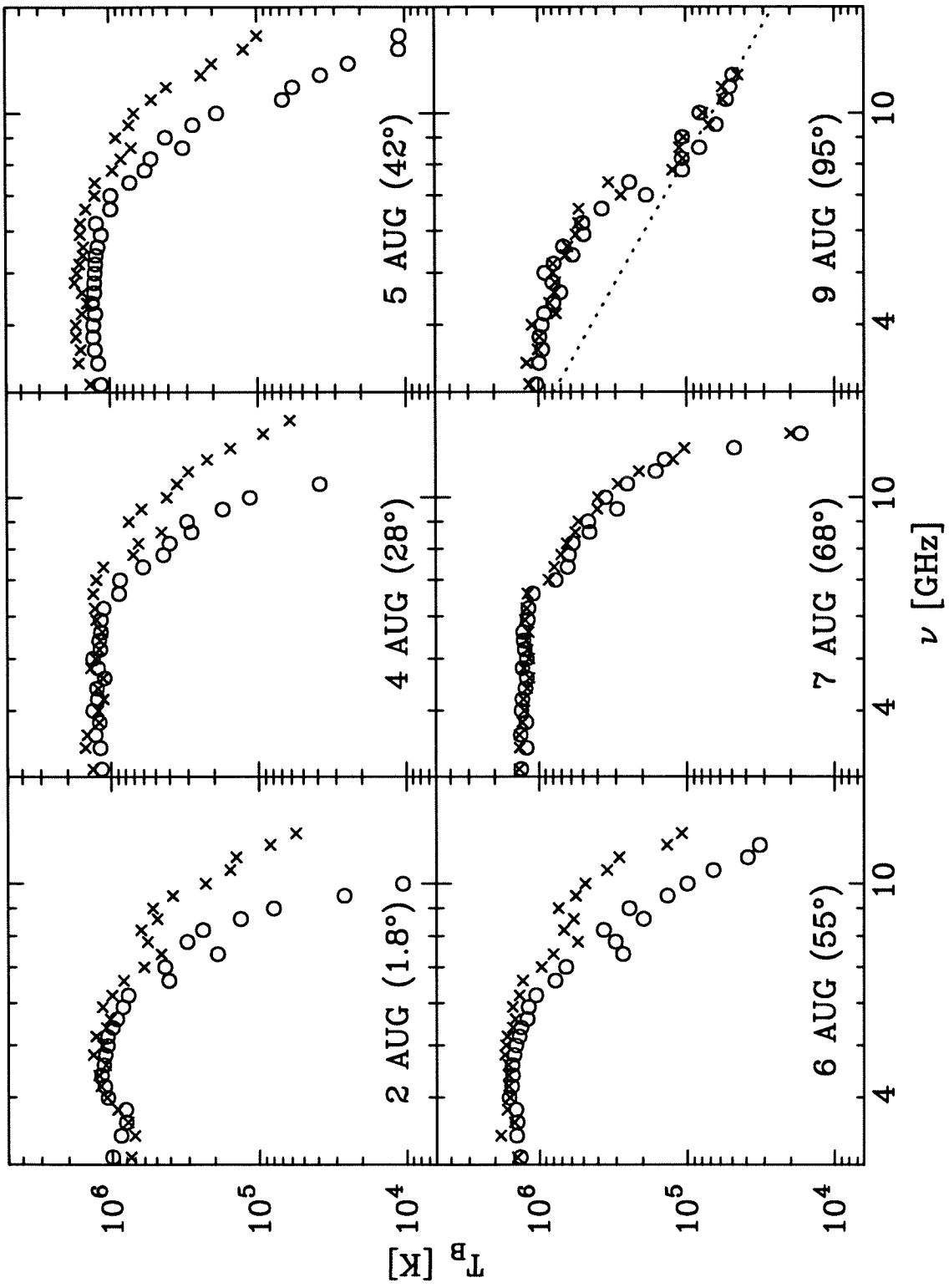

Figure 2

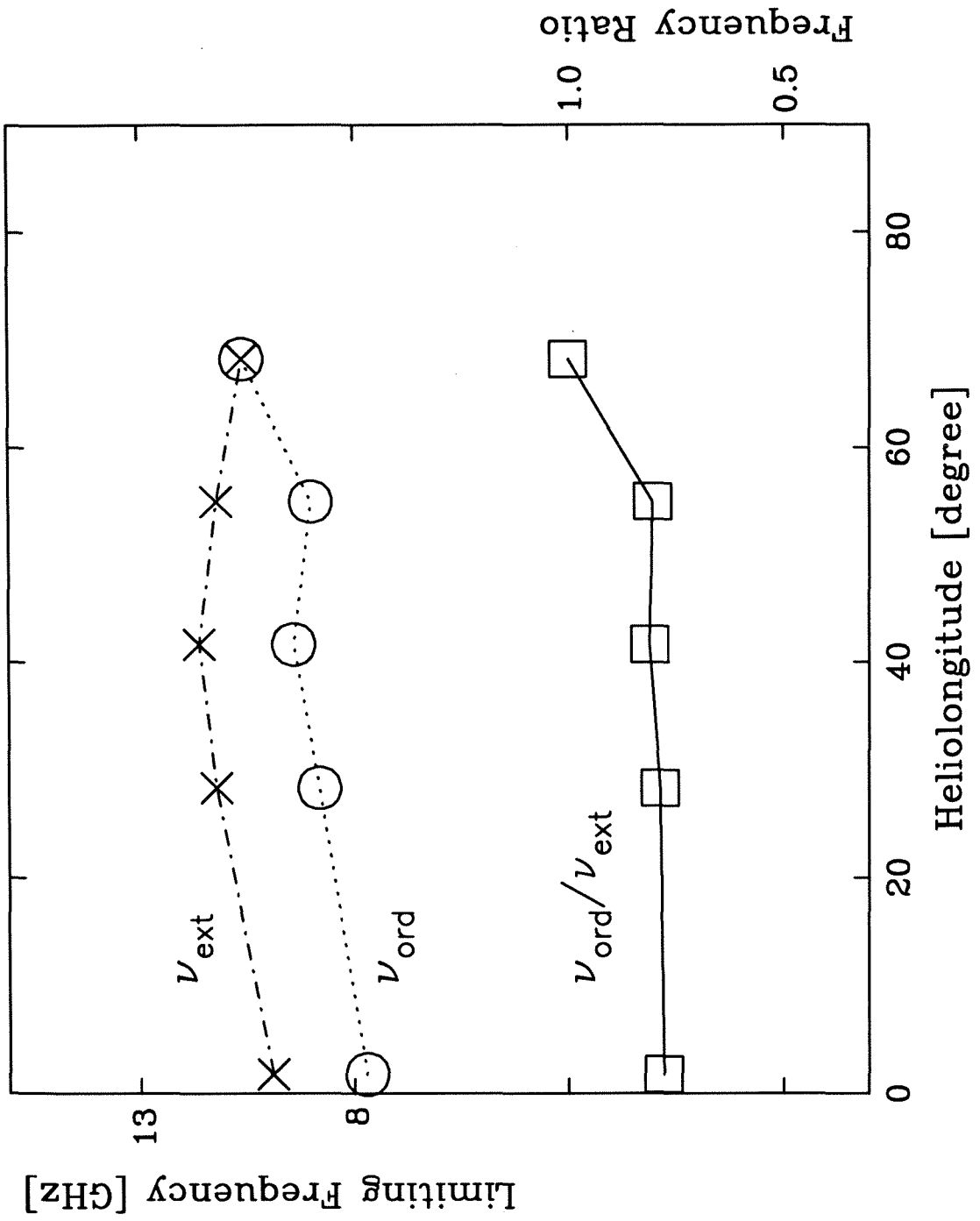
Frequency Ratio
1.0
0.5
Limiting Frequency [GHz]
13
8
0
20
40
60
80
Heliolongitude [degree]
ν_{ext}
ν_{ord}
ν_{ord}/ν_{ext}

Figure 3

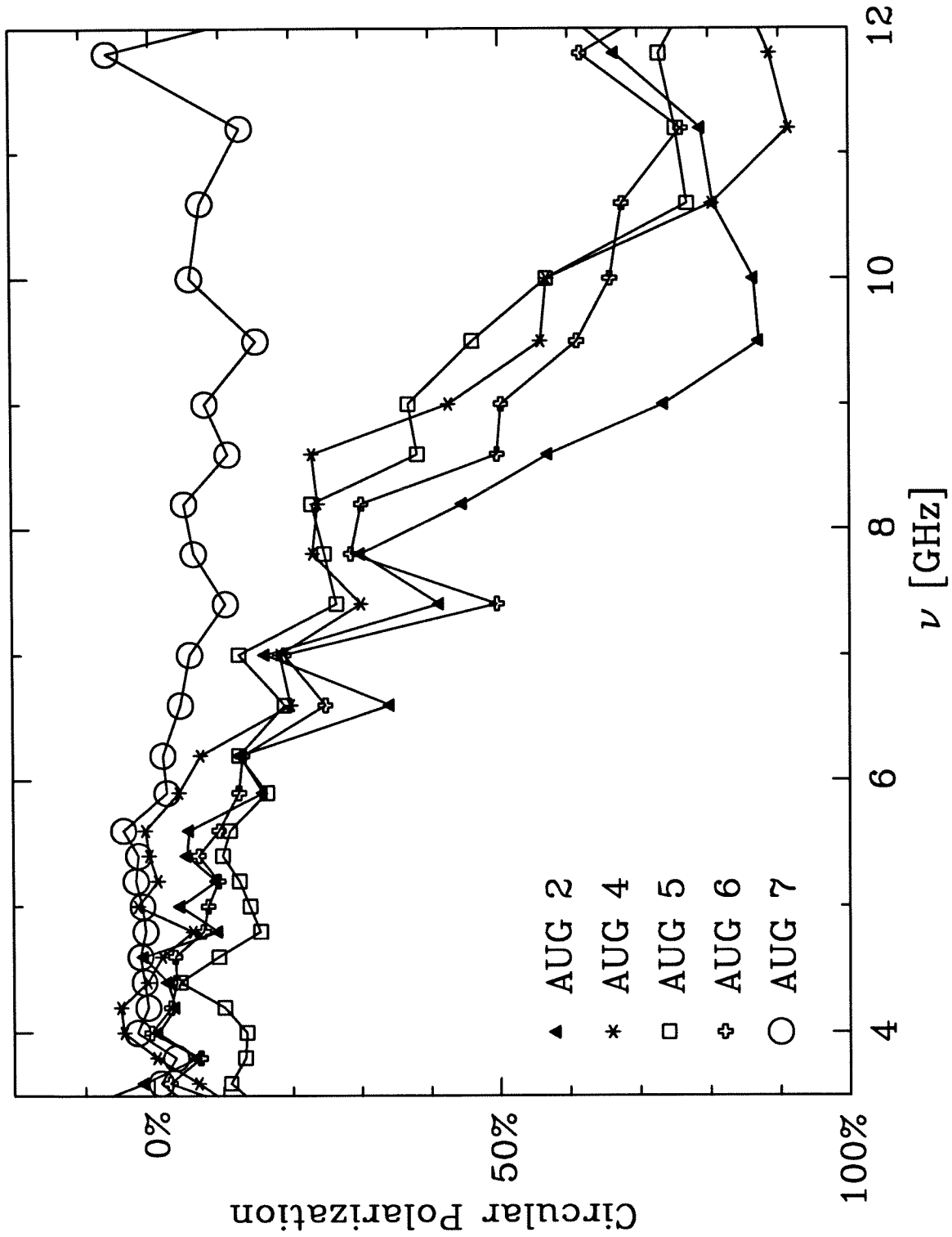
Circular Polarization
0%
50%
100%
4
6
8
10
12
ν [GHz]
AUG 2
AUG 4
AUG 5
AUG 6
AUG 7

Figure 4

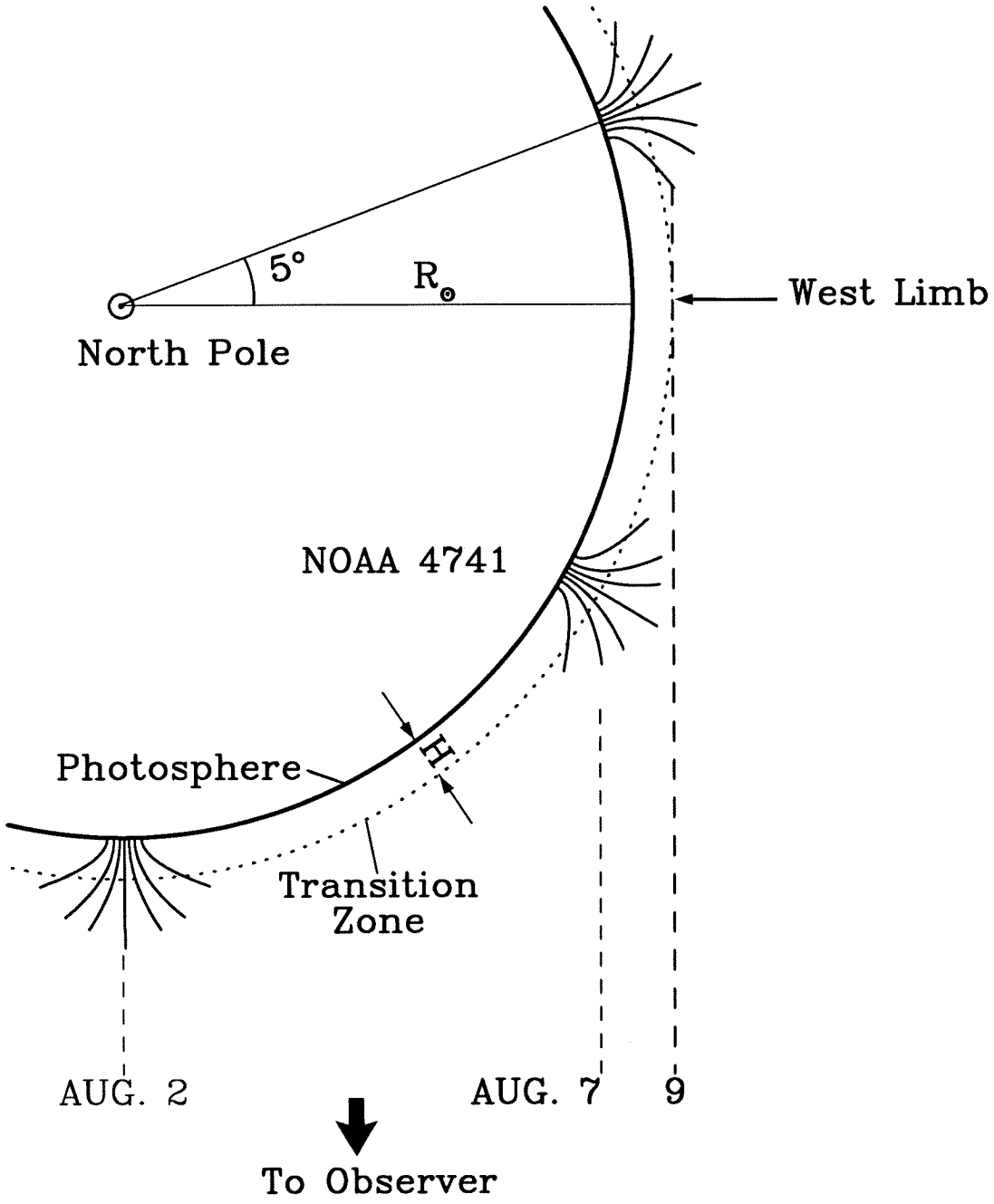
5°
$R_\odot$
West Limb
North Pole
NOAA 4741
Photosphere
H
Transition
Zone
AUG. 2
AUG. 7
9
To Observer

Figure 5

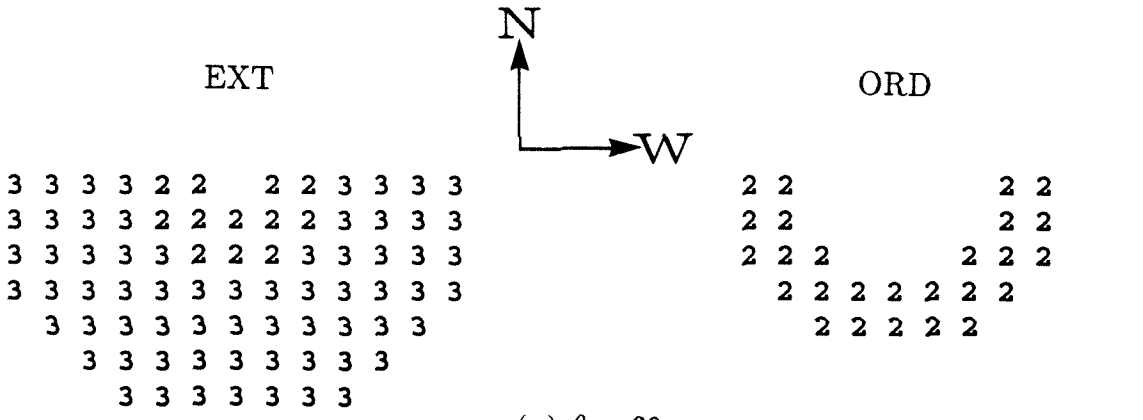

(a) $\theta = 0°$

(b) $\theta = 30°$

(c) $\theta = 70°$

Figure 6

Chapter 4

Force balance in the sunspot corona

Published in the **IAU Colloquium**, No. 141

Abstract

We present our earlier measurement of the coronal fields above a sunspot in the active region, NOAA 4741, which was obtained using microwave spectroscopy from the Owens Valley Radio Observatory (OVRO) in a form that allows comparison with theoretical models. Our empirical results for the coronal fields are compared with several theoretical models in order to understand the magnetic structure of a static sunspot. It is found that the presence of transverse pressure gradients should be considered to get a satisfactory fit.

1. Introduction

The magnetic field structure of the active region corona has been a popular subject in microwave studies of solar active regions, as the solar microwave radiation is known to provide a unique opportunity to detect the coronal fields directly (e.g., Alissandrakis, Kundu, and Lantos, 1980). One technique to measure the coronal fields using microwave spectroscopy has been discussed by Hurford and Gary (1986). In Papers I and II (Lee, Hurford, and Gary (1993) and Lee, Gary, and Hurford (1993), respectively), we applied Hurford and Gary's (1986) procedure to derive the coronal field distribution in the active region NOAA 4741 along both the vertical and the horizontal directions. This was possible because we had multi-frequency, interferometric observations at OVRO at both the disk center and the limb. Since these results are new and entirely empirical, it is of new interest to test whether the coronal field distribution inferred from our observations can be reproduced by any simple theoretical model. In this paper, we make a comparison of our observational results with the dipole model, the solenoid model of Sakurai and Uchida (1977), and the magnetohydrostatic equilibrium model of Low (1980) to yield an implication for the static magnetic structure of a sunspot. The results of our coronal field measurement are briefly described in §2; the photospheric field measurement from magnetogram data is also included. Comparison of the observational data with theoretical models is made in §3. In §4, we discuss the result in relation to the force balance in a sunspot atmosphere. The conclusion will be given in §5.

2. Observed Magnetic Fields

In Paper I, we report the radial distribution of magnetic fields at the coronal base deduced from OVRO microwave data of the spot located near the disk center. In Paper II, the vertical variation of the coronal fields at the center of the same spot is inferred from the occultation by the solar limb seven days later which allows a measurement of the field at another point higher in the corona. Here, we bring these two results together to yield a three-dimensional magnetic structure of the spot in

a form in which they can be compared with theoretical models. For this purpose, we use the cylindrical coordinates shown in Figure 1 where $\hat{\mathbf{z}}$ is along the symmetry axis of the spot and $z = 0$ is at the waist of the spot field; d and H are respectively the depth of the waist of the sunspot fields and the height of the coronal base above the photosphere; h is the height of the point of occultation observation above the coronal base. In these coordinates, our results from Papers I and II for the coronal magnetic fields are expressed as

$$B(r, z = d + H) = 1420(1 \pm 0.08) \exp\left[- \left(\frac{r}{11.05'' \pm 0.16''} \right)^2 \right] \text{ G}, \qquad (1)$$

and

$$B(r = 0, z = d + H + h) = 860(1 \pm 0.03) \text{ G} \quad \text{with} \quad h \simeq 2700\text{km}. \qquad (2)$$

We complement the above results for the coronal fields by using the photospheric magnetic fields inferred from the KPNO magnetogram data and the Mt. Wilson data (courtesy of Tom Shieber) to impose stronger constraints on the model fitting. At the photospheric level (Paper I),

$$B_z(r, z = d) = 2400(1 \pm 0.04) \exp\left[- \left(\frac{r}{9.9'' \pm 1.0''} \right)^2 \right] \text{ G}. \qquad (3)$$

Note that the photospheric field given by (3) is the vertical component only, while the coronal fields, B, that appear in (1) and (2) refer to the total field strengths.

3. Comparison with Theoretical Models

We compare our observational results with three theoretical models: (i) a simple dipole model (e.g., Purcell, 1981), (ii) the solenoid model of Sakurai and Uchida (1977), (iii) Low's (1980) magnetostatic equilibrium model (hereafter called 'M.S.E.'

model) which is based on the similarity law of Schlüter-Temesváry (1958). All of these models present the cylindrically symmetric fields with no ϕ-component. We do not consider force-free models (e.g., Nakagawa *et al.*, 1971) in spite of their popular use, since this spot does not appear in a spiral structure as usually predicted by the force-free models.

To constrain model parameters, we first compare the model values for agreement with the observed magnetic fields at the spot center at three different heights, i.e., $B_z(0,d)$, $B(0,d+H)$, and $B(0,d+H+h)$ as given above. This determines the allowable range of the depth, d, of the waist of the field (or the location of current coils) of each model for a given horizontal extent scale, a. We then look for a and H that can reproduce the observed radial distribution of the fields, $B_z(r,d)$ and $B(r,d+H)$, as closely as possible. We plot in Figure 2 the resulting model values (solid lines) together with our results (shaded area).

For the dipole model, only two parameters need to be specified: the magnetic moment, m, and its location, d. Therefore, there can be no doubt that the dipole model predicts a more extended field structure at the upper sunspot atmosphere than observed. In the solenoid model, a current coil giving rise to the magnetic moment is allowed to have a finite horizontal extent, a, by which we can adjust the field shape outside the coil at a given depth. However, due to the constraint of vertical magnetic fields at three different heights, the choice of a is much limited. The result is that the solenoid model is also not capable of reproducing the confined structure of the coronal fields we observe. The M.S.E. model comes closer to our observation: First of all, it predicts a gaussian form for the field distribution in agreement with our observation (Equations [1] and [3]). The horizontal structure of this model is sensitive to the parameter, η (see Low (1980) for full expressions), but insensitive to the choice of H. This is in good agreement with our result that the gaussian width changes only a little with height, H. The vertical variation is also closely fitted by this model if we locate the waist ($z=0$) at a depth, $d \simeq 10''$.

4. Implication for the Force Balance in a Sunspot

The dipole and the solenoid fields are specified solely by source currents in vacuum. In comparison, the M.S.E. model (Low, 1980) is based on the exact solution of the magnetohydrostatic equation, which reads

$$\frac{1}{4\pi}(\nabla \times \mathbf{B}) \times \mathbf{B} - \nabla P - \rho g \hat{z} = 0, \tag{4}$$

where P is the gas pressure, ρ the density, and g the gravitational acceleration. Therefore, the agreement of our observational results to the M.S.E. model would imply that the static interaction between the magnetic curvature force, the pressure gradient, and the gravity serves to shape the sunspot magnetic structure.

The amount of horizontal pressure gradient can be estimated from the assumed magnetic field structure as

$$\frac{\partial P}{\partial r} = \frac{1}{4\pi} B_z \Big(\frac{\partial B_r}{\partial z} - \frac{\partial B_z}{\partial r} \Big). \tag{5}$$

We compute the pressure gradient, $\partial P/\partial r$, and the corresponding pressure difference, $\Delta P(r) = P(r = \infty) - P(r) = \int_r^\infty (\partial P/\partial r) dr$, by using Low's (1980) model for the magnetic fields together with the parameters found above (Figure 2). The results are shown in Figure 3. The pressure difference at the photosphere ($z = d$) is estimated to $\Delta P(r = 0) \simeq 1.7 \times 10^5$ dyne cm^{-2}, which is rather smaller than a more popularly adopted value ($\sim 10^6$ dyne cm^{-2}) in previous theoretical works on the sunspot structure (e.g., Deinzer, 1965; Yun, 1970). On the other hand, the value at the coronal base ($z = d + H$) comes out as $\Delta P(r = 0) \simeq 0.6 \times 10^5$ dyne cm^{-2}. It is therefore noted that about one third of the horizontal pressure difference at the photosphere should be maintained at the base of the corona in order to make a confined magnetic structure as found in our observations.

The pressure gradient along the vertical direction cannot be assessed without knowledge of the density variation. Along the sunspot axis, however, the magnetic curvature vanishes and thus there are only the vertical pressure gradient and the gravity to be balanced. This explains why even a vacuum model can match the observed vertical field distribution along the sunspot axis. It should be noted that the above consideration on the force balance is valid from the photosphere up to the coronal base above which the magnetic field lines could be force-free.

5. Conclusion

In this paper we investigated whether our observational results (Papers I and II) for the sunspot (NOAA 4741) coronal fields can be reproduced by any simple theoretical model. It is found that our results can be closely fitted by the M.S.E. model (Low, 1980) where static interaction between the magnetic curvature force and the horizontal pressure gradient serves to limit the spread of the field lines with height. We therefore presume that the sunspot fields at upper atmosphere tends to be kept confined by the pressure gradient across the spot which would otherwise be extended as predicted by the dipole or the solenoid model.

Acknowledgement

We thank Dr. B. C. Low for helpful comments. This work was funded by NSF grants ATM-9013173 and AST-8919770 and by NASA grant NAGW-3005 to the California Institute of Technology.

References

Alissandrakis, C. E., Kundu, M. R., and Lantos, P.: 1980, *Astron. and Astrophys.* **82**, 30.

Deinzer, M.: 1965, *Astrophys. J.* **141**, 548.

Hurford, G. J. and Gary, D. E.: 1986, in *Coronal Processes and Plasmas*, Nasa Conference Proc. 2442, p. 319.

Lee, J. W., Hurford, G. J., and Gary, D. E.: 1993, *Solar Phys.* **144**, 45 (Paper I).

Lee, J. W., Gary, D. E., and Hurford, G. J.: 1993, *Solar Phys.* **144**, 349 (Paper II).

Low, B. C.: 1980, *Solar Phys.* **67**, 57.

Nakagawa, Y., Raadu, M. A., Billings, D. E., and McNamara, D.: 1971, *Solar Phys.* **19**, 72.

Purcell, E. M.: 1981, *Electricity and Magnetism*, McGraw-Hill, New York.

Sakurai, K. and Uchida, Y.: 1977, *Solar Phys.* **52**, 397.

Schlüter, A. and Temesváry, S.: 1958, in B. Lehnert, (eds.), *Electromagnetic Phenomena in Cosmical Physics*, *IAU Symp.* **6**, 263.

Yun, H. S.: 1970, *Astrophys. J.* **162**, 975.

Figure Captions

Fig. 1. The sunspot coordinates and the three levels where magnetic fields are measured (marked by a filled circle and dark panels). See text for the definitions of d, H, and h.

Fig. 2. Comparison of the fields deduced from the observation (shaded area) with theoretical fields (solid lines). Used model parameters are: $d = 15''$, $H = 3.0''$, and $m = 1.6 \times 10^{30}$ G·cm^3 for the dipole model; $d = 13''$, $H = 3.0''$, $a = 4.0''$, and $J = 1.3 \times 10^{23}$ esu·sec^{-1} for the solenoid model; $d = 10''$, $H = 3.5''$, $a = 7.0''$, $B_o = 9.4 \times 10^{20}$ G·cm^2, and $\eta = 1.95$ for the M.S.E. model.

Fig. 3. The horizontal pressure gradient $\partial P/\partial r$ (solid lines) and the pressure difference $\triangle P$ (dashed lines) at two heights ($z = d$ and $z = d + H$) as a function of the radial distance r. r_{um} and r_{penum} represent the umbral and the penumbral radii, respectively.

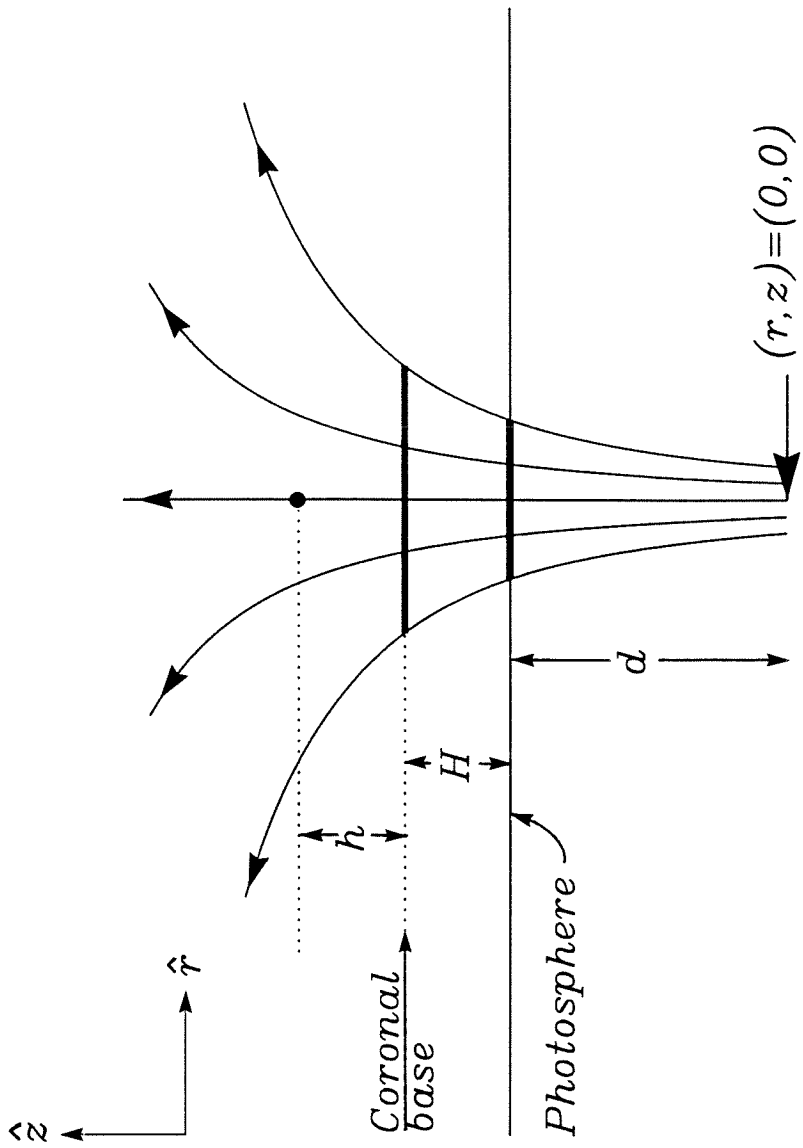

Figure 1

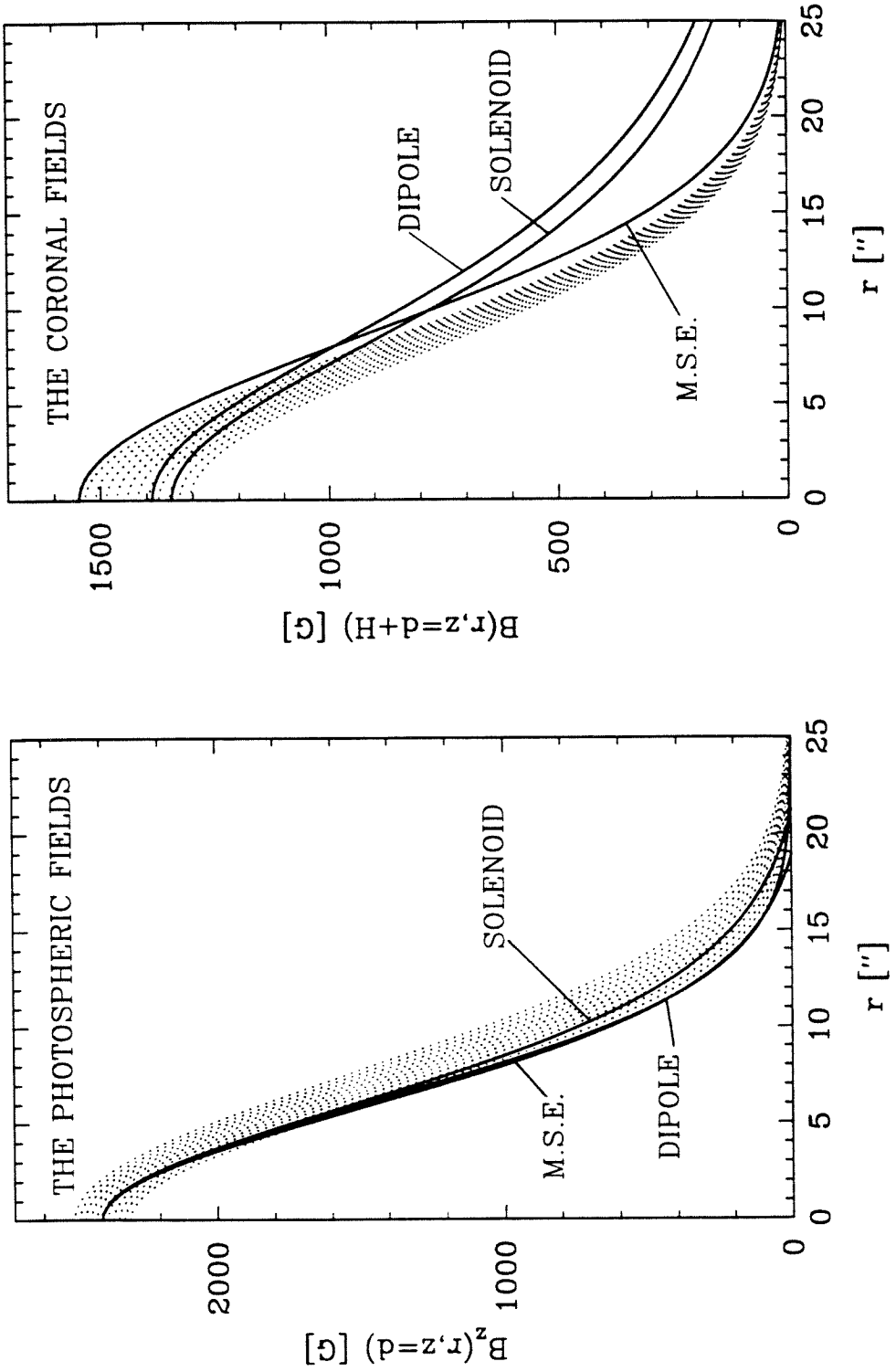
THE CORONAL FIELDS
DIPOLE
SOLENOID
M.S.E.
B(r,z=d+H) [G]
r ["]
THE PHOTOSPHERIC FIELDS
SOLENOID
M.S.E.
DIPOLE
B_z(r,z=d) [G]
r ["]

Figure 2

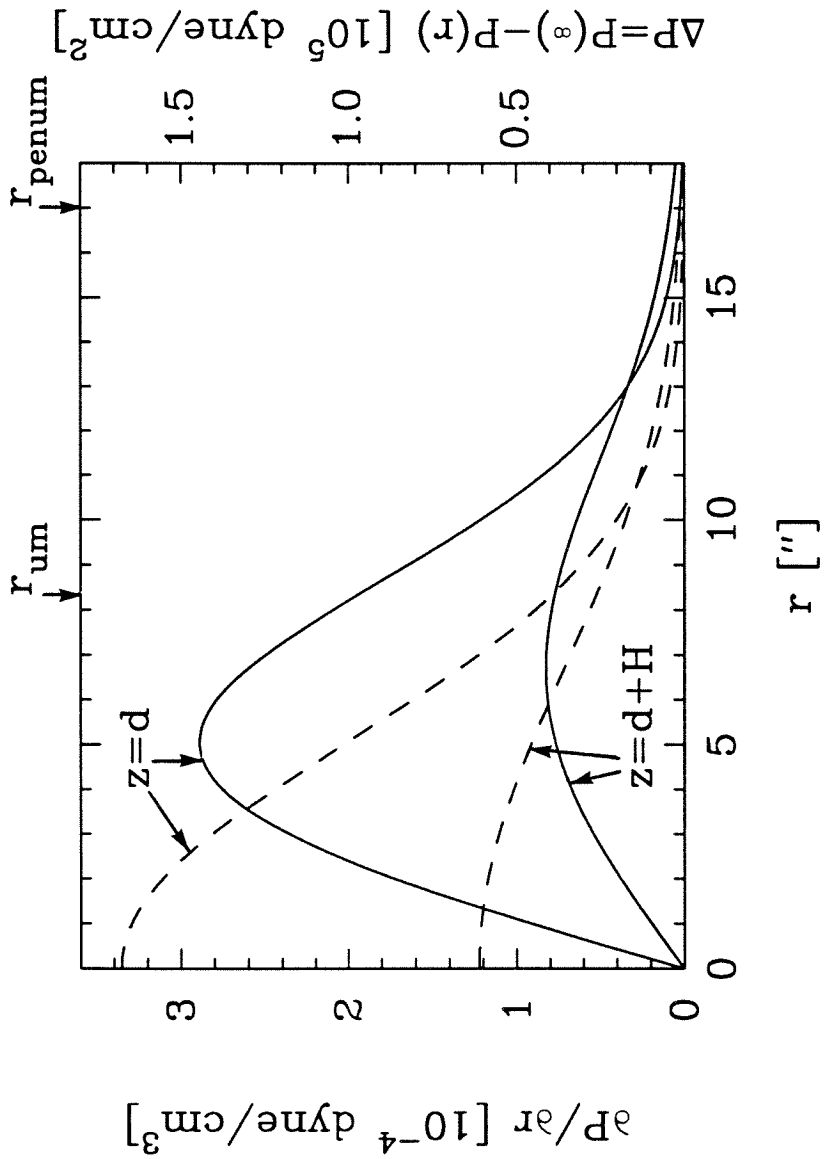
ΔP=P(∞)−P(r) [10^5 dyne/cm^2]
1.5
1.0
0.5
r_penum
r_um
z=d
z=d+H
0
5
10
15
r ["]
3
2
1
0
∂P/∂r [10^-4 dyne/cm^3]

Figure 3

Chapter 5

Evolution of electrons in impulsive microwave bursts

Submitted to the **Solar Physics**

Abstract

We analyze the time variation of microwave spectra and hard X-ray spectra of 1989 March 18, which are obtained from the Solar Array at the Owens Valley Radio Observatory (OVRO) and the Hard X-Ray Burst Spectrometer (HXRBS) on the Solar Maximum Mission (SMM) respectively. From this observation, it is noted that the hard X-ray spectra gradually soften over 50 - 200 keV on-and-after the maximum phase while the microwaves at 1-15 GHz show neither a change in spectral shape nor as rapid a decay as hard X-rays. This leads to decoupling of hard X-rays from the microwaves in the decay phase away from their good correlation seen in the initial rise phase.

To interpret this observation, we adopt a view that microwave emitting particles and hard X-ray particles are physically separated in an inhomogeneous magnetic loop but linked via interactions with the Whistler waves generated during flares. From this view point, it is argued that the observed decoupling of microwaves from hard X-rays may be due to the different ability of each source region to maintain high energy electrons in response to the Whistler waves passing through the entire loop. To demonstrate this possibility, we solve a Fokker-Planck equation that describes evolution of electrons interacting with the Whistler waves, taking into account the variation of Fokker-Planck coefficients with physical quantities of the background medium. The numerical Fokker-Planck solutions are then used to calculate microwave spectra and hard X-ray spectra for agreement with observations. Our model results are as follows: In a stronger field region, the energy loss by electron escape due to scattering by the waves is greatly enhanced resulting in steep particle distributions that reproduce the observed hard X-ray spectra. In a region with weaker fields and lower density, this loss term is reduced allowing high energy electrons to survive longer so that microwaves can be emitted there in excess of hard X-rays during the decay phase of the flare. Our results based on spectral fitting of a flare event are discussed in comparison with previous studies of microwaves and hard X-rays based on either temporal or spatial information.

1. Introduction

The temporal variations of impulsive microwave flux and hard X-ray flux during solar flares are so similar that the same or closely related populations of electrons are believed to be responsible for both radiations. The attempt to elucidate this good correlation have, however, met several controversies with a simple model where both radiations are emitted by an identical population in the same position in a loop. First, observations with high spatial resolution shows that microwaves and hard X-rays are not cospatial (see Dulk, McLean, and Nelson, 1985 for review). Second, more detailed comparison of time profiles uncovers that impulsive microwave bursts peak slightly later (Kaufmann *et al.*, 1983; Cornell *et al.*, 1984) and fall more slowly than the accompanying hard X-ray bursts (Crannel *et al.*, 1978; Lu and Petrosian, 1990). It therefore seems that microwaves and hard X-rays, while they may be of a common origin, do not necessarily coevolve in the same physical volume. More plausibly, it is suggested that the hard X-rays are emitted when precipitating into the foot-points of a flaring loop while the particles trapped in the coronal part of the loop emit microwaves (e.g., Dennis and Schwarz, 1989; Petrosian, 1989; Lu and Petrosian, 1990).

If the microwave and the hard X-ray emitting particles are separated in position and if physical quantities affecting the energy gain and loss vary with position within a flaring loop, each population may well undergo different evolution. The results will be reflected in the resulting microwaves and hard X-rays in terms of spectral variation as well as in terms of time profiles or spatial images. It is, in fact, the spectral data that carry more direct information of the electron energy distribution.

Numerous works to deduce solar flare particles have been made primarily referring to hard X-ray spectra. One reason is that high-resolution hard X-ray spectra have been available for a long time (e.g., Lin and Schwarz, 1987) and the optically-thin hard X-ray spectra can, with some assumptions, be inverted to give the particle distribution (e.g., Brown, 1971; Johns and Lin, 1992; Hamilton and Petrosian, 1992;

Holman and Benka, 1992). In comparison, the study of electron distributions using microwave radiation has been relatively limited. A reason for this situation may come from intrinsic difficulties in analyzing microwaves such as more source parameters to be specified and the radiation transfer problem entangled with the source geometry (Brown, 1975; Lu and Petrosian, 1989; Petrosian, 1989). Thus, in the study of microwave-emitting electrons, a schematic distribution function that combines a Maxwellian and nonthermal power-law distribution has been used to calculate the microwave spectra for comparison with observations (e.g., Holt and Ramaty, 1969; Böhme *et al.*, 1976, 1977; Benka and Holman, 1992). It would be better if a more detailed electron distribution function can be modelled based on microwave spectra to deduce the evolution of microwave-emitting electrons.

In this paper, we study the microwave spectra and the hard X-ray spectra observed in the 1989 March 18 flare which are obtained from OVRO and the HXRBS on SMM, respectively. The motivation for use of these data is two-fold: First, the event was a compact limb flare with two foot points lying perpendicular to the line of sight according to Hα images obtained at Big Bear Solar Observatory (BBSO). As will be further discussed in Section 2, such a source geometry greatly alleviates the above-mentioned difficulties for analyzing microwave data. Second, this event appears as a typical one in both microwaves and hard X-rays so that the results of analysis of these data can help to address some general problems. Specifically, the microwave spectra appear in the classic shape of a single gyrosynchrotron spectrum and the spectral shape changes little during the flare (Stähli, Gary, and Hurford, 1989, 1990). The hard X-ray data shows spectral softening after the maximum flux (e.g., Dennis, 1988; Dulk, Kiplinger, and Winglee, 1992). The main observational point we newly concern ourselves with in this data set is the apparent insensitivity of microwave spectral variation relative to that of the accompanying hard X-rays during the decay phase, which basically implies a different evolutionary history for each population.

Unlike most other works, spectral information is given for both microwaves and hard X-rays. We thus investigate the microwave-emitting particles and the

hard X-ray particles separately, based on a Fokker-Planck equation, taking into account the variation of energy gain and loss efficiency along an inhomogeneous model loop. The solutions are then used to compute theoretical microwave flux and hard X-ray flux for agreement with observations. In this way, we hopefully explore the evolution of the electron distributions underlying both microwaves and hard X-rays. The plan of this paper is as follows: In Section 2, we report observational data. In Section 3, we present a set of model particle distributions after solving the Fokker-Planck equation. From these, we compute the microwave and hard X-ray flux spectra for comparison with observations in Section 4. Our approach and results will be discussed in Section 5.

2. Observation

The data we examined are Hα, microwaves and hard X-rays of the 1989 March 18 flare that occurred in the active region NOAA 5395. The Hα images obtained at BBSO reveal that the source geometry is that of a single compact loop located at the very limb facing the observer. In such a geometry, we may set the viewing angle of magnetic fields to a common value ($\sim 90^{\circ}$) over the whole source region. Moreover, the radiative transfer problem, in this case, is simplified because the source can be assumed to be uniform along the line of sight (i.e., across the magnetic fields) although the loop is stratified along the magnetic fields–this is not the case for disk flares. In addition, the fact that Hα brightness concentrated in one leg of the loop enhances the probability of single source for the hard X-rays. We also note that this event attained GOES soft X-ray class M3.1 and shows a maximum microwave flux close to 10^3 sfu and thus provides sufficient strength of radiation for spectral analysis.

In Figure 1, we compare flux spectra of microwaves with those of hard X-rays at six different times with interval of 20s including the time of maximum, t_p, which is 21:56:40 UT. The microwave spectra show a spectral maximum around 8-10 GHz and appear in a typical gyrosynchrotron shape (Guidice and Castelli, 1975).

The shape of these microwave spectra is invariant during this period, as typical of high resolution microwave burst spectra observed at OVRO (Stähli, Gary, and Hurford, 1989, 1990). In contrast, the hard X-ray spectra appear in the form of a single power-law which is gradually steepened with time; the spectral slope changed from 4.6 to 5.0 over $t_p \pm$ 20s. The steepening seems to continue after this, but an accurate spectral fit is difficult after $t_p + 30$s because the spectra become too steep. To conclude, changes in the microwave spectrum do not correlate well with those in the hard X-ray spectrum.

Figure 2 compares the time profiles of microwaves at six selected frequencies and those of hard X-rays in channel 1 to channel 5. The microwave frequencies and energy range of X-ray channels are specified in the figure. It is seen that hard X-rays have a good correlation with microwaves over a time range limited to $t \leq t_p + 20$s. Later on ($t > t_p + 20$s), however, hard X-ray photons with energy $\epsilon > 100$ keV drop more rapidly than those with $\epsilon < 100$ keV, which leads to the spectral steepening of hard X-ray spectra as noticed above (Figure 1). In contrast, the microwaves keep a similar time profile at all frequencies at least at $t < t_p + 2$ min. Therefore, microwave flux is more abundant compared to hard X-ray flux in the decay phase (cf., Crannell *et al.*, 1978; Lu and Petrosian, 1990).

In Figure 3, we show the phase and visibility data of microwaves mainly to check the source size effect on the microwave flux. The phase and visibility data are obtained from a baseline lying in the east-west direction of length 367m. The phases show a linear relationship with the frequencies, indicative of a simple structure. We are thus encouraged to use the relative visibility data to calculate the FWHM of the microwave source according to the procedure presented in Bastian and Gary (1992). The resulting FWHM is almost independent of frequency at ν = 3.0 - 8.0 GHz and keeps a similar value over the period of current investigation. This means that the slow decay of microwave flux relative to that of hard X-rays is not due to an increase of source size but entirely due to a slower decay of the brightness temperature. The result also excludes a hypothesis that the time-invariant spectral

shape might be solely due to the change of the source size under time-invariant brightness temperatures.

3. Model for Particle Evolution

A quantitative analysis of the above radiation spectra requires information of the electron evolution in momentum space. There are various theoretical models for the solar flare particles (see Heyvaerts, 1981, for review). It is, however, generally agreed that plasma waves build up during flares and provide stochastic acceleration of electrons to higher energies at which they emit microwaves and other high energy emissions (e.g., Bai and Dennis, 1985; Dulk, Kiplinger, and Winglee, 1992). We therefore consider a model in which evolution of the electron distribution function is closely related to the fate of waves through the gyroresonant interaction between them.

Of many candidates for the agent of stochastic acceleration, we consider the Whistler waves because the gyroresonant interaction with Whistler waves has been suggested to provide a viable mechanism for accelerating electrons in the energy range 1 keV to MeV which is our current concern (e.g., Melrose 1974; Miller and Ramaty, 1987, 1989; Aschwanden 1990; Steinacker and Miller 1992; Miller and Steinacker 1992; Hamilton and Petrosian, 1992). Another motivation for adopting the Whistler waves is that the efficiency of energy gain and loss of particles due to these waves depends sensitively on the magnetic field strength, unlike other candidates for stochastic process (e.g., Fermi process and Langmuir waves). This property agrees with the demands of our model, where the loop-top and the foot-point regions are distinguished mainly according to the field strength.

We, in general, follow the Fokker-Planck formalism used in previous works as mentioned above–in particular, Hamilton and Petrosian (1992). However, we introduce several simplifications which may be better justified in the time period, $t \geq t_p$, under investigation. Firstly, we ignore the injection spectrum, $S(E,t)$, in the Fokker-Planck equation. The injection must have had an influence upon the

particle evolution at the initial rise, perhaps responsible for the good correlation of microwaves with hard X-rays. However, it may be assumed that injection has been turned off by the time of maximum flux. Secondly, although significant anisotropy in the particle distribution is required to generate the Whistler waves at the very initial period, this anisotropic structure in the distribution of radiating particles has gone by the time t_p, owing to much more efficient pitch angle scattering relative to the momentum diffusion. These assumptions allow us to use a Fokker-Planck equation that involves only the time and energy variables (Hamilton and Petrosian, 1992):

$$\frac{\partial f(E,t)}{\partial t} = \frac{\partial^2}{\partial E^2}\Big[D(E)f(E,t)\Big] - \frac{\partial}{\partial E}\Big[A(E)f(E,t) - \dot{E}f(E,t)\Big] - \frac{f(E,t)}{T(E)}, \quad (1)$$

where $f(E,t)$ is the electron distribution function in unit energy interval and $\dot{E}$ represents the energy loss rate. For the energy loss term, we consider the Coulomb loss and the synchrotron loss in the present study. In this equation, $D(E)$ and $A(E)$ are determined by the momentum diffusion coefficient, and the escape time $T(E)$ by the pitch angle diffusion coefficient. These quantities have been evaluated by Miller and Ramaty (1987) and Hamilton and Petrosian (1992) using the basic formulae in Melrose (1974, 1980) under a given form of wave spectrum. For our purpose, we evaluate these quantities as functions of wave spectral index n and total amplitude $\mathcal{E}_o$ under the assumed wave spectral density in the form of $\mathcal{E}(\omega) \propto \mathcal{E}_o(\omega/\omega_c)^{-n}$ above a cut-off frequency, ω_c. The explicit expressions for $D(E)$, $A(E)$, $T(E)$, and $\dot{E}$ are respectively given by Equations (2) and (3) in the Appendix. We note that these coefficients come out as very sensitive to background quantities such as magnetic fields and electron density.

The solution behavior that we want to investigate under this formalism is basically the dependence of the solution $f(E)$ on the form of wave spectrum and background physical quantities for a given wave amplitude $\mathcal{E}_{tot}$. Specifically, we look

for solutions in two different environments: a region with stronger fields and higher density ($B_2 = 6.0$, $N_{10} = 1.0$) and a region with weaker fields and lower density ($B_2 = 2.0$, $N_{10} = 0.1$) where B_2 and N_{10} represent the field strength and the electron density in units of 10^2 G and 10^{10} cm^{-3}, respectively. For simplicity, we denote these two sets of parameters as Region A and Region B, which are presumably to represent a lower and a upper part of a magnetic loop, respectively. Not much is known for the wave spectral index, n, and amplitude, $\mathcal{E}_o$. In the present study, we consider n in the range, $2 \leq n \leq 3$, for it leads to a reasonable acceleration time scale with choice of $10^{-10} < \mathcal{E}_o/(B^2/8\pi) < 10^{-3}$ where $B^2/8\pi$ is the self-energy of ambient magnetic fields.

We investigate the solution behaviors in the following way: To start, we seek the wave amplitude, $\mathcal{E}_o(t_p)$, for which the steady state solution, $f(E, t_p)$, of Equation (1) under conditions of Region A comes closest to the electron distribution as inferred from hard X-ray spectra observed at $t = t_p$. We then allow the wave to decay with time linearly on a time scale of τ, i.e., $\mathcal{E}_o(t) = \mathcal{E}_o(t_p)[1 - (t - t_p)/\tau]$ so that $f(E, t)$ decay with time to simulate the hard X-ray observation. The results for three different values of n ($n = 2.0$, 2.5, and 3.0) are shown in upper panels of Figure 4 where we specify $R \equiv 8\pi\mathcal{E}_o(t_p)/B^2$ and τ as defined above. The solid lines in Figure 4 represent $f(E, t_p)$ and the dashed lines $f(E, t_p + 80\text{s})$ calculated in this way. In each case, the wave decay time, τ, has been chosen to yield a similar amount of decrement of $f(E)$. In the next step, we feed the same wave spectra determined in Region A into Region B; the results are shown in lower panels of Figure 4. The solutions at Region B tend to show a more enhanced high energy tail in general. This trend simply reflects that particle escape is less efficient in a weaker field region and thus the high energy particles, once produced, survive longer. Such a different solution behavior in the two regions depict the different patterns of electron evolution in the lower and upper parts of a coronal magnetic loop if the waves propagate along the magnetic fields without damping.

We also draw attention to the dependence of $f(E)$ on the assumed wave spectral index, n. In general, the solution, $f(E)$, looks more like a thermal distribution at

low n but close to power-law distribution at high n. It is also noted that $f(E)$ at Region B shows larger time-variation at lower n in both amount and slope of high energy tails. In contrast, $f(E)$ at Region B calculated with $n = 3.0$ shows less variation, keeping a more or less constant energy slope. Such a characteristic variation of $f(E)$ with wave spectral index, n, makes it possible to deduce the wave spectrum that can best fit the particle distribution necessary to reproduce the observed hard X-ray spectra and microwave spectra. In the next section, we calculate the theoretical spectra of microwaves and hard X-rays from these particle distributions for agreement with observation.

4. Analysis of Hard X-ray Spectra and Microwave Spectra

We analyze the hard X-ray data first because the hard X-ray spectra are essentially shaped according to the particle distribution thus allowing a more straightforward analysis. We compute hard X-ray spectra from the particle distribution obtained in Region A (Figure 4) using the expression for the thick-target bremsstrahlung model (Brown, 1971). In Figure 5, we show theoretical hard X-ray spectra calculated with a model electron distribution for $n = 2.5$ (solid lines) and compare them with the observed hard X-ray data (cross symbols) from Figure 1. A good fit to the observation is obtained when we assume waves with amplitude $\mathcal{E}_o(t_p) = 2.7 \times 10^{-2}$ erg cm^{-3} which decay with time scale $\tau = 230$ s. It appears, however, that such a spectral fit can be made for various n if wave amplitude, $\mathcal{E}_o$, is accordingly adjusted. We therefore need an additional constraint to determine the underlying electron distribution and wave spectrum.

The needed constraint on the wave spectrum can be gained by requiring the theoretical microwave flux calculated from $f(E)$ in Region B to match the observation. Unlike the hard X-ray flux which concerns only the emissivity ($F_x \sim \int j(E)dE$), the microwave flux is given by $F_\mu \sim (j_\nu/\kappa_\nu)(1 - \exp[-\kappa_\nu d])$ for a uniform source along the line of sight where j_ν is the emissivity, κ_ν is the absorption coefficient and d is the path length. We use full expressions for j_ν and κ_ν of gyrosynchrotron

radiation (Ramaty, 1969; Trusen and Fejer, 1970; Benka and Holman, 1992) so as not to loose spectral details. We proceed by creating a model particle distribution that best reproduces the observed microwave fluxes at $t = t_p$. A good fit can be made when $\mathcal{E}_{tot} = 2.2\times10^{-2}$ erg cm^{-3} is used for $n = 2.5$, as shown in Figure 6 (Curve 1). In calculating microwave spectra, we assume that the microwave source has angular size, $\Omega = 2.2 \times 10^{-9}$ sterad and thickness, $d = 10$ arcsec. Note that this wave amplitude value is just close to the value demanded to fit hard X-ray data at $t = t_p$. Later evolution of microwave-emitting particles is modelled by allowing a finite decay rate of wave amplitude as we did in case of the hard X-rays and the resulting solutions at $t = t_p + 40$s and $t = t_p + 80$s are used to calculate theoretical microwave spectra. In Figure 6(a), we check results of this modelling against the observed spectra at the corresponding times. While results are made closer to the observation in the optically-thin regime, the results in the optically-thick regime largely disagree to the observation. This means that j_ν/κ_ν did not change as much as j_ν in time which determine the optically-thick and -thin spectrum respectively. This tendency for a relatively invariant optically-thick part is more prominent when we take a steeper wave spectrum (i.e., $n = 3.0$) where the slope of the electron distribution changes little with time. In other words, we need a certain amount of change in the shape of $f(E)$ in order to match the optically-thick part as well as the thin part of observed spectra.

As a plausible way that we can accommodate variations of both the optically-thick and -thin microwave fluxes, we consider a case where the wave spectrum not only decays in amplitude but also flattens in shape. A motivation for this model is from the observation that $f(E)$ calculated with lower wave spectral index, n, has more rapidly decreasing high energy tails (Figure 4) as demanded to reproduce the drop of microwave spectra in the decay phase. Under this notion, we allow the wave spectrum to vary in both amplitude and spectral slope. As a result, a satisfactory fit to the observed spectra is made when the wave spectral index is lowered from $n = 2.5$ to $n = 2.25$ and wave amplitude decreases exponentially with $1/e$-folding time of 30 s (Curves 4 and 5 in Figure 6(b)). Such an evolutionary pattern of wave

spectra is basically in agreement with the general picture of wave damping (cf., Krall and Trivelpiece, 1973).

As alternative ways to explain microwave activities, one may consider, on a general basis, a particle sink term which is effective in shaping only the high energy tail of the electron distribution in a desired way. Qualitatively, the radiative loss appeared to be a good candidate. We examined this possibility by adding the synchrotron loss term, $\dot{E}_{sync}$, given by Equation (3) to find that, under the rather weak field strength we consider, the synchrotron term is inefficient. Another possible way is to invoke a higher value of cut-off frequency that limits the growth of high energy tails of electron distribution (cf., Holt and Ramaty, 1969). Unfortunately, we have at present no good theoretical ground to specify these quantities in more detail. Until then, we conclude that a time-dependent change of wave spectra in both amplitude and shape could explain the observed microwave spectral variation.

5. Discussion

In this paper, we analyzed microwave data and hard X-ray data of the 1989 March 18 flare in terms of a model in which the microwave source and the hard X-ray source are physically separated but related via waves passing through them. From a quantitative analysis, we conclude that the decoupling of microwaves and hard X-rays observed at the decay phase is most likely due to a difference in the trapping of high energy particles of each source region in response to the decay of the Whistler waves. In order to clarify our line of approach, we discuss the assumptions made in our modelling and implications of our results by comparing with those of other approaches.

5.1. THE MODEL FOR PARTICLE DISTRIBUTION

We assumed that microwave emitting particles and hard X-ray particles are produced as a result of stochastic acceleration by Whistler waves, following previous

works (e.g., Melrose 1974, 1980; Miller and Ramaty, 1987, 1989; Hamilton and Petrosian, 1992). As another class of model for flare particles, the DC-current model has been favored to account for the break-down type of hard X-ray spectrum often seen at the initial rise phase (e.g., Lin and Schwarz, 1987; Dulk, Kiplinger, and Winglee, 1992). We note that our approach does not necessarily exclude the possible role of DC-current in accelerating particles at the initial phase ($t < t_p$), because our investigation started with an equilibrium solution at $t = t_p$ that is constrained by observed radiation spectra. Even in a DC-current model, it is commonly presumed that plasma turbulence builds up during flares to produce higher energy particles that emit microwaves (e.g., Bai and Dennis, 1985; Winglee *et al.*, 1991; Dulk, Kiplinger, and Winglee, 1992).

Benka and Holman (1992) considered a DC-current model for microwave-emitting electrons in an attempt to explain the invariance of peak frequency of microwave burst spectra during flares as reported by Stähli, Gary, and Hurford (1989). However, their model (their Figure 7) leads to a consequence that only the fluxes around the peak frequency keep changing while the optically-thick fluxes are relatively invariant (as in Figure 6a). As discussed in Section 4.2, such model-prediction is inconsistent with the observation that fluxes at all frequencies show more or less the same amount of decrement (or increment) during the impulsive phase (Figure 1). To explain this, some change in the slope of electron energy distribution is needed as in Figure 6b.

We, however, believe that plasma turbulence driven by the DC-currents might play an important role in particle evolution in the period under consideration. A detailed study in this line has been presented by Moghaddam-Taaheri and Goertz (1990) showing that the maximum phase leads to a rather flat emissivity spectrum in agreement with the observation by Marsh *et al.* (1981). Since the flare spectra presented by Marsh *et al.* (1981) were from a weak event and had a rather unusual spectral shape, it is yet to be checked whether their theoretical results can help to understand more typical microwave spectra. The majority of microwave spectra

show a spectral peak at 5-10 GHz and decline above the peak frequency (Guidice and Castelli, 1975). In order to reproduce this more common spectral behavior, we need a decreasing emissivity above 10 GHz, which in turn requires particle distribution falling sufficiently at least below 1 MeV. As Moghaddam-Taaheri and Goertz (1990) commented, the particle escape term is a likely candidate that can lead to such a particle distribution (see also Holt and Ramaty, 1969). In the present model, the role of particle escape by wave scattering is emphasized to match the observed microwave spectra.

5.2. IMPLICATION OF OUR RESULTS

The results presented in this paper are based on the spectral fitting of a single event which is chosen primarily to ease the analysis of microwave data. Nevertheless, our results of analysis may provide a complementary view to the previous studies made without spectral information in microwaves, since the data of this event show a rather typical behavior (Stähli, Gary, and Hurford, 1989).

5.2.1. *For the Study of Time-Correlations of Microwaves and X-Rays*

Lu and Petrosian (1990) investigated the evolution of particles that produce microwaves and hard X-rays with emphasis on the time delay between their peak fluxes. They noted that the thick-target model for hard X-rays reproduces the microwave flux in the rising phase but too little microwave flux in the decay phase. In an attempt to explain this, they invoke flattening of the electron distribution at $\geq$ 300 keV during the decay. The model presented in this paper basically agrees with this view and it also suggests a physical interpretation why this should happen. It is that the microwave particles in the decay phase belong to an environment that permits longer survival time as compared to the hard X-ray particles in the thick target model. It is also noted that the electron distribution is harder in the microwave-emitting region owing to less efficient energy loss in our model.

On the other hand, results of the present work warrant neither the study that incorporates spectral parameters from microwaves and hard X-rays nor the study of time-correlation of both to estimate the energy of microwave-emitting electrons. As a reason, the low energy (< 100 keV) hard X-ray photons in our data has a seemingly good correlation with the microwaves at most frequencies. Such a result may not be used to argue the low energy origin of microwaves if the source regions for both were physically separated as we proposed. In fact, the theory of microwave radiation (e.g., Takakura, 1973; Petrosian, 1982) predicts that microwaves are emitted mostly from high energy electrons ($>$ a few 100 keV). In more detail, high energy electrons are responsible not only for the high-frequency flux through emission at higher harmonics but also for the low-frequency flux through emission and absorption at lower harmonics, which makes it difficult to set one-to-one correspondence between the energy of hard X-ray photons and the frequency of microwaves in general.

5.2.2. *For the Loop-Top Model of Microwave Sources*

A more direct evidence for the separation of two radiation sources, of course, comes from observations with high spatial resolution. In many occasions, the microwaves are observed to come from the loop top (Marsh and Hurford, 1980; Marsh *et al.*, 1980; Kundu, Bobrowsky, and Velusamy, 1981; Kundu, Schmahl, and Velusamy, 1982). In contrast, results of the Hard X-ray Imaging Spectrometer (HXIS) on the SMM tend to show that the X-rays primarily come from the foot-points of loops (e.g., Hoyng *et al.*, 1981). The result for hard X-rays agrees with the prediction of the thick-target model (Brown, 1971). However, the result for microwaves was once regarded as puzzling not only because microwaves had been expected to be cospatial with hard X-rays but because microwaves are naively expected to be brighter at footpoints where magnetic fields are stronger. Theoretical approaches to resolve this puzzle have been made in two different ways: In one, the top-brightness is attributed to the radiative transfer effect that affects microwaves but not hard X-rays (see Section 4). The model-computations found that either the top or the foot-points may appear brighter depending on how the gyrosynchrotron self-absorption

varies with field inhomogeneity and the observing frequency (e.g., Klein and Trottet, 1984; Alissandrakis, 1986; Preka-Papadema and Alissandrakis, 1992). This model-prediction agrees with some observations made with high spatial resolution at multi-frequencies (e.g., Shevgaonkar and Kundu, 1985; Kundu, 1989). While the study of source structure using the radiative property of microwaves is certainly an important mission, this approach does not fully address the physics of the flare particles. In the other theoretical approach, Petrosian (1982) investigated various possibilities that the top-bright microwave radiation is due to variation of the particle distribution function along a flaring loop. Although his optically-thin approach does not include radiative transfer effects (i.e., absorption), it provides a means to assess the particle distribution from the resulting radiation.

The model presented in this paper is an attempt to incorporate both of these two: the radiative transfer (Figure 6) and the particles (Figure 4) in a simpler form. The simplification of the radiative transfer problem owes to the simple geometry of this limb event while the simple model for particle diffusion is due to ignoring spatial details like field convergence and spatial convection in the Fokker-Planck equation. Our simple approach, however, clarifies how these two factors interplay to modulate the resulting radiation. In our results, the hard X-ray source is located low due to higher density there and the microwave source is located high due to more abundant energetic particles, in spite of weaker fields at the region. Without proper evaluation of the relative importance of particles and magnetic fields, the observational properties of microwave radiation may not be correctly understood. The future study of microwave data should therefore be directed toward resolving these two factors.

5.2.3. *For the Insensitivity of Microwave Spectra to Hard X-ray Spectra*

As a most important consequence of the present model, we can account for the rather independent time-variation of microwave spectra from that of hard X-rays during

the decay phase by separating the hard X-ray emitting region from the microwave-emitting region as mentioned above. In principle, the insensitivity of microwaves to hard X-rays may result solely from the fact that microwaves and hard X-rays are emitted by electrons at different energies (Takakura, 1973; Petrosian, 1989). In the present study, however, separation of the sources is needed in order to explain the microwave excess relative to hard X-rays in the decay phase.

In general, hard X-ray spectra are known to evolve in shape during flares (e.g., Lin and Schwartz, 1987; Dulk, Kiplinger, and Winglee, 1992) and has thus been regarded as yielding a more direct diagnostic. This is probably due to the Coulomb loss term that plays a role in shaping the low energy part (10 keV to 200 keV) of the electron distribution against an acceleration term (see Hamilton and Petrosian, 1992). Such a variation can be manifested in the hard X-ray spectrum covering a similar energy band. On the other hand, microwave spectra are largely determined by the higher energy electrons (say > 500 keV) and thus do not necessarily show the same spectral behaviors.

Microwaves can, however, provide other information on the electron distribution. As we can learn from Figure 6(a), the fitting to the optically-thin region was relatively easy and has more choices of possible candidates. As we attempt to match the optically-thick part as well (Figure 6(b)), the possible candidates for model particle distributions are more limited. The fact that fitting to microwave spectra as a whole necessitates a greater restriction on the scenario of particle evolution may increase the value of microwaves as another independent diagnostic of flare-produced electrons.

Acknowledgement

We thank Kim Tolbert for providing the hard X-ray data in the present form. Observations at OVRO were funded by NSF grants ATM-9013173 and AST-8919770

to the California Institute of Technology. One of us (JWL) has been supported by NASA grant NAGW-3005 and NAGW-1972.

Appendix

We here calculate the momentum diffusion rate and escape time for electrons interacting with the Whistler waves under the assumed form of wave spectral density. For simplicity, we assume the waves propagate mostly along the ambient magnetic field lines; that is, we set $|\cos\theta| \equiv 1$ in (A.7) of Melrose (1974). Then the momentum diffusion coefficient D_{pp} and pitch angle diffusion coefficient $D_{\mu\mu}$ are given as (Melrose, 1974)

$$D_{\mu\mu}(p,\mu) = \frac{4\pi^3 e^2}{\gamma^3\beta^2 m_e^2 c^2}\left(\frac{\Omega_e}{\omega_p}\right)^2 \frac{1-\mu^2}{\mu^2}\mathcal{E}(\omega_R),$$
$$D_{pp}(p,\mu) = \left(\frac{m_e c}{\beta|\mu|}\right)^2\left(\frac{\Omega_e}{\omega_p}\right)^4 D_{\mu\mu}(p,\mu),$$

where m_e and c are the electron mass and the speed of light, respectively; Ω_e and ω_p are the electron gyrofrequency and the plasma frequency, respectively, and μ is the cosine of the pitch angle.

$\mathcal{E}(\omega)$ is the spectral energy density of Whistler waves in units of [erg cm^{-3} s]. In this study, we assume that wave spectrum is given by a power-law of wave frequency as:

$$\mathcal{E}(\omega) = \mathcal{E}_o\left(\frac{n-1}{\omega_c}\right)\left(\frac{\omega}{\omega_c}\right)^{-n} \quad \text{for} \quad \omega \geq \omega_c,$$

where $\mathcal{E}_o$ is the wave amplitude in units of [erg cm^{-3}]. If the wave spectrum is given in a form of one-dimensional wavenumber as $\mathcal{E}(k) \propto k^{-q}$, the spectral index q and n are related by $q = 2n - 1$ (cf., Hamilton and Petrosian, 1990). In the above

expressions, ω_c is the cut-off frequency and ω_R is the resonant frequency of waves. ω_R is related to the electron momentum, p, as

$$\omega_R = \frac{\Omega_e}{\gamma^2\beta^2}\left(\frac{\Omega_e}{\omega_p}\right)^2\frac{1}{\mu^2} = \frac{1.71\times10^8}{\mu^2}B_2^3N_{10}^{-1}\left(\frac{p}{m_ec}\right)^{-2} \quad [\mathrm{s}^{-1}],$$

where B_2 is magnetic field strength in units of 10^2 G, and N_{10} is electron number density in units of 10^{10} cm^{-3}. We set the lower cut-off frequency, ω_c, of the wave spectrum according to the lower cut-off wavenumber, $k_c = k_{th} \equiv \Omega_p/v_A$, as proposed by Hamilton and Petrosian (1992):

$$\omega_c = \frac{k_{th}^2c^2\Omega_e}{\omega_p^2} = 9.61\times10^5B_2 \quad [\mathrm{s}^{-1}],$$

where v_A is the Alfvén speed.

Using these expressions, the momentum diffusion coefficient and the escape time come out as (cf., Miller and Ramaty, 1987; Hamilton and Petrosian, 1992)

$$\begin{aligned}
D(E) &= \langle D_{pp}(p,\mu)\rangle\frac{\beta^2}{m_e^2c^2} \\
&= 1.16\times10^9(5.62\times10^{-3})^n\frac{n-1}{(2n-1)(2n-3)}B_2^{5-2n}N_{10}^{n-3}\mathcal{E}_o\beta(\gamma\beta)^{2n-3}, \\
A(E) &= \frac{m_ec}{p^2}\frac{\partial}{\partial p}\left[\frac{p^2}{\beta}D(E)\right] \\
&= 1.16\times10^9(5.62\times10^{-3})^n\left(\frac{n-1}{2n-3}\right)B_2^{5-2n}N_{10}^{n-3}\mathcal{E}_o(\gamma\beta)^{2n-4}, \\
T(E) &= \langle D_{\mu\mu}(p,\mu)\rangle\frac{L^2}{\beta^2c^2} \\
&= 1.36\times10^{10}(5.62\times10^{-3})^n\frac{n-1}{(2n+1)(2n-1)}B_2^{1-2n}N_{10}^{n-1}\mathcal{E}_o\gamma(\gamma\beta)^{2n-4},
\end{aligned} \tag{2}$$

where L is the size of acceleration region; we assumed $L = 10^{10}$ cm. The dimensions of $D(E)$, $A(E)$, and $T(E)$ are respectively [s^{-1}], [s^{-1}], and [s]. Note that these quantities are evaluated for E in units of m_ec^2.

The energy loss rates for Coulomb loss and synchrotron loss are given as:

$$\begin{aligned} \dot{E}_{coul} &= 6.00 \times 10^{-3} N_{10} \beta^{-1} \\ \dot{E}_{sync} &= 1.29 \times 10^{-5} B_2^2 \gamma^2 \beta^2 \end{aligned} , \tag{3}$$

in units of $[s^{-1}]$ from Hamilton, Lu, and Petrosian (1990).

References

Alissandrakis, C. E.: 1986, *Solar Phys.* **104**, 207.

Ashwanden, M. J.: 1990, *Astron. and Astrophys. suppl.* Ser. **85**, 1141.

Bai, T. and Dennis, B.: 1985, *Astrophys. J.* **292**, 699.

Bastian, T. S. and Gary, D. E.: 1992, *Solar Phys.* **139**, 357.

Benka, S. G. and Holman, G. D.: 1992, *Astrophys. J.* **391**, 854.

Böhme, A., Fürstenberg, F., Hildebrandt, J., Hoyng, P., Krüger, A., Saal, O., and Stevens, G. A.: 1976, HHI-STP-Report No. 6, Astronomical Institute Utrecht.

Böhme, A., Fürstenberg, F., Hildebrandt, J., Saal, O., Krüger, A., Hoyng, P., and Stevens, G. A. 1977, *Solar Phys.* **53** 139.

Brown, J. C.: 1971, *Solar Phys.* **18**, 489.

Brown, J. C.: 1975, in S. R. Kane, (eds.), *Solar Gamma-, X-, and EUV Radiation*, p. 245.

Cornell, M. E., Hurford, G. J., Kiplinger, A. L., and Dennis, B. R.: 1984, *Astrophys. J.* **279**, 875.

Crannell, C. J., Frost, K. T., Mätzler, C., Ohki, K., and Saba, J. L.: 1978, *Astrophys. J.* **223**, 620.

Dennis, B. R.: 1988, *Solar Phys.* **118**, 49.

Dennis, B. R. and Schwartz, R. A.: 1989, *Solar Phys.* **121**, 75.

Dulk, G. A., Kiplinger, A. L., and Winglee, R. M.: 1992, *Astrophys. J.* **389**, 756.

Dulk, G. A., McLean, D. J., and Nelson, G. J.: 1985 in *Solar Radiophysics*, D. J. Nelson and N. R. Labrum, (eds.), Cambridge Univ Press, Chapter 4.

Guidice, D. A. and Castelli, J. P.: 1975, *Solar Phys.* **44**, 155.

Hamilton, R. J. and Petrosian, V.: 1992, *Astrophys. J.* **398**, 350.

Hamilton, R. J., Lu, E. T., and Petrosian, V.: 1990, *Astrophys. J.* **354**, 726.

Heyvaerts, J.: 1981, in *Solar Flare Magnetohydrodynamics*, E. R. Priest, (eds.), Cambridge Univ Press, Chapter 8, Gordon and Breach, New York.

Holman, G. D. and Benka, S. G.: 1992, *Astrophys. J.* **400**, L79.

Holt, S. S. and Ramaty, R.: 1969, *Solar Phys.* **8**, 119.

Hoyng, P., Duijveman, A., Machado, M. E., Rust, D. M., Švestka, Z., Boelee, A., de Jager, C., Frost, K. F., Lafleur, H., Simnett, G. M., van Beek, H. F., and Woodgate, B. E.: 1981, *Astrophys. J.* **246**, L155.

Johns, C. M. and Lin, R. P.: 1992, *Solar Phys.* **137**, 121.

Kaufmann, P., Strauss, F. M., Costa, J. E. R., Dennis, B. R., Kiplinger, A., Frost, K. J., and Orwig, L. E.: 1983, *Solar Phys.* **84**, 311.

Klein, K. L. and Trottet, G.: 1984, *Astron. Astrophys.* **141**, 67.

Krall, N. A. and Trivelpiece, A. W.: 1973, *Principles of Plasma Physics*, McGraw-Hill, New York.

Kundu, M. R.: 1989, *Solar Phys.* **121**, 153.

Kundu, M. R., Bobrowsky, M., and Velusamy, T.: 1981, *Astrophys. J.* **251**, 342.

Kundu, M. R., Schmahl, E. J., and Velusamy, T.: 1982, *Astrophys. J.* **253**, 963.

Lin, R. P. and Schwartz, R. A.: 1987, *Astrophys. J.* **312**, 462.

Lu, E. T. and Petrosian, V.: 1989, *Astrophys. J.* **338**, 1122.

Lu, E. T. and Petrosian, V.: 1990, *Astrophys. J.* **354**, 735.

Marsh, K. A. and Hurford, G. J.: 1980, *Astrophys. J.* **240**, L111.

Marsh, K. A., Hurford, G. J., Zirin, H., Dulk, G. A., Dennis, B. R., Frost, K. J., and Orwig, L. E.: 1981, *Astrophys. J.* **251**, 797.

Marsh, K. A., Hurford, G. J., Zirin, H., and Hjellming, R. M.: 1980, *Astrophys. J.* **242**, 352.

Melrose, D. B.: 1974, *Solar Phys.* **37**, 353.

Melrose, D. B.: 1980, *Plasma Astrophysics*, Vol. 1 and 2, Gordon and Breach, New York.

Moghddam-Taaheri E. and Goertz, C. K.: 1990, *Astrophys. J.* **352**, 361.

Miller, J. A. and Ramaty, R.: 1987, *Solar Phys.* **113**, 195.

Miller, J. A. and Ramaty, R.: 1989, *Astrophys. J.* **344**, 973.

Miller, J. A. and Steinacker, J.: 1992, *Astrophys. J.* **399**, 284.

Petrosian, V.: 1982, *Astrophys. J.* **255**, L85.

Petrosian, V.: 1989, in E. R. Priest and V. Krishan, (eds.), Basic Plasma Processes On The Sun, IAU Symp. No. 142, p. 391.

Preka-Papadema, P. and Alissandrakis, C. E.: 1992, *Astron. and Astrophys.* **257**, 307.

Ramaty, R.: 1969, *Atrophys. J.* **158**, 753.

Shevgaonkar, R. K. and Kundu, M. R.: 1985, *Astrophys. J.* **292**, 733.

Stähli, M., Gary, D. E., and Hurford, G. J.: 1989, *Solar Phys.* **120**, 351.

Stähli, M., Gary, D. E., and Hurford, G. J.: 1990, *Solar Phys.* **125**, 343.

Steinacker, J. and Miller, J. A.: 1992, *Astrophys. J.* **393**, 764.

Takakura, T.: 1973, in Ramaty, R., Stone, R. G., (eds.), *High Energy Phenomena on the Sun*, NASA/GSFC-SP-342, p. 179.

Trulsen, J. and Fejer, J. A.: 1970, *J. Plasma Phys.* **4**, 825.

Winglee, R. M., Dulk, G. A., Bornmann, P. L., and Brown, J. C.: 1991, *Astrophys. J.* **375**, 382.

Figure Captions

Fig. 1. Time-sequence of flux spectra of microwaves (upper panels) and hard X-rays (lower panels) of 1989 March 18 flare at 6 consecutive times in intervals of 20s each, including the time of peak brightness, t_p (21:56:40 UT). The vertical bars in X-ray data centered on each channel represent error range of X-ray flux. Error bar is not given for microwave data.

Fig. 2. Time profiles of (a) microwaves and (b) hard X-rays. Time shown here is relative to the peak time, t_p = 21:56:40 UT. Frequencies of microwaves and energy ranges of X-ray channels are specified.

Fig. 3. Phases (upper panels) and FWHMs (lower panels) as a function of frequency at 5 consecutive times starting from t_p.

Fig. 4. Fokker-Planck solutions obtained in two physical conditions: $(B_2,\ N_{10})$ = (6.0, 1.0) in Region A and (2.0, 0.1) in Region B, and for three wave spectral indices: n = 2.0, 2.5, and 3.0. In each frame the solid line represents the equilibrium solution calculated with wave amplitude, $R = 8\pi\mathcal{E}_o/B^2$ with B = 200 G and the dashed line, its evolution after 80s provided the wave amplitude diminish linearly with time scale τ as specified.

Fig. 5. A model fit to the observed hard X-ray spectra (Figure 1) at 5 consecutive times. Model parameters used to compute particle evolution are specified at the upper right corner.

Fig. 6. Observed microwave spectra *vs.* calculated spectra at $t = t_p$ (Curve 1), t_p+40s (Curves 2 and 4), and t_p + 80s (Curves 3 and 5) in case (a) where the waves change only in amplitude and in case (b) where the waves change both in amplitude and in spectral shape. The rates of change are specified in the upper left corner.

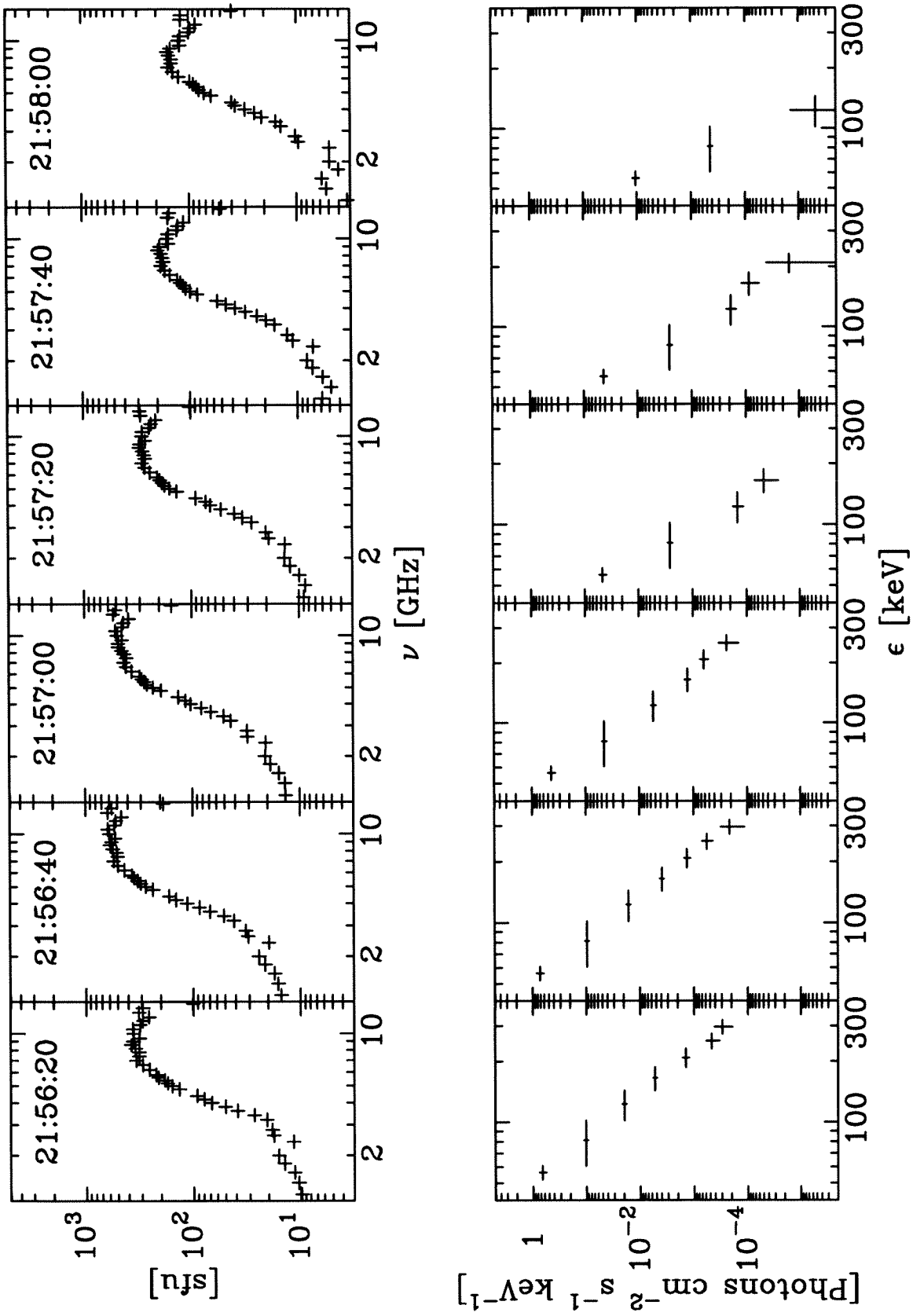
21:56:20
21:56:40
21:57:00
21:57:20
21:57:40
21:58:00
[sfu]
ν [GHz]
[Photons cm⁻² s⁻¹ keV⁻¹]
ε [keV]

Figure 1

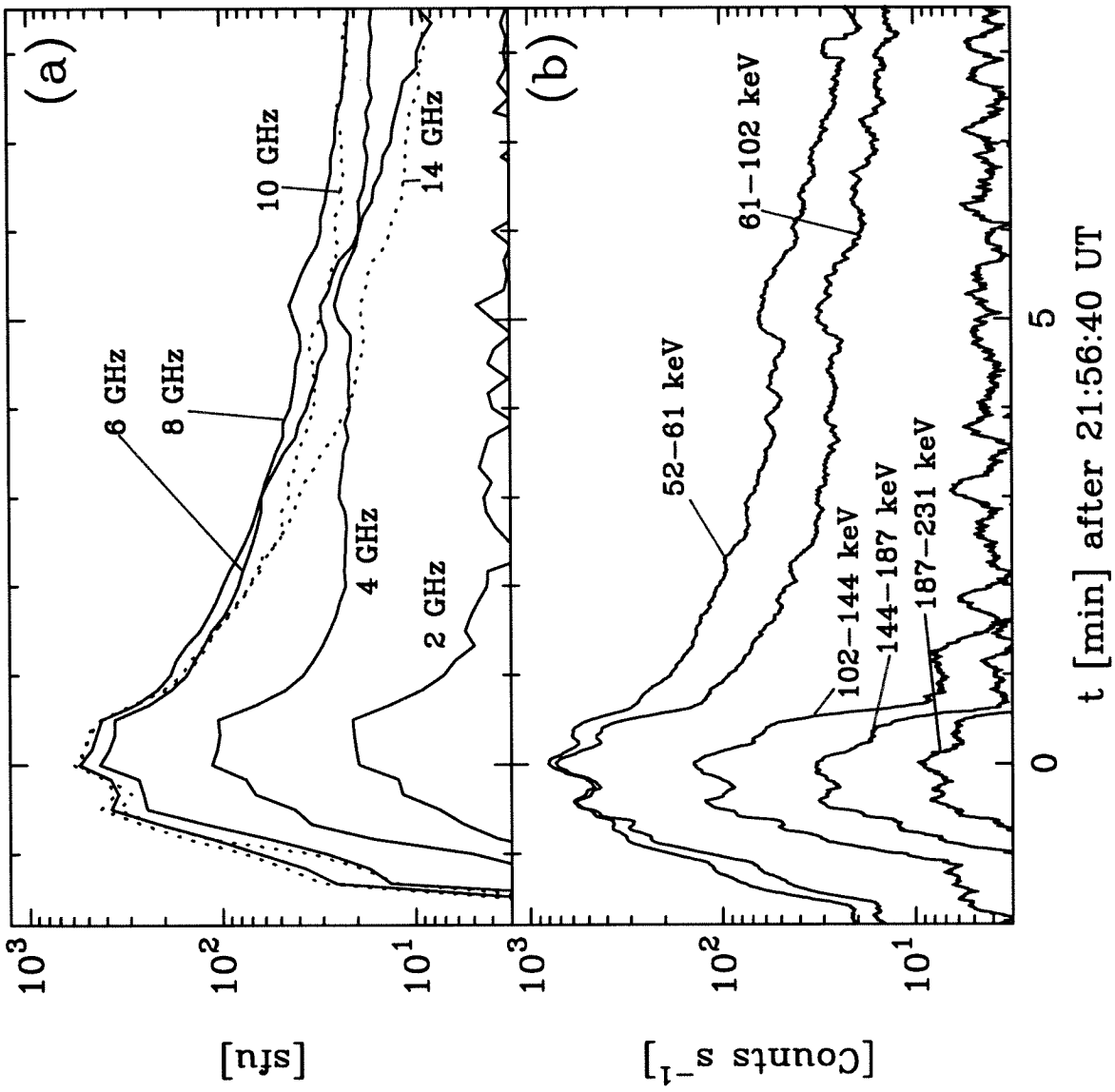
(a)
(b)
8 GHz
6 GHz
10 GHz
14 GHz
4 GHz
2 GHz
52–61 keV
61–102 keV
102–144 keV
144–187 keV
187–231 keV
[sfu]
[Counts s^{-1}]
t [min] after 21:56:40 UT
0
5

Figure 2

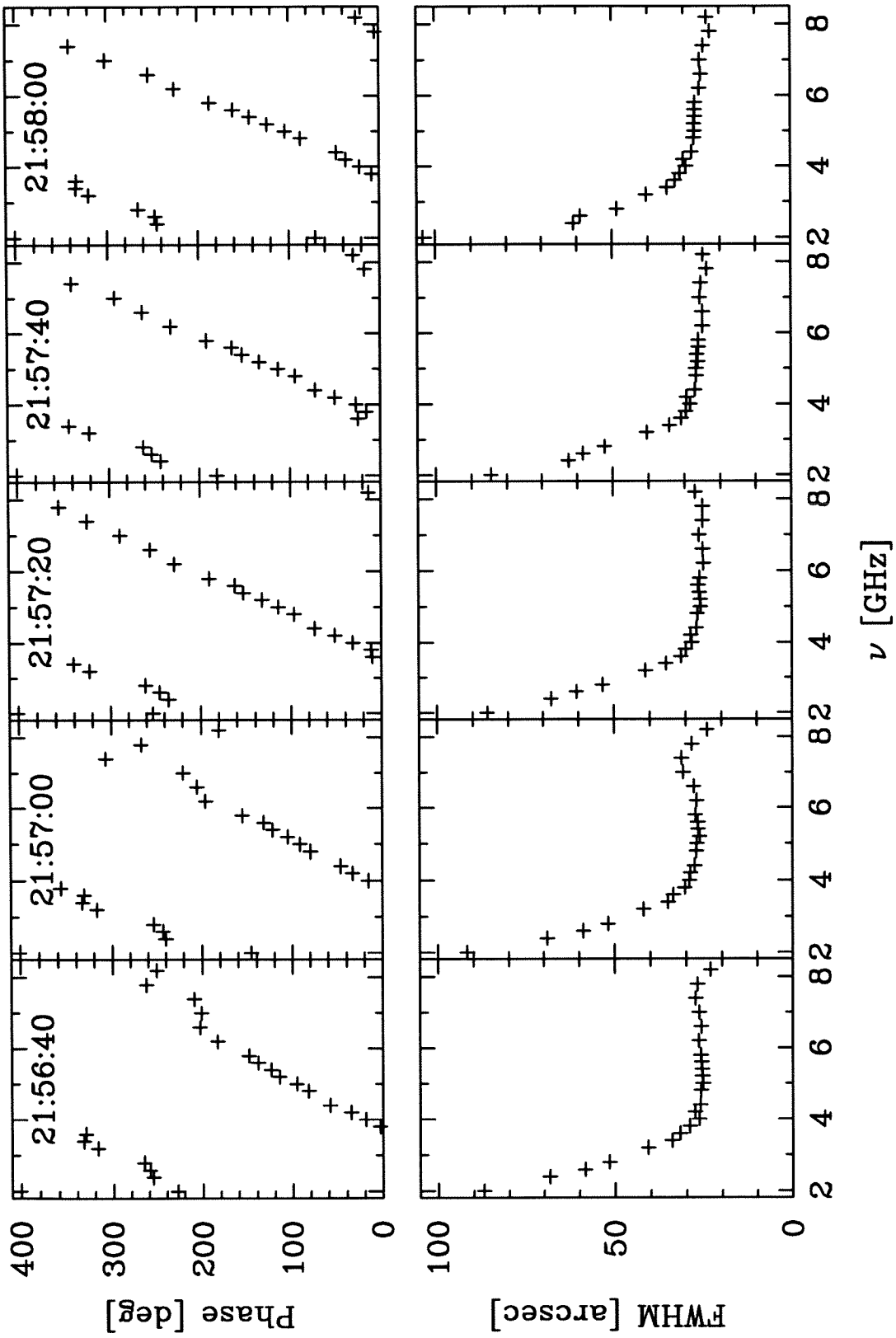
21:58:00
21:57:40
21:57:20
21:57:00
21:56:40
Phase [deg]
FWHM [arcsec]
ν [GHz]

Figure 3

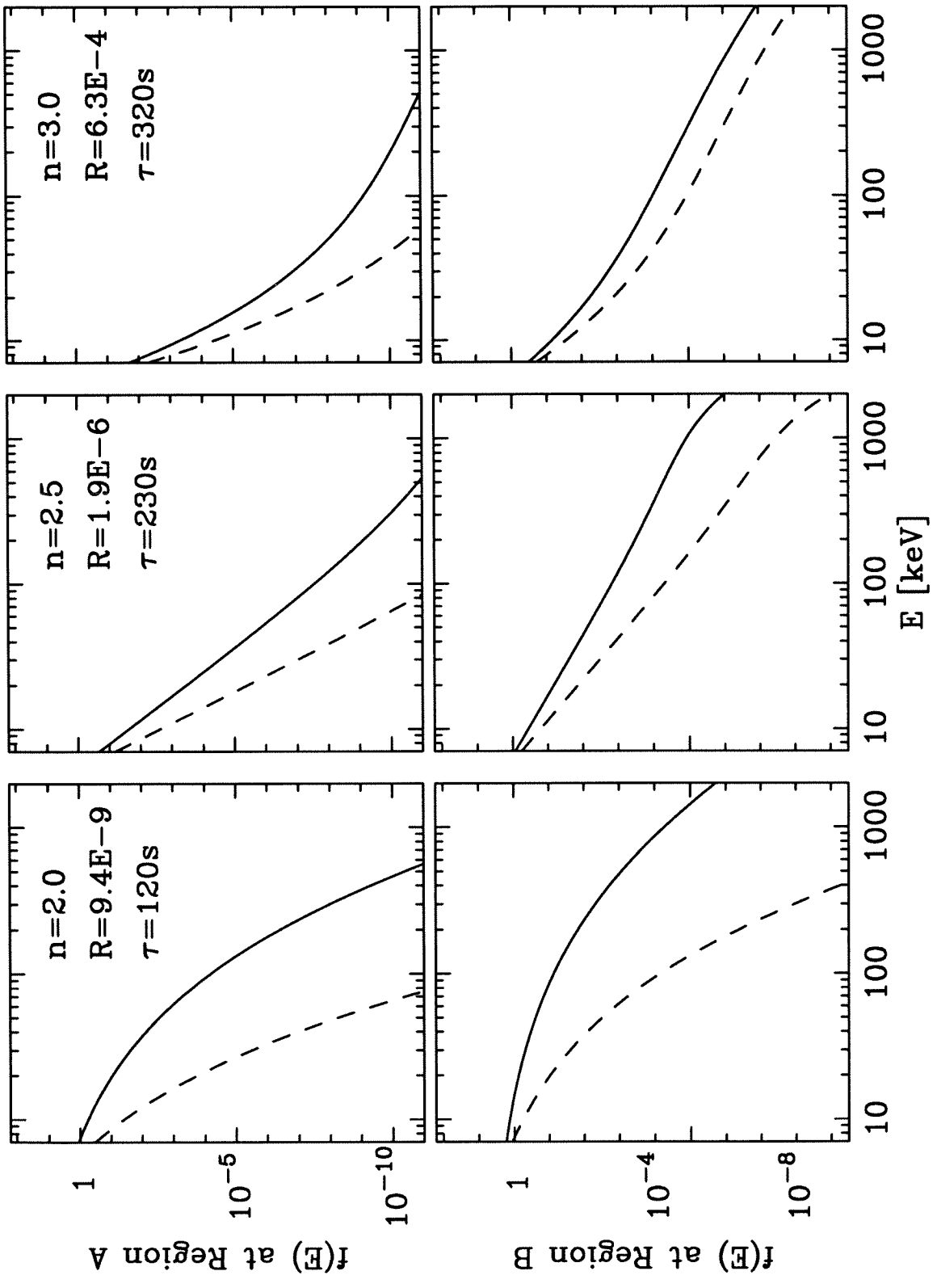
n=2.0
R=9.4E−9
τ=120s
n=2.5
R=1.9E−6
τ=230s
n=3.0
R=6.3E−4
τ=320s
f(E) at Region A
f(E) at Region B
1
10^−5
10^−10
10^−4
10^−8
10
100
1000
E [keV]

Figure 4

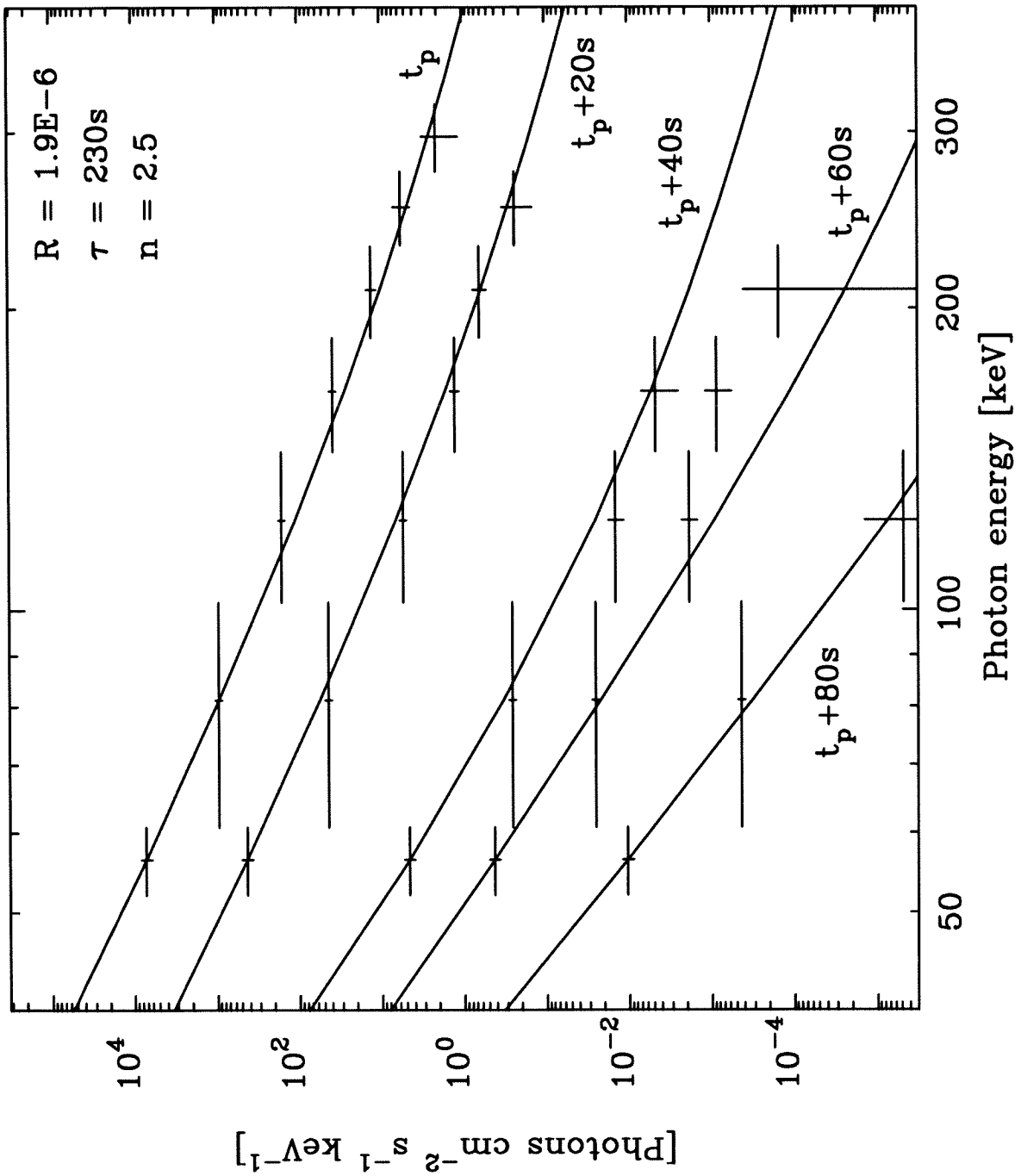
R = 1.9E-6
τ = 230s
n = 2.5
t_p
t_p+20s
t_p+40s
t_p+60s
t_p+80s
Photon energy [keV]
50
100
200
300
10^4
10^2
10^0
10^{-2}
10^{-4}
[Photons cm^{-2} s^{-1} keV^{-1}]

Figure 5

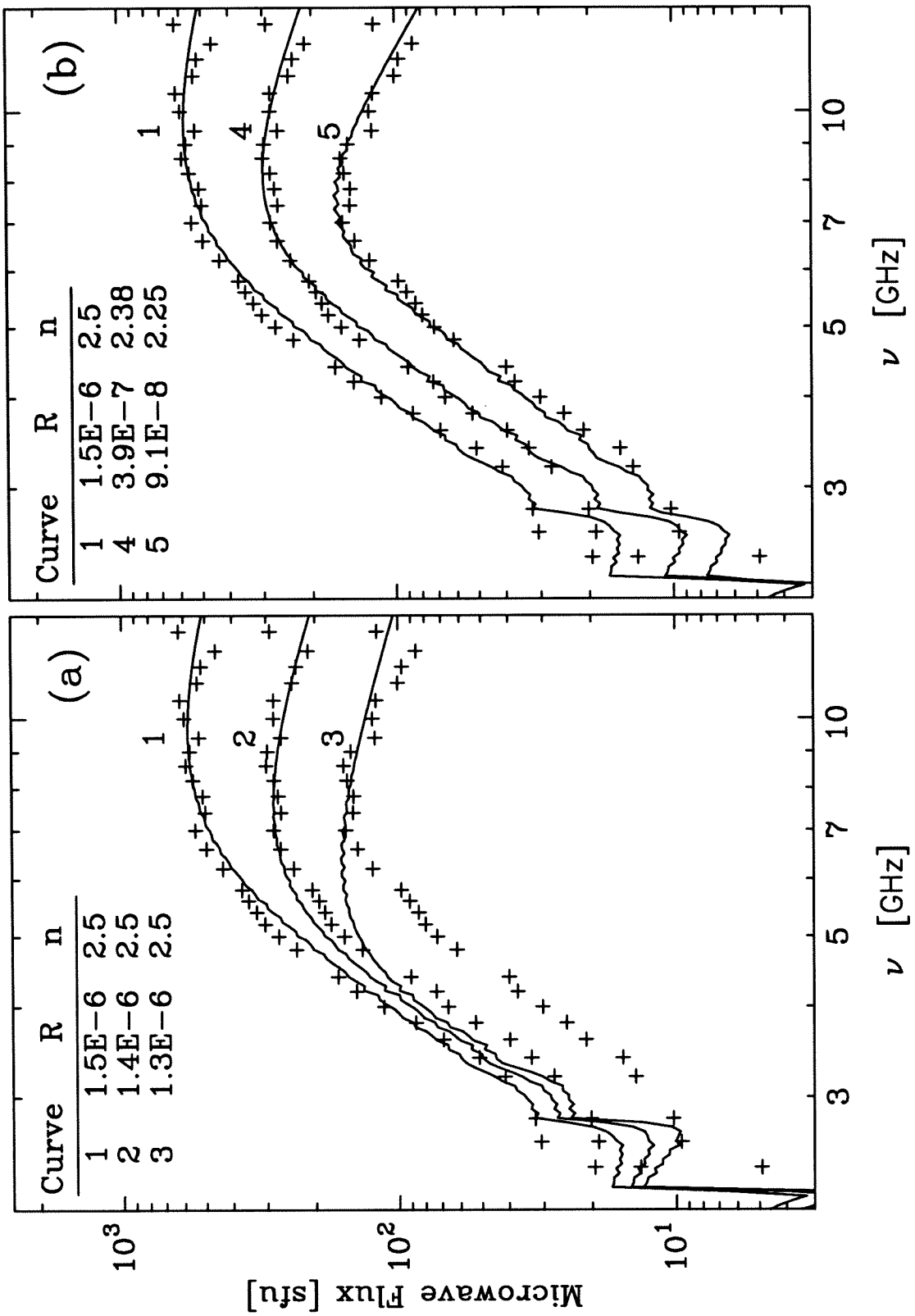
(a)
Curve R n
1 1.5E−6 2.5
2 1.4E−6 2.5
3 1.3E−6 2.5
(b)
Curve R n
1 1.5E−6 2.5
4 3.9E−7 2.38
5 9.1E−8 2.25
Microwave Flux [sfu]
ν [GHz]

Figure 6

Chapter 6

Flat microwave spectra seen at X-class flares

Submitted to the **Solar Physics**

Abstract

We report peculiar spectral activity of four large microwave bursts as obtained from the Solar Arrays at the Owens Valley Radio Observatory during observations of X-class flares on 1990 May 24 and 1991 March 7, 8, and 22. Main observational points that we newly uncovered are: (1) flat flux spectra over 1-18 GHz in large amounts of flux ranging from 10^2 to 10^4 sfu at the maximum phase, (2) a common evolutionary pattern in which the spectral region of dominant flux shifts from high frequencies at the initial rise to low frequencies at the decaying phase, and (3) unusual time profiles that are impulsive at high frequencies but more extended at lower frequencies.

In an attempt to elucidate these new properties, we carry out the model-calculations of microwave spectra under assumptions of gyrosynchrotron mechanism and a dipole field configuration to reproduce the observational characteristics. Our results are summarized as follows: First, a flat microwave spectrum reaching up to 10^2 - 10^4 sfu may occur in a case where a magnetic loop is extended to an angular size of $\sim$(0.7-7.0)$\times 10^{-7}$ sterad and contains a huge number ($N(E > 10\mathrm{keV}) \sim 10^{36}$ - 10^{38}) of nonthermal electrons with power law index $\delta \sim 3$ - 3.5 over the entire volume. Second, the observed spectral activity could adequately be accounted for by the shrinking of the region of nonthermal electrons to the loop top and by the softening of the power-law spectrum of electrons in a timescale ranging 3 - 45 minutes depending on the event. Third, the extended microwave activity at lower frequencies is probably due to electrons trapped in the loop top where magnetic fields are low. Finally, we clarify the physical distinction between these large, extended microwave bursts and the gradual/post microwave bursts often seen in weak events both of which are characterized by long-period activity and broadband spectra.

1. Introduction

The large microwave bursts which are characterized by high fluxes over 10^3 solar flux units (sfu) and a flat spectral shape over 1-20 GHz have been reported by Hachenberg and Wallis (1961). Most attention was given to the flat spectral shape, which is against the prediction of the theory of gyrosynchrotron radiation from a uniform source (cf., Ramaty and Petrosian, 1972; Klein and Trottet, 1984). Since no further reports of such flat and high microwave flux spectra followed after Hachenberg and Wallis (1961), the theoretical efforts have been limited to those addressing only the instantaneous spectral shape at the maximum phase (Ramaty and Petrosian, 1972; Klein and Trottet, 1984). For the purpose of further exploring properties of this kind of microwave activity, we examined the data gathered from the solar-dedicated telescope at the Owens Valley Radio Observatory (OVRO) over a few years around the last Solar Maximum to find four samples, the 1990 May 24 and 1991 March 7, 8, and 22 flares, which show a similar spectral behavior at the maximum phase. Having examined these data in time as well as with high spectral resolution, we find the following properties are worthy of new attention:

First, these microwave bursts exhibit radio fluxes ranging from 10^2 sfu to 10^4 sfu over the frequency band of 1-18 GHz, with two of them having peak fluxes over 10^4 sfu. The latter value is comparable to the highest microwave fluxes ever reported. As examples, Croom and Powell (1971) reported two events with fluxes over 10^4 sfu at 19 GHz among 148 bursts gathered over 2.5 years; Tanaka (1969) stated that the highest microwave flux ever recorded at 3 GHz was 3.2×10^4 sfu in the 1969 March 30 flare; the 1991 June 6 flare attained $\sim 5 \times 10^4$ sfu at 2.7 GHz (Solar Geophysical Data, 1991, Prompt Reports, No. 564). Explanation of such a high level of flux may require a new quantitative model simply because it far exceeds the previously known maximum flux value used as an observational constraint in a theoretical model (Ramaty and Petrosian, 1972). Second, temporal evolution of these burst spectra appears in a common pattern characterized by dominant flux at high frequencies at the initial rise, flat shape at the maximum phase, and dominant

flux at low frequencies at the decay phase. Such an evolutionary pattern might be indicative of a common dynamical origin for these events. Third, the microwave decay time, in these samples, shows a large variation with frequency as follows: the higher frequency fluxes are as impulsive as hard X-rays, while lower frequency fluxes are as extended as soft X-rays. This provides a challenge to the well-known rule that the time profile of microwaves in general resembles that of hard X-rays and its time-integral reproduces that of soft X-rays (e.g., Neupert, 1968; Tanaka and Zirin, 1985; Dennis and Zarro, 1993).

These new observational properties therefore pose additional problems that must be addressed by the models which were originally constructed to account for the flat spectral shape at the maximum phase. In particular, the fact that this distinctive spectral activity occurs in several large events suggests that the origin of such anomalies should be looked for in the characteristics of big flares. As an effort in this line, we carry out model-calculations of microwave flux under assumptions of nonthermal gyrosynchrotron mechanism and dipole field geometry mainly to deduce source conditions for the observed spectral properties during the flares. We also show that the results of spectral fitting can lead to a qualitative understanding of the unusual frequency-dependent relationship between the microwaves and X-rays in these events. In this way, we hopefully explore the big flare characteristics underlying these large microwave bursts with peculiar spectral properties. The plan of this paper is as follows: In §2, we describe the observations. In §3, we set up our line of approach by a review of previous works that may bear on the explanation of the present observations. In §4, our model calculations are presented and the issues are discussed based on the results. Conclusions are given in §5.

2. Observation

Data we examined are microwave spectra and soft X-ray time profiles of four X-class flares that occurred on 1990 May 24 and 1991 March 7, 8, and 22. Microwave spectra are obtained from the OVRO Solar Array with spectral resolution of 0.2

GHz in the frequency range of 1-18 GHz and time resolution of 10 seconds. The soft X-ray fluxes at 1-8 Å are obtained from the GOES satellite. The flaring time, source location, and maximum fluxes of microwaves and soft X-ray classes of these events are listed in Table 1. It is noted that the four events are all characterized by high flux level at the maximum phase (10^2-10^4 sfu) and long durations of the whole activity (10 minutes to hours). We describe the microwave spectra of these events in §2.1 and their time correlations with X-rays in §2.2.

2.1. MICROWAVE SPECTRA AND THEIR TIME-EVOLUTION

Figure 1 shows the the time-sequence of total power spectra centered at the time of maximum flux of four events. At the maximum phase (the central frames in Figure 1), the spectra appear in a broadband type (Guidice and Castelli, 1975) and similar to those reported by Hachenberg and Wallis (1961). It is noteworthy that two of them show fluxes above 10^4 sfu, which even persist to frequencies as low as 1 GHz. It is one of the largest radio fluxes ever reported at that low frequency (see §1).

Another interesting point in Figure 1 is the characteristic pattern of the spectral evolution which takes three stages: In the initial impulsive rise phase, a spectral peak shows up first at high frequencies and then subsequent enhancement of flux follows up at lower frequencies (the first and the second frames in Figure 1). In the maximum phase, the overall spectra appear in a flat shape (the central frame). In the decay phase, the higher frequency components diminish much faster while lower frequency ones diminish more slowly. As a result, fluxes dominate at low frequencies with negative spectral slope in the extended decay phase and the negative slope is gradually increasing with time (the fourth and the last frames).

Such a change of spectral shape during flares is in a contrast with a more common case of impulsive microwave bursts where the spectra evolves keeping the same shape during flares (Stähli, Gary, and Hurford, 1989, 1990).

2.2. TIME PROFILES OF MICROWAVES AND X-RAYS

In Figure 2, we plot the microwave fluxes at four frequencies (1, 2, 5, and 18 GHz) in upper panels and X-ray fluxes at 1-8 Å in lower panels. As hard X-ray data from HXRBS were unavailable at the times of these events, we take time-derivative of the soft X-ray curves as hypothetical hard X-ray curves in light of the well-known 'Neupert effect' (Neupert 1968; Dennis and Zarro, 1993). The hypothetical hard X-ray curves computed in this way show duration over 1-2 minutes (dotted lines in Figure 2). These values are in a rough agreement with the results of the Phebus experiment on board the GRANAT satellite for the 1990 May 24 event (Talon *et al.*, 1993) and the 1991 March 22 event (C. Barat and O. Terekhov, 1993, private communication).

GOES soft X-ray data are usually given in two wavelength bands to provide information of the electron temperature, T_e, and the emission measure, $\int n_e^2 dV$ (Thomas, Starr, and Crannell, 1985). In the present data, the fluxes at wavelengths 0.5-4Å show saturation near the peak time. If we make interpolation to recover the saturated portion approximately, a rough estimate of these quantities goes as $\int n_e^2 dV \approx 9 \times 10^{50}$ cm^{-3} for the 1990 May 24 event, 8×10^{50} cm^{-3} for the 1991 March 22 event, and 2×10^{50} cm^{-3} for the 1991 March 7 event and $T_e \approx 2 \times 10^7$ K for all these three events; GOES data for the 1991 March 8 event are absent. These results suggest that the events under present investigation belong to the strongest class of soft X-ray activity (cf., Denton and Feldman, 1984).

Comparison of microwave time profiles with those of X-rays yields several points to note: First, the well-known good correlation between microwaves and hard X-rays (e.g., Dennis, 1988) is found only at high frequencies (> 14 GHz). Second, at lower frequencies (< 14 GHz), the microwave flux violates this rule by decaying more slowly. This trend of longer duration at lower frequencies continues down to 1 GHz, the lowest frequency used in the present observation, so that the microwaves at 1 GHz approach closer to that of soft X-rays. Third, the degree of closeness of

microwaves at 1 GHz with soft X-rays is, however, different from event to event. In particular, microwaves at all frequencies decay faster than soft X-rays in the 1990 May 24 event while microwaves below 5 GHz live longer than soft X-rays in the 1991 March 22 event. We also note that microwaves rise impulsively at all frequencies while soft X-rays rise more slowly and peak later as compared to the microwaves in all events. Due to such discrepancies, it is unlikely that the microwaves at lower frequencies share the same origin with soft X-rays although duration times are roughly similar. The general trend for increasing microwave duration toward lower frequencies must, however, be explained.

3. Previous Studies

The above observational properties may be new as a whole. However, the flat spectra and the long-duration activity seen at large bursts have been discussed elsewhere referring to different observations. For the purpose of gathering available information, we review the previous studies here and discuss their relevance to understanding of present data.

3.1. ON THE FLAT SPECTRAL SHAPE

It was Ramaty and Petrosian (1972) who first gave a theoretical interpretation of flat and high microwave flux spectra as observed by Hachenberg and Wallis (1961), in terms of a uniform model. They noted that the free-free emission is not capable of producing the high microwave fluxes as observed ($\sim 10^3$ sfu) and that nonthermal gyrosynchrotron emission is thus the most likely radiation mechanism. In a uniform model, however, the flat spectral shape is hardly reproduced by the gyrosynchrotron mechanism alone so that they worked out a set of conditions for dominance of the free-free opacity relative to the gyrosynchrotron opacity over 2-20 GHz. The resulting conditions include low electron temperature, $T_e < 3 \times 10^6$ K, and weak magnetic field, $B < 180$ G, and a limit for the possible maximum flux as $F_\nu \leq 2 \times 10^3$ sfu.

Klein and Trottet (1984), on the other hand, proposed that source inhomogeneity can lead to flattening of microwave spectra due to nonthermal gyrosynchrotron. Klein, Trottet, and Magun (1986) noted that multiple burst sources can lead to a similar effect. The flattening of optically-thick nonthermal gyrosynchrotron spectra due to source inhomogeneity was noticed earlier by Takakura and Scalise (1970) and Takakura (1972) although no particular observation was referenced. Böhme *et al.* (1977) suggested superposition of multiple sources to produce broadband spectra. In a somewhat different context, Dulk and Dennis (1982) also noted that multi-thermal components will lead to flattening of optically-thick thermal gyrosynchrotron flux spectra.

In our view, a nonuniform model comes closer to explaining the present observation than the uniform model by Ramaty and Petrosian (1972). First of all, in the uniform model, any attempt to raise the flux up to the observed high values using gyrosynchrotron emission is subject to the restriction that free-free opacity must dominate, which limits the brightness temperature. A nonuniform model has no such restriction. Second, according to Ramaty and Petrosian's (1972) results, a large source area above $\sim 10^{-7}$ sterad is likely to be needed to explain the high flux above 10^3 sfu at low frequencies. Extending source area above that large value, still keeping a uniform structure, seems unrealistic in view of the typical physical scale of solar active regions. It is likely that such a big source is inevitably inhomogeneous and the flat spectra are a natural consequence of the source inhomogeneity.

3.2. ON THE LONG-DURATION ACTIVITIES

Another characteristic of our data is the long duration at low frequencies. This recalls several works discussing the underlying physics of extended bursts in contrast to that of impulsive bursts, based on time profiles of microwaves and hard X-rays (Vilmer, Kane, and Trottet, 1982; Kai, Kosugi, and Nitta, 1985; Kosugi, Dennis, and Kai, 1988; Bruggmann *et al.*, 1993). A basic notion brought up by these papers is that a coronal trapping of energetic particles is responsible for the long duration

microwave activity in general. This coronal trap model appears to be useful in explaining the extended microwave activity at lower frequencies if it is combined with the nonuniform magnetic field model. Namely, lower frequency microwaves are emitted from weaker field region near the loop top where particles are trapped and thus survive longer. The high-frequency microwaves are still expected to be short-lived as they are emitted from a stronger field region near footpoints. With a uniform magnetic loop model, we hardly make such a distinction of microwave duration with frequency. That is another benefit of a nonuniform model.

4. Analysis with Model Support

In light of the foregoing discussion, we analyse the observed microwave spectra using a nonuniform magnetic loop model and gyrosynchrotron radiation mechanism. The model is described in §4.1. Using this model, we interpret and analyse the flat and high flux spectra observed at the maximum phase in §4.2. The time-evolution of microwave spectra is analysed in §4.3. The result obtained in §4.3 is used again to give a qualitative interpretation of the correlations of microwaves with X-rays in §4.4.

4.1. MODEL

In the absence of spatial information of the radio emitting region, we tentatively adopt a magnetic loop model as shown in Figure 3. The magnetic fields inside of the loop are assumed to be due to a single dipole lying parallel to the photosphere as in Klein and Trottet's (1984) model (cf., Takakura and Scalise, 1970; Alissandrakis and Prekka-papadema, 1984; Prekka-papadema and Alissandrakis 1988, 1992; Kucera *et al.*, 1993a for other model set-up). Size of the loop is parametrized by the height R and the thickness at the apex, $2\triangle R$. The coronal field distribution is scaled according to B_1 and B_2 which are the field strength at the middle of the loop apex and that at the coronal base, respectively (see Figure 3). We set $B_2 = 1500$ G in this study.

The model dipole loop set up in the reference frame (x_o, y_o, z_o) is rotated by heliographic angles (θ, ϕ) so that the distribution of field strengths and viewing angles can be determined in the observer's frame (x, y, z). At each point (x, y, z) inside the loop, we calculate the emissivity j_ν and the opacity τ_ν due to gyrosynchrotron radiation using the simplified expressions by Dulk and Marsh (1982), and perform the line-of-sight ($\hat{z}$ in Figure 3) integration of the radiative transfer equation to get the distribution of the brightness temperature, T_B, on the projected sky plane (x, y) as

$$T_{B,\nu}(x,y) = \frac{c^2}{k\nu^2} \int_0^\infty j_\nu e^{-\tau_\nu} dz.$$

where k is the Boltzmann constant and c is the speed of light. From the brightness distribution, $T_{B,\nu}(x, y)$, we calculate effective source area and total flux:

$$\Omega_{eff}(\nu) = \frac{\int T_{B,\nu}(x,y) dx dy}{T_{B,\nu}^{max}} \quad \text{and} \quad F_\nu = k T_{B,\nu}^{max} \left(\frac{\nu}{c}\right)^2 \Omega_{eff}(\nu)$$

as a function of frequency where $T_{B,\nu}^{max}$ is the maximum value of $T_{B,\nu}(x, y)$.

In the present model-computation, we mainly control (i) the size of the loop, R and $\triangle R$, and the field strength at the loop top, B_1, all of which determine the degree of magnetic field inhomogeneity and (ii) the power-law index of electrons, δ, which defines hardness of the electron energy distribution. For simplicity, we assume that the nonthermal electrons are uniformly distributed inside the loop.

4.2. FLAT SPECTRAL SHAPE AND MAXIMUM FLUX

The goal here is to investigate under which source condition the observed flat and high-flux spectra are reproduced. As a first step, we check the issue of thermal/ nonthermal origin of these events and also the uniform/nonuniform sources. We

show the results in Figure 4. Upper panels in Figure 4 show two-dimensional display of $T_{B,\nu}$ for nonthermal (Figure 4a) and thermal (Figure 4b) gyrosynchrotron emission from a nonuniform magnetic loop and the nonthermal gyrosynchrotron from a uniform loop (Figure 4c) mainly to contrast the source areas at two different frequencies. In the lower panel, we show the spectra of maximum brightness temperatures (Figure 4d), effective source area (Figure 4e), and the total flux (Figure 4f); model parameters used in the calculation are listed below the figure. It is known from previous works that under certain circumstances the whole loop is bright at lower frequencies while only the foot-points are bright at high frequencies (e.g., Klein and Trottet, 1984; Alissandrakis and Prekka-papadema, 1984; Alissandrakis, 1986; Prekka-papadema and Alissandrakis, 1988, 1992). This tendency is particularly prominent in the present models (Figure 4a and 4b) where the field strengths at the loop top and footpoints make a big contrast ($B_1/B_2 \sim 1/300$). The uniform model (Figure 4c), however, does not share this property so that Ω_{eff} changes little with frequency (Figure 4e). As a result, total flux spectrum follows closely the Rayleigh-Jeans law: $F_\nu \propto \nu^2$ (Figure 4f). In nonuniform models, the effective source size increases towards lower frequencies (Figure 4e) and it tends to make the resulting flux spectra flatter than the ν^2-slope (Figure 4f).

With the frequency-dependence of source size alone, however, an essentially flat flux spectrum cannot be achieved; we thus need an increase of $T_B(\nu)$ towards lower frequencies as well. Figure 4d shows that the increase of $T_B(\nu)$ at lower frequencies can happen for nonthermal gyrosynchrotron radiation. To understand the increase of $T_B(\nu)$ at lower frequencies, we recall the fact that for nonthermal particles, the effective temperature depends on magnetic fields and power-law index as $T_{eff} \equiv (c^2/k\nu^2)(\eta_\nu/\kappa_\nu) \propto (\nu/\nu_B)^{.5+.085\delta}$ (Dulk and Marsh, 1982) where ν_B ($\equiv 2.8B$ MHz) is the gyrofrequency. Therefore, T_{eff}, which corresponds to the optically-thick brightness temperature, can be made higher toward lower frequencies if the effective source region moves to weaker field regions at lower frequencies to increase (ν/ν_B). Figure 4a shows that this is the case for nonthermal gyrosynchrotron emission from a nonuniform magnetic loop. In case of a thermal model,

T_{eff} is equivalent to the electron temperature T_e independent of frequency and therefore a thermal model is inadequate in producing the flat and high-flux spectra as we observed. To conclude, only nonthermal gyrosynchrotron emission from an inhomogeneous source can explain the spectral characteristics we observe.

We now examine the influence of various source parameters upon the resulting flux spectra using only the nonthermal gyrosynchrotron source. Figure 5a shows flux spectra calculated with three different values of field strength at the loop top, B_1; flux spectra become flatter as B_1 decreases and thus makes bigger contrast with the field strength at the base of the loop. Figure 5b (bottom panel) shows flux variation with loop size; in order to raise the amount of flux up to 10^4 sfu, we need a gigantic loop with $R \sim 300''$, which will then result in a radio source of size $\sim 7 \times 10^{-7}$ sterad at 1 GHz. We note that a large microwave burst with a size comparable to the above values has been reported by Kucera *et al.* (1993b). Results shown in Figure 5a and 5b give an estimate for the field strength and source size required to reproduce the observed flux spectra (Figure 1). Figure 5c shows dependence of spectra on the loop location on the solar disk. For a fixed heliolatitude ($\phi = 25^\circ$), we try three heliolongitudes, $\theta = 0^\circ$, 30°, and 70°, to find that the resulting spectra are insensitive to heliographic location. This result disagrees with previous results (e.g., Takakura and Scalise, 1970) which show a limb increase of gyrosynchrotron flux. We note that such a directivity results when the particles are assumed to be concentrated at a lower coronal region where the field strength is relatively high and the field directions are better organized. This is not the case in our model, where the microwave flux mostly comes from the loop top which is so highly inflated that the field distribution as a whole loses directivity. Our result of the insensitive dependence of flux shape upon the heliographic position is in agreement with the observation (see Table 1 for the source location). Finally, we check the dependence of flux on the hardness of radiating particles in Figure 5d. The result shows that a relatively hard electron distribution ($\delta \sim 3$) is essential to produce the high level of flux as observed ($F_\nu \sim 10^4$ sfu) in addition to the big size ($R \sim 300''$) and a large degree of source inhomogeneity ($B_1/B_2 \sim 1/300$).

Based on the results presented in Figure 5, we determine sets of source parameters that best reproduce the observed spectra at the maximum phase (Figure 1); results are listed in Table 2 (columns 2 - 6). Taking a weaker field strength at the loop top (5-10 G) is essential to reproduce the flat flux spectra as observed in all events. Hard nonthermal electrons ($\delta = 3$) and a large source size ($R = 300''$) are required to raise the overall fluxes to those of two strongest events (the 1990 May 24 and 1991 March 22 flares). For weaker events (the 1991 March 8 and 1991 March 7 flares), relatively softer electrons ($\delta = 3.5$) and smaller source sizes ($R = 180''$-$240''$) are adequate. Total number of nonthermal electrons above 10 keV is calculated for each event by integrating the electron density over the whole loop volume. The resulting values, $N(E \geq 10 \text{ keV}) \sim 10^{36}$ - 10^{38}, far exceed commonly reported values of normal flares but are comparable to the previous result by Ramaty and Petrosian (1972) for the flat spectra observed by Hachenberg and Wallis (1962), which are similar to that of the 1991 March 8 event.

4.3. TIME-EVOLUTION OF MICROWAVE FLUX SPECTRA

Another interesting property of these microwave bursts is the time-evolution of the microwave spectra. In the present study, we investigate a hypothesis that a time-dependent change of source position within a nonuniform magnetic loop can lead to such a time behavior, in light of the sensitive dependence of gyrosynchrotron spectra on magnetic fields. We here describe our procedure mainly referring to the spectra from the 1991 March 22 flare. In Figure 6, we make a model-fit to the observed spectra at five instances: t_1 (22:43:20 UT), t_2 (22:43:50 UT), t_3 (22:44:10 UT), t_4 (22:55:00 UT), and t_5 (23:30:020UT) in the 1991 March 22 event.

We first consider the spectra in the rise phase of the 1991 March 22 event. The spectra at this period show flux concentrated at high frequencies, implying that radiation comes from a relatively stronger and more uniform field region. Since there is no good reason that nonthermal electrons should be confined only to a stronger field region in our loop geometry, such a spectrum is hardly reproduced if

we keep the same source size R and the same field strength B_1 as we assumed to match the maximum phase spectra. As a plausible model, we assume that the loop was initially of a smaller size, but expands to a size of $R \sim 300''$ at the maximum phase. We thus make a fit to the observation by using $R = 40''$ and $\triangle R/R = 0.1$ at t_1 and $R = 200''$ and $\triangle R/R = 0.2$ at t_2; the magnetic field strengths scale according to loop height R as $B_1(t_{1,2}) \approx B_1(t_3)[R(t_3)/R(t_{1,2})]^2$ (Figure 6a). On the other hand, the change of δ has little influence on the shape of spectra which are optically thick in the frequencies under investigation. Therefore, it is most likely that the spectral variation in the rise phase is due to the change of loop size, $R(t)$, or the corresponding change of $\Omega_{eff}(\nu)$ rather than that of $T_B(\nu)$. In this case, the delayed rise of lower frequency fluxes relative to high frequency ones should be interpreted as due to the finite time taken for the structural change of the loop, which is about 1-2 minutes (cf. the time variations of $\Omega_{eff}(\nu)$ and $T_B(\nu)$ in Figure 6a).

The maximum phase is reached when the loop is expanded to the size $\sim 300''$ as demanded to explain the observed flat and high-flux spectra as we worked out in §4.2 (curves denoted as t_3 in Figure 6a and 6b).

Figure 6b shows model-fits made to the decay-phase spectra. The spectral variation in this period is characterized by a gradual increase of the negative spectral slope of the spectra. A change of loop size cannot produce this effect because reducing loop size will lead to a positive spectral slope, and extending the loop size further seems too unrealistic. Required here would be a gradual decrease of average field strength in the source. We, therefore, consider the coronal trap model (see §3.2) with the assumption that a whole volume of nonthermal electrons is gradually shrinking to the loop top where fields are weakest. This, together with a softening of the electron power-law distribution ($\delta(t_4) = 3.5$ and $\delta(t_5) = 4.0$), leads to a good fit to the spectra, with a negative spectral slope. The shrinking of the microwave source to the loop top lowers the turnover frequency of gyrosynchrotron spectra and the electron softening makes the spectral slope above the turnover frequency more

steep. The former is conceivable in a case where the net survival time of high-energy electrons increases at a higher part of the loop due to decreasing Coulomb loss with height.

A common trend in the rise phase and the decay phase is that the effective source area, Ω_{eff}, becomes more independent of frequency as we go away from the maximum phase (Figure 6). This means that the source in both the earlier rise and the later decay phase is smaller and more uniform. In contrast, the source at the maximum phase is highly inflated and the degree of magnetic field inhomogeneity is greatly enhanced, which leads to the increase of Ω_{eff} toward lower frequencies and thus the flux spectra become flat. The basic difference between the spectral evolution at the rise and that at the decay phase can be learned from Figure 6. The initial evolution of microwave spectra is mainly due to the change of $\Omega_{eff}(\nu)$ associated with the loop dynamics, while the later evolution is mainly due to the change of $T_B(\nu)$ associated with the softening of nonthermal electrons.

Of many quantities involved with this model-fit, the most interesting one would be the time scale for the change of electron power-law index, δ, in the particle evolution during the decay phase. We define a quantity, τ_δ, as the time taken for δ to increase by unity, and determine τ_δ by comparing the microwave spectra calculated with δ and $\delta+1$ with the observed spectra. The results come out as $\tau_\delta \approx$ 3.3 - 46 minutes depending on events (see the last column of Table 2). A trend is not quite obvious with these four events alone except that τ_δ is larger in a stronger event in general. It is, however, certain that τ_δ is longer in the 1990 May 24 event than in the 1991 March 22 event, although the whole microwave activity is longer in the 1991 March 22 event. This might imply that the particle loss is involved with some internal dynamics which differs from event to event. According to our model scenario of these two big events, what is required is the preferential loss of higher-energy electrons over a time scale longer than 40 minutes in a inflated coronal trap where the fields are relatively weaker and the density of thermal particles is low. Coulomb loss may not be an adequate answer because the Coulomb loss is

more efficient for lower-energy electrons and in denser medium. The radiative loss in the coronal trap would be too slow due to weaker field strength. The escape of high-energy electrons as a result of scattering by plasma turbulence could be a good candidate and the betatron loss (Bruggman *et al.*, 1993) could be another.

4.4. CORRELATIONS WITH X-RAYS

In these events, microwaves at low frequencies are unusually extended in time and thus look similar to soft X-rays, although a good correlation with hard X-rays is still found at higher frequencies above 14 GHz. Such a time behavior might suggest a thermal origin for the low-frequency microwaves, in contradiction with our conclusion of the nonthermal origin for the microwaves based on the spectral fitting (§4.2 - §4.3).

We have already mentioned in §2.2 that there are a few observational discrepancies that preclude this possibility. Another point gathered after model-analysis is that the observed huge amount of radio flux cannot be produced by thermal gyrosynchrotron or by thermal free-free emission from soft X-ray particles with electron temperature at most 2×10^7 K, although their emission measure is impressively high ($\int n_e^2 dV \sim 10^{51}$ cm^{-3}).

Therefore, the question should shift from the thermal/nonthermal origin of the radiating particles to how the impulsive and extended components can coexist in an event and how such a frequency-dependence can result if both are of nonthermal origin. We believe that the key lies again in the influence of the field inhomogeneity upon the evolution of microwaves at different frequencies, along with the coronal trap's gradual shrinking to a weaker field region (i.e., the loop top). We thus propose, based on the model fit made in previous section, the following scenario:

(i) The whole microwave burst starts with an initial injection of nonthermal electrons at the loop top, which impulsively raises the fluxes at all frequencies. The duration of this injection should be no longer than that of high frequency

(> 14 GHz) microwaves and hard X-rays which are as short as 1-2 minutes. Otherwise, longer microwave activity must have been seen at high frequencies as well as at the lower frequencies.

(ii) After the impulsive injection ceases, the evolution of microwaves is under the influence of the ambient medium which controls cooling efficiency of microwave-emitting electrons depending on the position within a loop. The electrons reaching footpoints will quickly die out due to the Coulomb loss efficient there. Since the Coulomb loss time is much shorter than the inferred injection time, the resulting radiation time profile is largely determined according to that of injection, which is over 1-2 minutes. This will be the case of high-frequency microwaves and perhaps the hard X-rays which occur in the stronger field region near footpoints. On the other hand, the lower frequency microwaves can persist until the flare activity in the coronal trap becomes entirely extinct, as they are emitted from the weaker field region near the loop top. The regular trend of longer microwave duration toward lower frequencies is then due to the gradual shrinking of the source region to the loop top.

The next concern would be whether the longer lifetime of low-frequency microwaves is entirely due to the cooling condition or partly due to continued acceleration, perhaps by interaction with plasma turbulence that builds up later. This important problem can properly be handled if a kinetic approach is used in combination with macroscopic dynamics of the loop (e.g., Bruggman *et al.*, 1993). This is beyond the scope of this paper in which the analysis is limited to spectral fitting at individual instances. However, the time scale, τ_δ, deduced from the present spectral fit may provide a piece of information useful in the detailed study of particle evolution.

5. Conclusions and Discussions

In this paper, we reported four microwave burst events which are characterized by flat and high flux spectra and a long duration (§2). We reviewed previous works

on the flat spectra and those on the long-duration microwave activity to get a qualitative understanding of these events as a whole (§3). Based on these works, we attempted a quantitative analysis of the microwave spectra in terms of nonthermal gyrosynchrotron radiation from nonuniform, dipole magnetic loops (§4). Our results are summarized as follows:

First, the flux spectra at the maximum phase appear as flat with fluxes ranging from 10^2 sfu to 10^4 sfu (Figure 1). As a first step to understanding this peculiar spectral behavior, we investigated how source inhomogeneity can lead to a flattening of gyrosynchrotron flux spectra in spite of increasing self-absorption at low frequencies. It is noted that the effective temperature of nonthermal particles can be made higher toward lower frequencies depending on source inhomogeneity. This property, together with increasing effective source area toward lower frequencies, tends to give flat flux spectra. Neither a thermal nor a uniform model share this radiative property and, therefore, they are excluded from the candidates (Figure 3). As specific results, we found that a flat microwave spectrum with 10^2-10^4 sfu may occur in a case where a magnetic loop is extended to an angular size of $\sim$ (0.7-7)$\times 10^{-7}$ sterad and contains a huge amount $N(E > 10\mathrm{keV}) \sim 10^{36}$ - 10^{38} of highly energetic particles with $\delta \sim$ 3-3.5 distributed over the entire loop, spanning a wide range of magnetic fields from 1500 G down to a few G (see Table 2). These results based on spectral fitting are in support of previous works of other extended events based on the analysis of time profiles. As examples, the tendency for a harder electron population trapped in a weaker field region has been noted by Takakura, Uchida and Kai (1968) and Kosugi, Dennis, and Kai (1988). The abundant number of relativistic electrons trapped in large magnetic loops have been noted in Vilmer, Kane, and Trottet, (1982) and Kai, Kosugi, and Nitta (1985). Therefore, the nonuniform magnetic fields and abundant hard electrons trapped in the corona are perhaps the most fundamental factors for producing these large extended microwave bursts.

Second, a common pattern of spectral evolution is seen in these four events. We attempted to deduce the scenario underlying the spectral variation based on

a model fit to instantaneous spectra by varying the loop size and power-law index of nonthermal electrons. In our results, the loop was initially of a smaller size and had a more uniform field distribution to emit radiation flux dominant at high frequency until it soon expanded to a big size to emit the flat, high-flux spectrum at the maximum phase. The spectral change at the decay phase is reproduced by assuming confinement of the source region to a smaller one at the loop top and gradual softening of electron power-law. The former can happen in a case where the particle loss by Coulomb interaction decreases with height; the latter may be due to either escape of high-energy electrons or radiative energy loss. We note that the picture drawn here is in good agreement with some classical models of the type IVμ event (a long-lasting and broadband radio microwave emission) in general. Böhme *et al.* (1976) attempted to reproduce type IVμ spectra in terms of the 'core-halo model.' Our results qualitatively agree with their model in that we locate the short-lived high-frequency components at stronger fields near foot-points (core) and the long-lived low-frequency ones at weaker fields near loop-top (halo). Šveska (1976, p192) commented that the low-frequency radio fluxes may be due to magnetic field modulation of trapped particles while the high-frequency fluxes represent direct acceleration, referring to the type IVμ burst during the 1966 July 7 event (Enomé, 1969). Our model assumption of the time-varying coronal trap may provide a physical interpretation of the term 'magnetic modulation' that he used.

Third, our multi-frequency observation uncovers that these microwave bursts have both the impulsive and the extended components, which thus look similar to the hard X-rays and the soft X-rays, respectively. We showed that the coronal trap model can be made to fit this observation if properly combined with a nonuniform magnetic loop model. In this way, it is concluded that the gradual shrinking of the region of energetic electrons is responsible for the increasing microwave duration toward lower frequencies. However, it is yet to be checked whether the extended life is solely due to the cooling condition or partly requires additional injection or acceleration in a limited region of the magnetic loop. In the latter case, the detailed

mechanism for subsequent acceleration (e.g., by shock waves) may deserve future study.

Finally, we wish to stress the distinction of these large extended events with the so-called 'gradual rise-and-fall' bursts. These two types of bursts sound similar in that both show long-duration activity and broadband spectra. The distinction can, however, be made in many ways: First of all, the gradual rise-and-fall components refer to weak events ($F(\nu > 1$ GHz$) < 40$ sfu) according to Švestka (1976, p140). The flux limit cited above is largely due to the presumed radiation mechanism which is the thermal free-free emission from soft X-ray particles (Shimabukuro, 1972; Hudson and Oki, 1972). In contrast, extended bursts seen at large flares accompany high fluxes ($F(\nu > 1$ GHz$) \geq 10^2$ sfu) which is thus most likely due to nonthermal gyrosynchrotron emission as we worked out in this paper (§4.2). Another important difference is that the *weak* gradual bursts (or postbursts) show gradual rise while the *large* extended bursts like those presented here show impulsive rise although decay curves are extended. The gradual rise microwave flux as slow as soft X-rays implies that the *weak* gradual bursts are due to the thermal response of the ambient plasma to the heating by nonthermal particles. In contrast, the impulsive rise seen in *large* extended bursts will indicate that the microwave flux at all frequencies are directly from a nonthermal injection. Due to such a difference in underlying physics, the extended bursts seen at large flares should not be regarded as just the high-energy version of weak gradual events.

Acknowledgements

We thank Dr. A. Krüger and Dr. N. Vilmer for helpful discussions. We also thank Dr. C. Barat and Dr. O. Terekhov for the information of Phebus data and Ms. Kim Tolbert for providing the GOES data. Observation at OVRO was funded by NSF grants ATM-9013173 and AST-8919770 to the California Institute of Technology. One of us (JWL) has been supported by NASA grant NAGW-3005 and NAGW-1972 during preparation of this paper.

References

Alissandrakis, C. E.: 1986, *Solar Phys.* **104**, 207.

Alissandrakis, C. E. and Preka-Papadema, P.: 1984, *Astron. and Astrophys.* **139**, 507.

Böhme, A., Fürstenberg, F., Hildebrandt, J., Hoyng, P., Krüger, A., Saal, O., and Stevens, G. A.: 1976, HHI-STP-Report No. 6 Astronomical Institute Utrecht.

Böhme, A., Fürstenberg, F., Hildebrandt, J., Saal, O., Krüger, A., Hoyng, P., and Stevens, G. A.: 1977, *Solar Phys.* **53**, 139.

Bruggmann, G., Vilmer, N., Klein, K.-L., and Kane, S. R.: 1993, *Solar Phys.* in press.

Croom, D. L. and Powell, R. J.: 1971, *Solar Phys.* **20**, 136.

Dennis, B. R.: 1988, *Solar Phys.* **118**, 49.

Dennis, B. R. and Zarro, D. M.: 1993, *Solar Phys.* **146**, 177.

Denton, R. E. and Feldman, U.: 1984, *Astrophys. J.* **286**, 359.

Dulk, G. A. and Dennis, B. R.: 1982, *Astrophys. J.* **260**, 875.

Dulk, G. A. and Marsh, K. A.: 1982, *Astrophys. J.* **225**, 350.

Enomé, S.: 1969, *Annals IQSY* **3**, 186.

Guidice, D. A. and Castelli, J. P.: 1975, *Solar Phys.* **44**, 155.

Hachenberg, O. and Wallis, G.: 1961, *Z. Astrophys.* **52**, 42.

Hudson, H. S. and Ohki, K.: 1972, *Solar Phys.* **23**, 155.

Kai, K., Kosugi, T., and Nitta, N.: 1985, *Publ. Astron. Soc. Japan* **37**, 105.

Klein, K. -L. and Trottet, G.: 1984, *Astron. Astrophys.* **141**, 67.

Klein, K. -L., Trottet, G., and Magun A.: 1986, *Solar Phys.* **104**, 243.

Kosugi, T., Dennis, B. R., and Kai, K.: 1988, *Astrophys. J.* **324**, 1118.

Kucera, T. A., Dulk, G. A., Kiplinger, A. L., Winglee, R. M., Bastian, T. S., and Graeter, M.: 1993a, *Astrophys. J.* **412**, 853.

Kucera, T. A., Dulk, G. A., Gary, D. E., Winglee, R. M., and Bastian, T. S.: 1993b, in preparation.

Neupert, W. M.: 1968, *Atrophys. J.* **153**, L59.

Preka-Papadema, P. and Alissandrakis, C. E.: 1988, *Astron. and Astrophys.* **191**, 365.

Preka-Papadema, P. and Alissandrakis, C. E.: 1992, *Astron. and Astrophys.* **257**, 307.

Ramaty, R. and Petrosian, V.: 1972, *Astrophys. J.* **178**, 241.

Shimabukuro, F. I.: 1972, *Solar Phys.* **23**, 169.

Stäli, M., Gary, D. E., and Hurford, G. J.: 1989, *Solar Phys.* **120**, 351.

Stäli, M., Gary, D. E., and Hurford, G. J.: 1990, *Solar Phys.* **125**, 343.

Švestka, Z.: 1976, *Solar flares*, D. Reidel Publishing Co., Boston.

Takakura, T.: 1972, *Solar Phys.* **26**, 151.

Takakura, T. and Scalise, E.: 1970, *Solar Phys.* **11**, 434.

Takakura, T., Uchida, Y., and Kai, K.: 1968, *Solar Phys.* **4**, 45.

Talon, R., Trottet, G., Vilmer, N., Barat, C., and Dezalay, J.-P.: 1993, *Solar Phys.* in press.

Tanaka, K.: 1969, *Solar Terrestrial Activity Chart, Jan.-June, 1969.*

Tanaka, K. and Zirin, H.: 1985, *Astrophys. J.* **299**, 1036.

Thomas, R. J., Starr, R., and Crannell, C. J.: 1985, *Solar Phys.* **95**, 323.

Vilmer, N., Kane, S. R., and Trottet, G.: 1982, *Astron. and Astrophys.* **108**, 306.

Table 1: Observational Data

Date	Region	Location	Peak Time	Duration	Maximum Flux	SX-class
1990/05/24	AR6063	N31W66	20:48:07	$\sim$ 40 min	1.4×10^4 sfu	X9.3
1990/03/07	AR6538	S21E67	23:17:46	9.5 min	1.7×10^2 sfu	X2.5
1990/03/08	AR6538	S25E50	20:27:16	36 min	2.0×10^3 sfu	X1.7
1990/03/22	AR6555	S27E27	22:44:12	$>$ 80 min	1.4×10^4 sfu	X9.4

Table 2: Derived Model Parameters

Event	B_1 [G]	R [']	$\Omega_{1\mathrm{GHz}}$ [sterad]	$N(E \geq 10\mathrm{keV})$	δ	τ_δ [min]
1990/05/24	5	300	7×10^{-7}	3×10^{38}	3.0	≥ 40
1991/03/07	10	180	7×10^{-8}	7×10^{35}	3.5	~ 3.3
1991/03/08	10	240	3×10^{-7}	1×10^{37}	3.5	~ 6.8
1991/03/22	5	300	7×10^{-7}	3×10^{38}	3.0	~ 46

Figure Captions

Fig. 1. Time-sequence of the observed total power spectra in four events as listed in Table 1. The frames in each event are centered on the time of maximum phase.

Fig. 2. Comparison of microwave time profile with X-ray light curves. Upper panels: microwaves at four selected frequencies in 1-18 GHz. Lower panels: soft X-ray light curves at 1-8Å from GOES (solid lines) and their time-derivatives taken as hypothetical hard X-ray curves (dotted lines).

Fig. 3. A model configuration of a dipole loop as seen by an observer at (θ, ϕ). (x_o, y_o, z_o) is the reference frame of the loop and (x, y, z) is the observer's frame with $\hat{z}$ along the line of sight. R and $\triangle R$ are the height and the thickness of the loop at the apex, respectively; B_1 and B_2 represent the field strength at the middle of loop apex and that at the coronal base, respectively.

Fig. 4. Upper panels: model-calculation of the Brightness Temperature distribution for (a) nonthermal gyrosynchrotron, (b) thermal gyrosynchrotron radiation from a nonuniform source, and (c) nonthermal gyrosynchrotron from a uniform source. Lower panels: calculated spectra of (d) the Brightness Temperature, (e) effective source area, and (f) total flux for the above three cases: case (a) - solid lines, case (b) - dashed lines, and case (c) - dotted lines.

Fig. 5. Calculated spectra of the Brightness Temperature, source area, and total flux: their variations with (a) magnetic field strength at the loop top, B_1 (b) loop size, R, (c) heliolongitude, θ, and (d) power-law index, δ, of nonthermal electrons.

Fig. 6. A model fit to the observed spectral variation in the 1991 March 22 event at (a) rise phase and (b) decay phase. t_1 - t_5 respectively refer to 22:43:20 UT, 22:43:50 UT, 22:44:10 UT, 22:55:00 UT, and 23:30:00 UT on 1991 March 22.

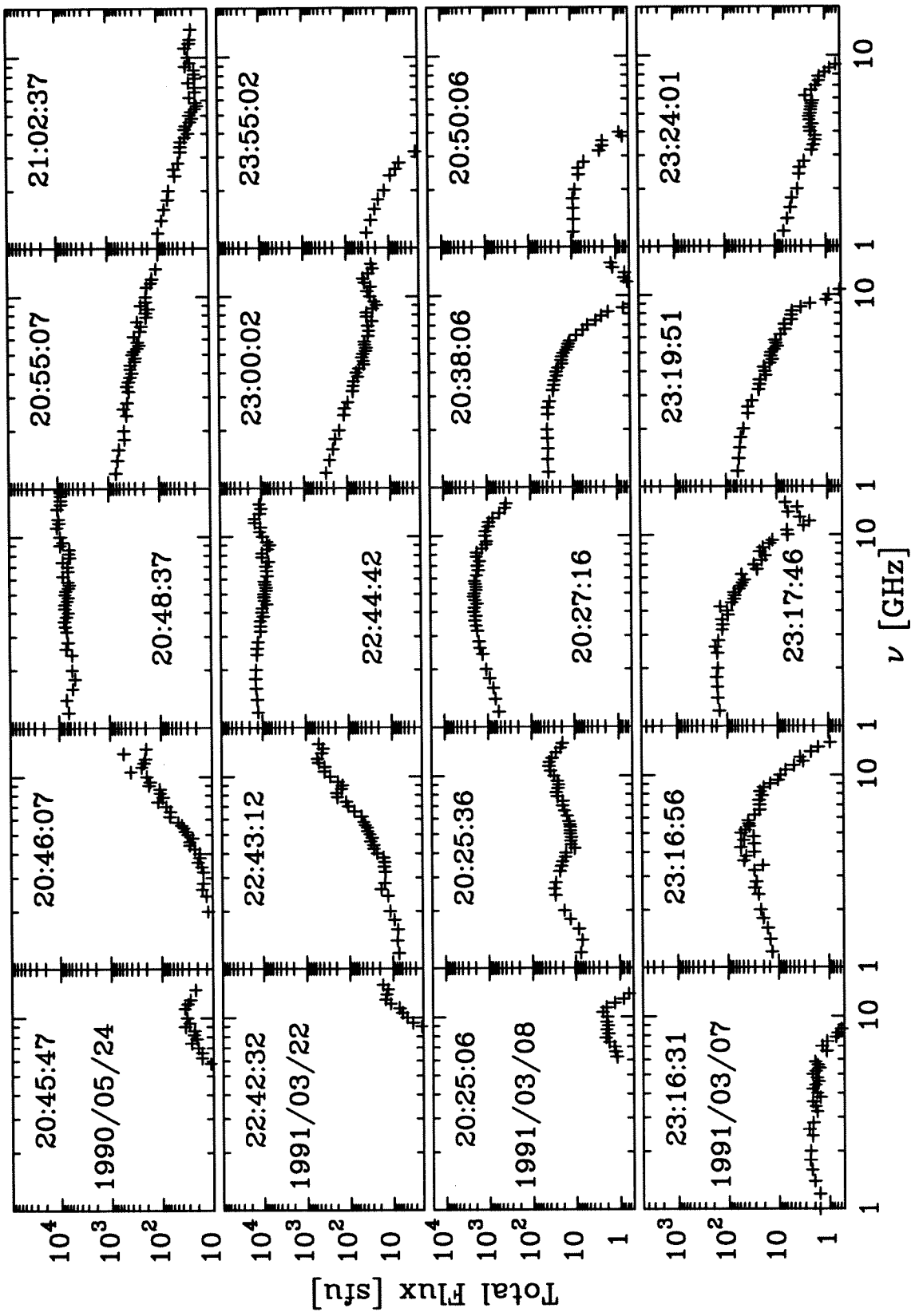
20:45:47
20:46:07
20:48:37
20:55:07
21:02:37
1990/05/24
22:42:32
22:43:12
22:44:42
23:00:02
23:55:02
1991/03/22
20:25:06
20:25:36
20:27:16
20:38:06
20:50:06
1991/03/08
23:16:31
23:16:56
23:17:46
23:19:51
23:24:01
1991/03/07
Total Flux [sfu]
ν [GHz]

Figure 1

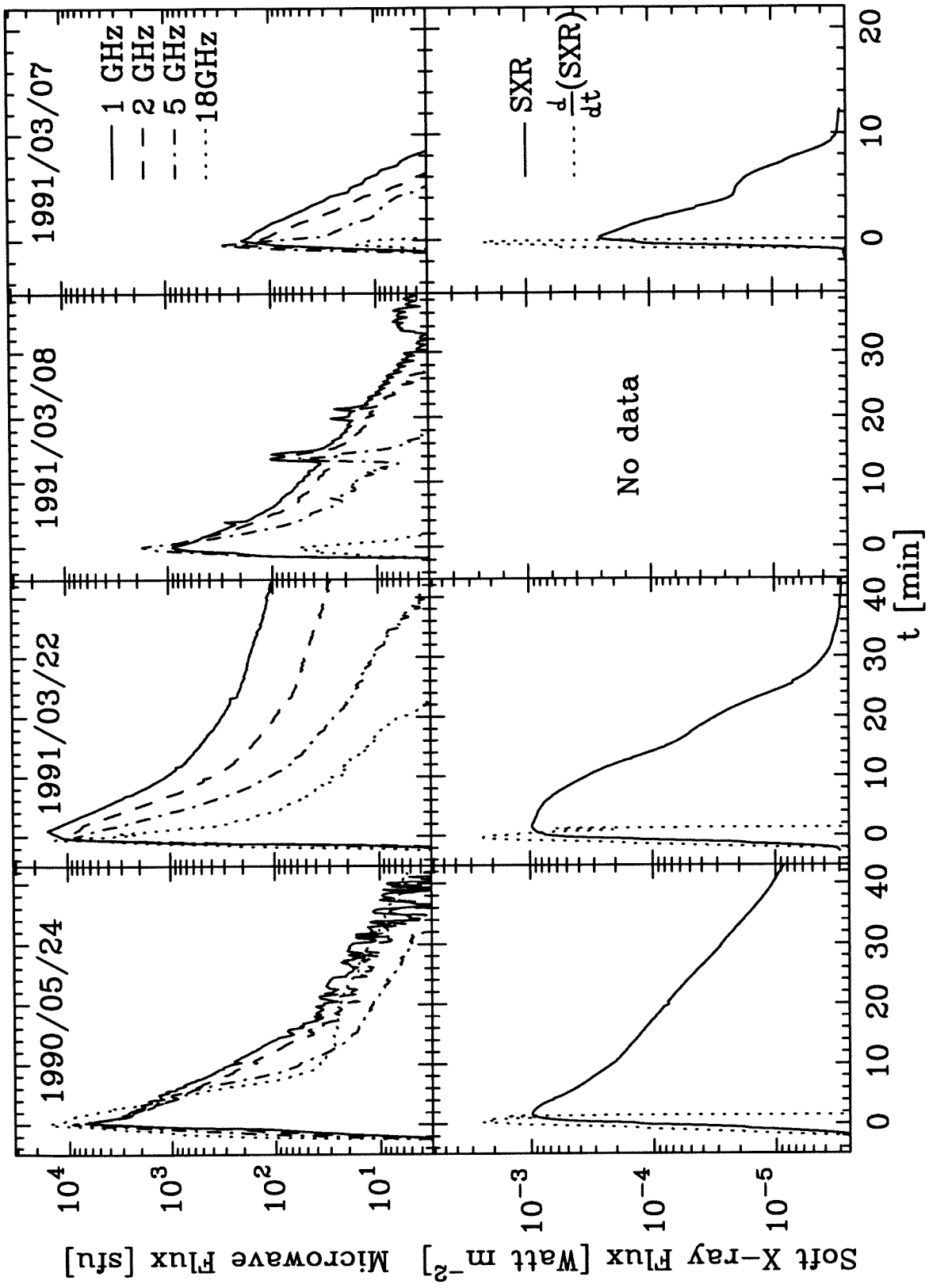
1991/03/07
1 GHz
2 GHz
5 GHz
18GHz
SXR
$\frac{d}{dt}$(SXR)
1991/03/08
No data
1991/03/22
1990/05/24
0 10 20 30 40 0 10 20 30 40 0 10 20 30 0 10 20
t [min]
10^4 10^3 10^2 10^1
10^{-3} 10^{-4} 10^{-5}
Microwave Flux [sfu]
Soft X-ray Flux [Watt m^{-2}]

Figure 2

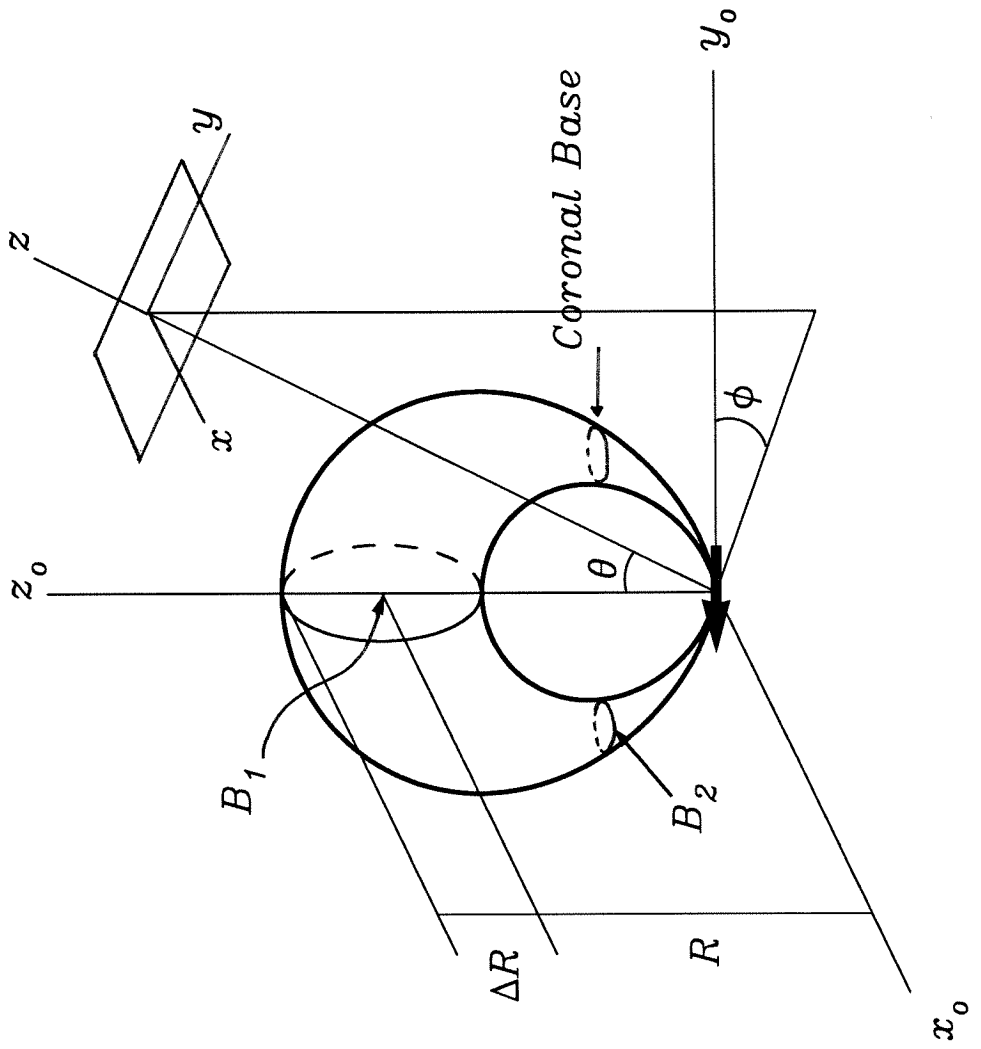

Figure 3

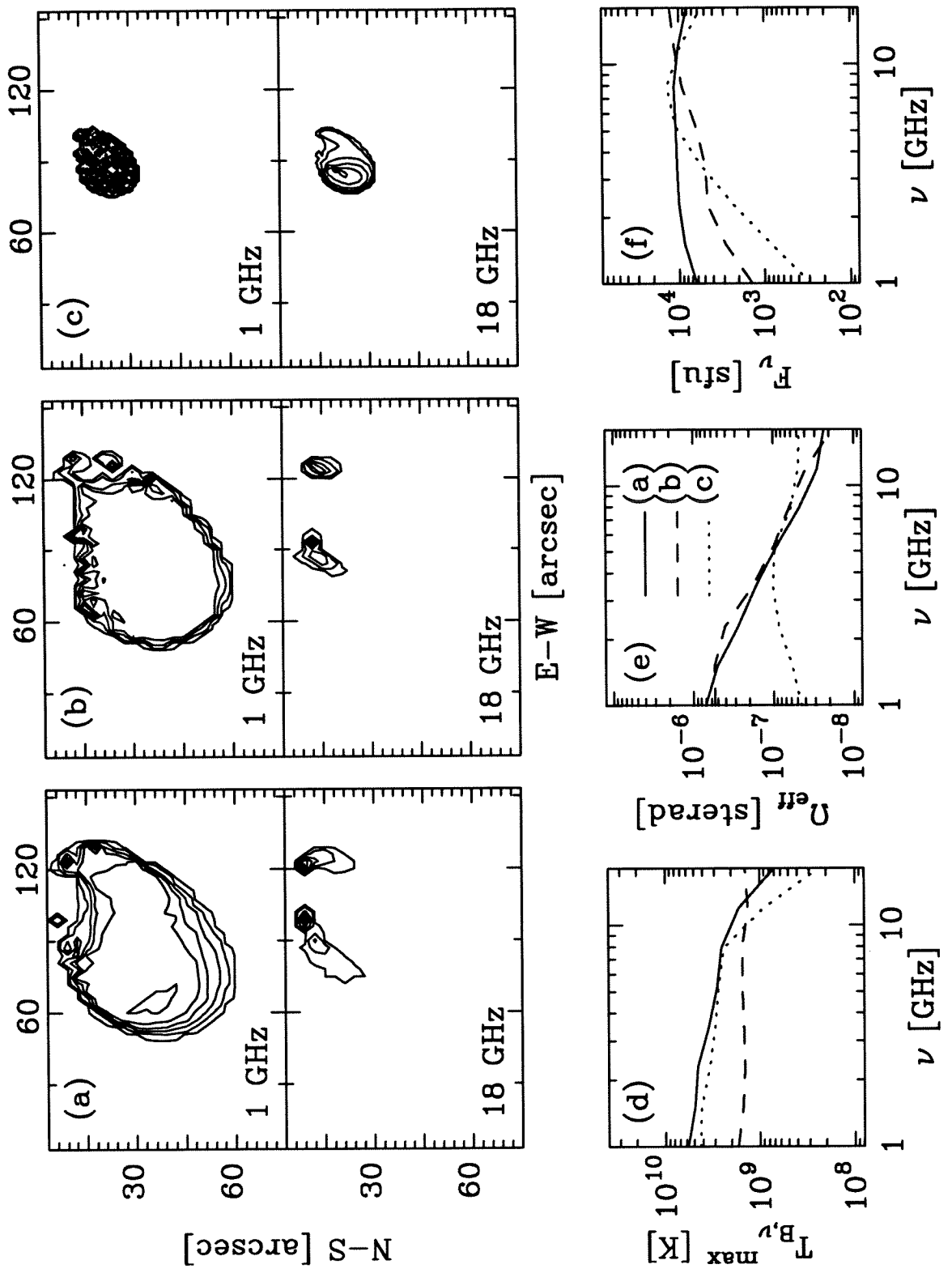
(a)
(b)
(c)
(d)
(e)
(f)
1 GHz
18 GHz
120
60
30
60
N–S [arcsec]
E–W [arcsec]
$T_{B,\nu}{}^{max}$ [K]
Ω_{eff} [sterad]
F_ν [sfu]
ν [GHz]
10
1
10^{10}
10^9
10^8
10^{-6}
10^{-7}
10^{-8}
10^4
10^3
10^2
a
b
c

Figure 4

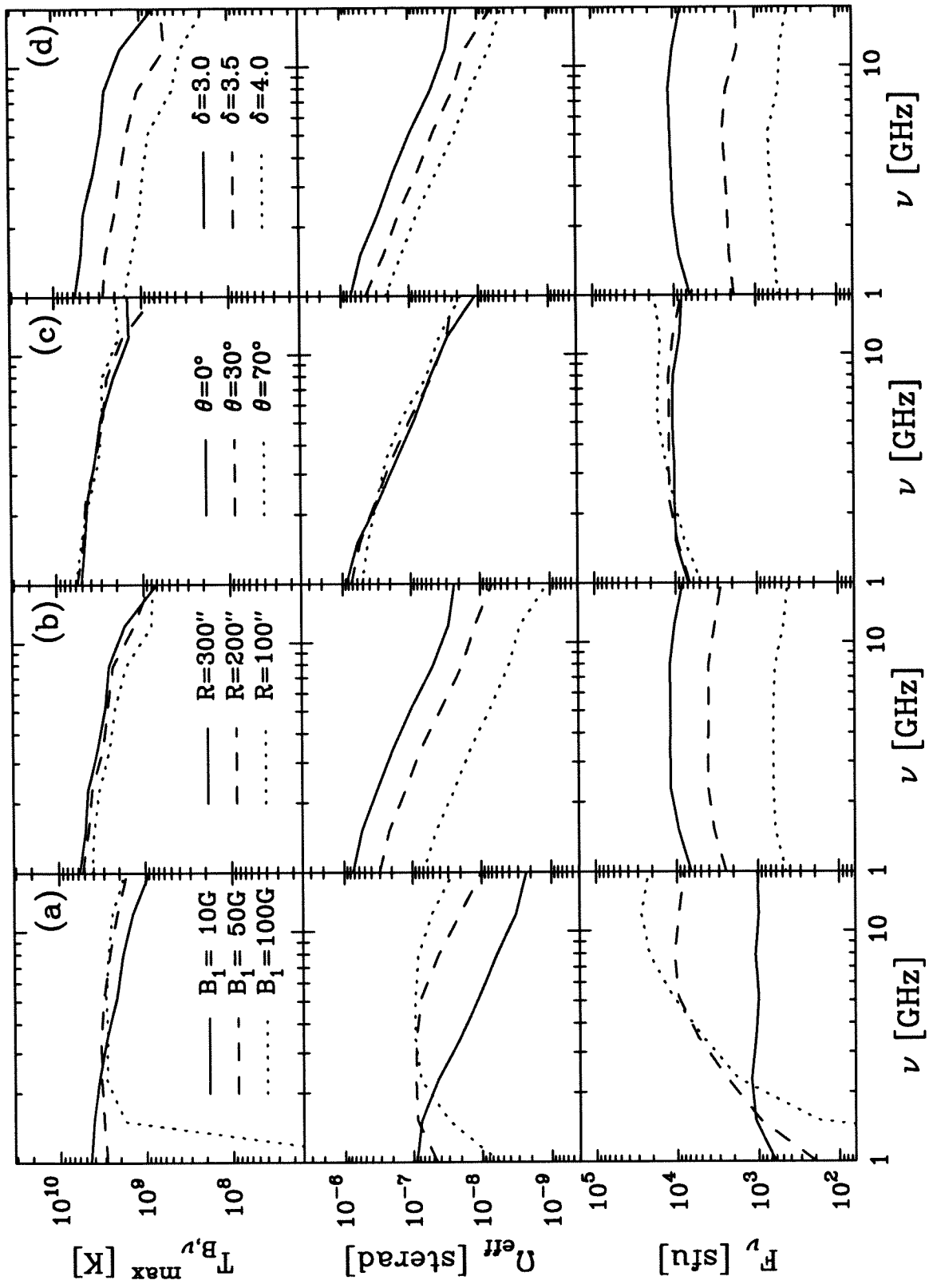
(a)
(b)
(c)
(d)
B1= 10G
B1= 50G
B1=100G
R=300"
R=200"
R=100"
θ=0°
θ=30°
θ=70°
δ=3.0
δ=3.5
δ=4.0
T_B,ν max [K]
Ω_eff [steread]
F_ν [sfu]
ν [GHz]

Figure 5

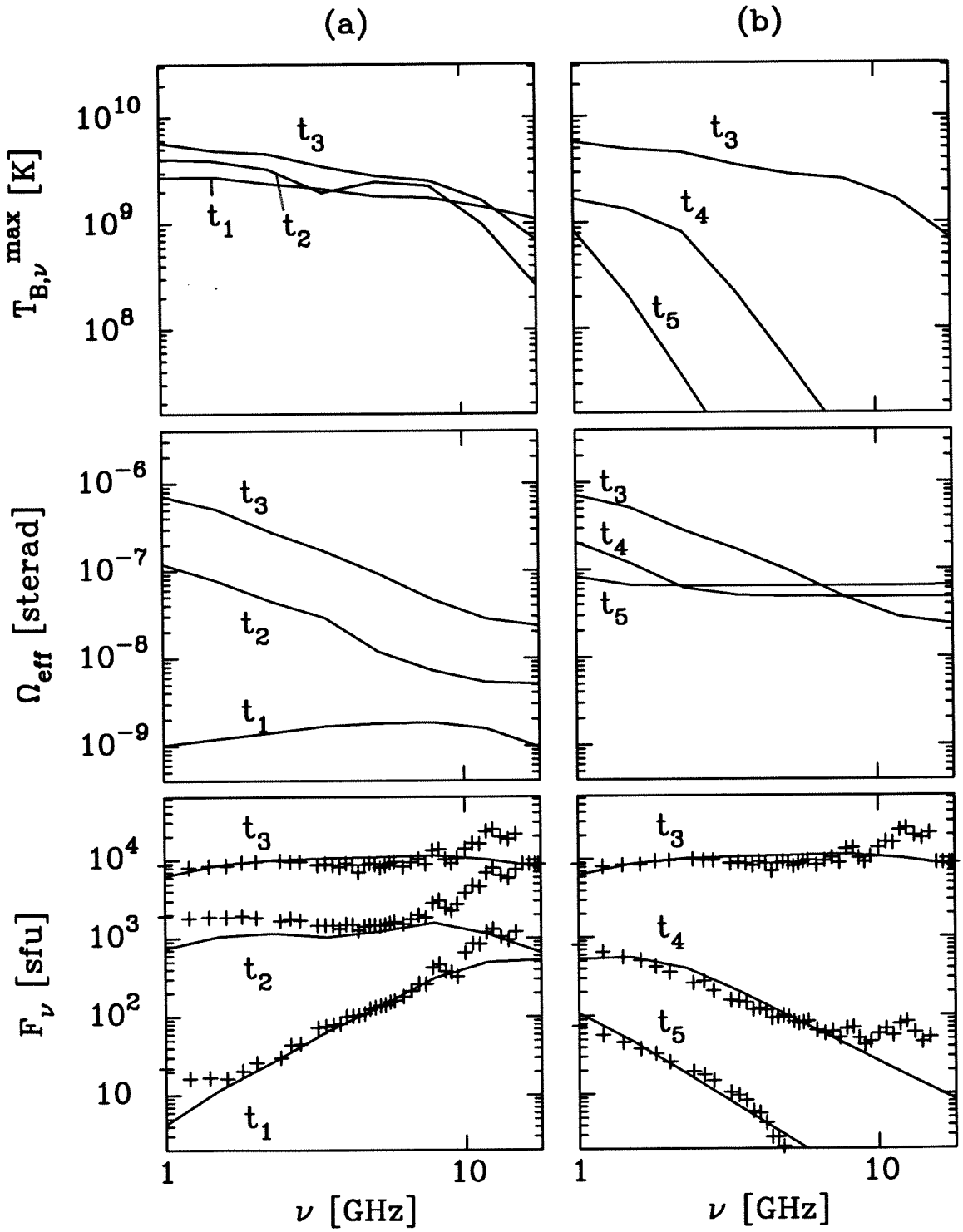
(a)
(b)
$T_{B,\nu}^{max}$ [K]
10^{10}
10^{9}
10^{8}
t_1
t_2
t_3
t_4
t_5
Ω_{eff} [sterad]
10^{-6}
10^{-7}
10^{-8}
10^{-9}
F_ν [sfu]
10^{4}
10^{3}
10^{2}
10
1
10
ν [GHz]

Figure 6